MICRO-FABRICATED SILICON BASED PROBES FOR BIOMEDICAL

APPLICATIONS: RELIABLE NEURAL INTERFACE, ELECTRO-MECHANO

TISSUE ASSAY SURGICAL TWEEZER, AND FLUID VISCOSITY SENSING

A Dissertation

Presented to the Faculty of the Graduate School

of Cornell University

In Partial Fulfillment of the Requirements for the Degree of

Doctor of Philosophy

by

Po-Cheng Chen

May 2016

MICRO-FABRICATED SILICON BASED PROBES FOR BIOMEDICAL
APPLICATIONS: RELIABLE NERUAL INTERFACE, ELECTRO-MECHANO
TISSUE ASSAY SURGICAL TWEEZER, AND FLUID VISCOSITY SENSING

PO-CHENG CHEN, Ph. D.

Cornell University 2016

Micro-electro-mechanical systems (MEMS) have been crucial in revolutionizing healthcare and environmental monitoring. By probing biological systems in mechanical, thermal, electrical and chemical modalities, one can gain a multiphysical characterization and understanding of the biological system. This understanding can be used for a more informed treatment of the disease. A key attribute for the success of MEMS biosensors and surgical tools is their ability to measure biological quantities and gather multimodal information with high resolution while minimizing their invasiveness for chronic reliability.

In this dissertation, four areas are explored where strategies have been developed to minimize biosensor invasiveness and multimodal tissue characterization. Ultrasonic horn neural probes driven at their longitudinal resonance can allow penetration through tissue with less force and induce less tissue damage. A model governing the force reduction proportions to ultrasonic horn probes on driving voltage, insertion velocity, and substrate elasticity is presented to guide design and use of ultrasonic horn probes in neural interface application. An animal model is developed for monitoring probe-tissue interaction over time using two-photon microscopy both electrically and optically.

Secondly, a detachable ultrasonic neural probe inserter is developed. Multiple neural probe geometries and configurations are affixed to the ultrasonic inserter using the polyethylene glycol polymers as an adhesive and a biodissolvable material. Neural

probes can be bonded and debonded reversibly to a silicon inserter with reduced implantation forces. This insertion method can potentially help inserting neural probes made in many different microfabrication technologies.

Thirdly, a silicon tweezer is presented. The silicon structure that can perform tweezing motion without silicon fracture is demonstrated. The silicon tweezer can be used for measuring multiple tissue electromechanical properties including the tissue Young's modulus, tissue penetration force, and electrical impedance. This tweezer can potentially provide more tissue information for surgeons deciding on several options to suture, or remove tissue.

Finally, an ultrasonically actuated silicon probe viscometer with integrated immersion depth sensors and strain gauges were demonstrated. The immersion depth and viscosity information from the liquid can be measured simultaneously. This can potentially solve a major problem of depth calibration in the portable applications of ultrasonic viscometers.

BIOGRAPHICAL SKETCH

Po-Cheng Chen was born in Taichung, Taiwan in 1984. He received the B.S and M.S. degrees in 2006 and 2008, respectively, under guidance of Prof. Chua-Chin Wang from the Department of Electrical Engineering, National Sun Yat-Sen University, Kaohsiung, Taiwan. He served as a corporal of artillery survey team in 2008. After his military service, he joined Prof. Wen-Shiang Chen's Lab as research assistant in National Taiwan University in 2009 for which he investigated MRI-compatible therapeutic ultrasonic driving system. He started his Masters of Engineering degree at Cornell University in 2010. In 2011, he began his doctoral education under the supervision of Prof. Amit Lal. His research interests have included MEMS sensors and actuators in medicine and biomedical application, Internet-of-Thing system, therapeutic ultrasound and mixed-signal circuit design.

To My Mother and Father

I would like to thank the staff members of Cornell Nanoscale Science and Technology Facility (CNF) and Nanobiotechnology Center (NBTC) for their suggestions to fabricate the devices needed to perform my research. I would also like to extend my gratitude to Sue Bulkley, Daniel Richter, Scott Coldren and Patty Gonyea for being patient with me and handling all my department paper works. I would like to thank all my friends in Ithaca for making my experience at Cornell a memorable one. Special thanks goes to I-Tzu Chen for her support and encouragement, and being patient with me throughout my Ph.D.

I am very grateful for all the collaborations, advices, and things I have learned working the people at Cornell over my Ph.D. time.

TABLE OF CONTENTS

LIST OF FIGURES

LIST OF TABLES

CHAPTER 1

INTRODUCTION

Micro-electro-mechanical systems (MEMS) can serve as inertial, pressure, sound, temperature sensors. Another class of MEMS devices include microfluidic systems that are used to characterize contents of a microfluidic sample. A third class of applications of MEMS is for biomedical devices and sensors that can interact with the body (e.g. tissues, and body fluids) directly. Together with microfabrication technology, which is capable of producing patterned mechanical and electrical devices with tens to hundreds of nanometer resolution, it is possible to probe biological system with similar micro and nano dimensions. By probing biological systems in mechanical, thermal, electrical and chemical modalities, one can realize multiphysical characterization and gain a detailed understanding of the biological system under testing. This understanding can be used for treatment of the tissue, one example being tissue characterization during surgical procedures of various maladies. A key attribute for the success of MEMS biosensors and surgical tools is their ability to measure biological quantities and gather multimodal information with high resolution while minimizing their invasiveness for chronic reliability. In this thesis, four different silicon-based MEMS devices are presented that minimize invasiveness, and characterize multiple tissue and fluid properties. In this chapter, a general introduction to the silicon-based neural interface based on a silicon ultrasonic transducer is presented.

1.1 *Microelectromechanical Systems and neural interfaces*

Silicon multi-electrode arrays (MEAs) allow for high-resolution measurement of electrical activity in electrically active tissues. The two-dimensional electrode arrays allow spatial analysis of recorded signals and decomposition into regional variations of

activity. These variations are important in understanding neural activity patterns. In the field of neural recordings, silicon probe arrays such as the Utah [1] and Michigan [2] electrode arrays have been developed with tens of hundreds of recording electrodes sites to allow intra-cortical recordings simultaneously. These electrode arrays have been used for understanding brain function in animals [3], [4]. These probes have also been demonstrated in humans for controlling prosthetic [5] and computer cursor [6]. The neural probes, when used for chronic recordings, have not been reliable. The biological immune system recognized the implanted as a foreign object. Foreign body reactions, which can quickly encapsulate the implant are one of the reasons that prevent long-term chronic recordings. Study of the immune response onset and methods to counteract the body response have been investigated here. To provide an understanding and rationale for the silicon-based neural interfaces, Section 1.1.1includes an introduction to neuron cell signaling methods and substrate materials, and a discussion of how biological cell activity can be transduced into electrical currents recorded by the electrodes.

1.1.1 Neuronal cell signaling and substrate material

In biological neural networks, neural cells communicate by conduction of action potentials. Action potentials arise from the flow of ionic currents in and out of cells. Neurons have voltage-gated ion channel that selectively allow ions to flow through them based on the voltage difference between the inside and outside of the cells [7]. The steady state relative potential between intracellular and extracellular space is called the resting membrane potential. The resting potential (E_k) is determined by the concentration gradients and the relative membrane permeability's of the ions in the system and is typically on the order of -70 mV relative to the extracellular potential. The value of resting potential can be determined using the Nernst equation relating internal $[K_+]_i$) and external ($[K_+]_o$) potassium concentrations:

$$E_k = \frac{RT}{zF} ln \left(\frac{[K_+]_o}{[K_+]_i} \right) \tag{1.1}$$

where R is the universal gas constant (8.314 J·K^{-1}·mol^{-1}), z is the valence of the ion species (+1 for potassium), and F is the Faraday's constant (96,485 C·mol^{-1}). If the cell is stimulated beyond its threshold potential (between -40 to 55 mV), voltage-gated sodium channels will begin to open with sodium ions entering the cell resulting in cell depolarization. When the membrane potential is sufficiently depolarized, voltage-gated potassium channels begin to open allowing potassium ions to diffuse out of the cell, which repolarizes the cell. At this lower potential, the sodium channels begin to inactivate, and membrane permeability to sodium ions ceases to a halt. The potassium ion channels then also close. The resulting membrane potential waveform is called the action potential (Figure 1.1).

Traditionally neurophysiologists have measured the neuron electrical activity using glass microcapillaries that can be pulled to very fine tip diameter to penetrate the double layer of cells. The glass capillaries are filled with a conductive solution. A small metal wire is threaded down the capillary to connect electrically the liquid to an external amplifier voltages. The ionic and currents are measured via the wire. The intracellular potential relative to the extracellular potential of cells is measured by having a reference electrode outside the cell. MEMS silicon neural probes are implanted into tissue, and the electrodes are almost always in extracellular space. The electrodes measure the summed activities of nearby cells, by having a larger exposed metal electrode surface to the tissue compared to the micro capillary method. Due to the structural differences and the presence of a capacitive shunt in the microcapillary, the frequency filtering properties of the two types of electrodes are different. Glass microcapillaries behave as
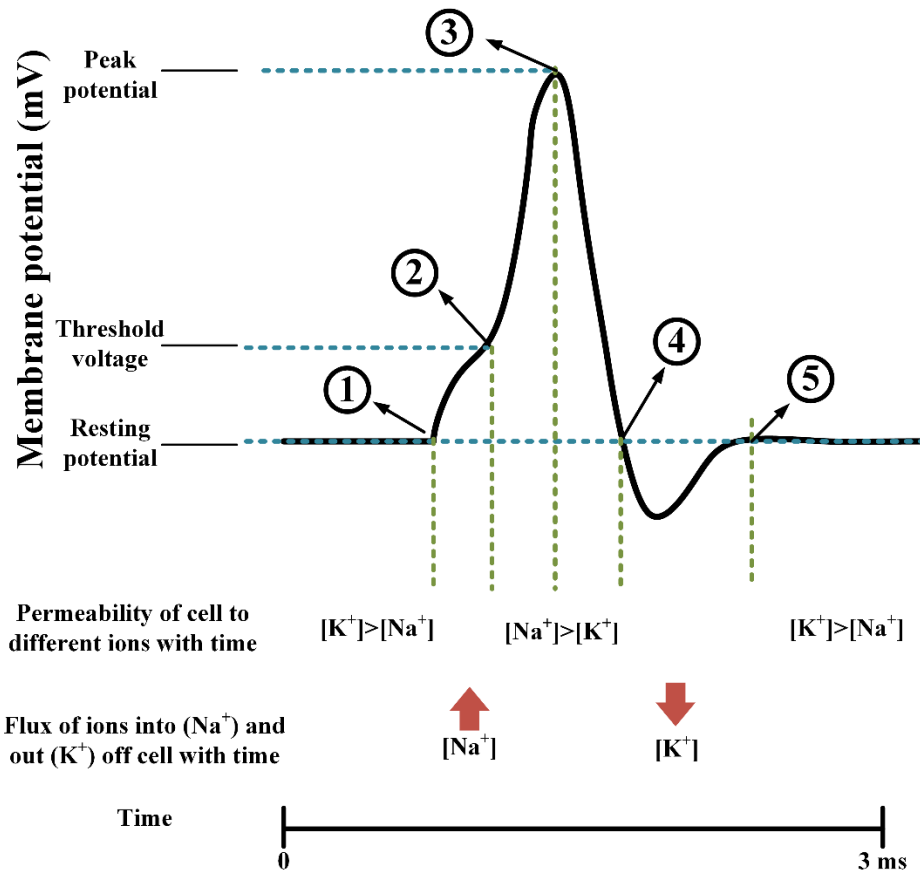
Figure 1.1: Typical neural cell action potential with changes in membrane permeability to sodium and potassium ions over time. Depolarizing stimulus causes membrane potential to become greater than a threshold voltage; the depolarization triggers an action potential (point 1 and 2). The initial depolarizing phase of an action potential consists of a smooth and rapid increase in V_m from negative resting potential to a maximum peak value (point 3). This sharp rise in Vm to the peak voltage of the action potential is then followed by a slower repolarizing phase (point 4 and 5).

low pass filter due to a low DC resistance of 10-200 MΩ and MEMS electrodes with DC resistance of 10-200 GΩ behave as high pass filter. In extracellular recordings, recorded activity includes local field potentials and neural spike (action potentials) activity with frequency components of up to a few kHz. The extracellular recording can include the contribution of signals from many neurons, requiring software approaches to identify signals from specific neurons. The problem of identifying individual neurons from the confounded signals can be alleviated by having many electrode sites to allow decomposition of signals into their various source signals. Additionally, the main benefit of extracellular recording lies in providing a viable method for longer-term neural recording. Though immune reactions are seen when electrodes are inserted in biological tissue, in extracellular recordings, cells are not penetrated and damaged as they would be for the intracellular recordings.

Various substrates are used for extracellular probes, including silicon microfabricated structures [1], [2], polyimide [8], silk [9], etc. Silicon-based substrates allow integration with additional functionality, such as COMS circuits [10], other sensors [11], and microfluidic elements [12] to gather further information about the neurons and the environment. Polyimide and silk have been introduced as electrode substrates for a better match to the mechanical elasticity of the neural tissue. It is believed with lower mechanical elasticity properties of the substrate, the tissue damage, and immune response can be reduced, although the exact mechanisms for damage response are still not conclusively identified. One of the major challenges with very flexible neural probes is that the probe can easily bend and buckle during insertion into tissue. Additional insertion tools are required to reach target area in the brain as their rigidity is not sufficient to penetrate the tissue [13]. To address this issue, an ultrasonic assisted inserter is developed for reducing the insertion force is presented in Chapter 3. This insertion technique can be used to penetrate soft probes into tissue.

1.1.2 Electrochemical transduction mechanism to metal electrodes

In the physiological environment, the bioelectric signals are carried in the electrolytic media in the form of ionic currents. Metal-based based electrodes are used to transduce these signal to voltages that can be amplified and digitized for digital signal processing. Therefore, the electrical characteristic impedance of the electrode-electrolyte interface is of utmost importance during electrophysiological studies. Experimental results have shown that the impedance of the interface has both frequency dependent reactive and resistive components which vary with frequency and current density. For small current densities, the charge exchange between ions in the electrolytic media and electrons in metal electrodes occurs by displacement currents across the capacitor formed by the double layer at the interface. On the other hand, the reduction-oxidation reaction will happen with high current densities. When a partially soluble metal electrode is immersed in an electrolyte, thermodynamic processes favor chemical reactions which result in dissolution of the metal into metal ions, and the buildup of negative charges on the metal electrode surface. The positive charges from the electrolyte accumulate near the electrode surface. This buildup proceeds until an equilibrium state is reached where the charge accumulated in the metal is enough to balance the thermodynamic favorability of the chemical reaction so that reduction and oxidation reactions occur at the same rates. A capacitive electrical double layer (EDL) is formed on the surface of the electrode from the charge exchange process. This double layer capacitance is in series with an electrolyte solution resistance. An equivalent circuit model (Figure 1.2) considered which is comprised of a constant phase angle impedance Z_{CPA} that represents the interfacial capacitance. This capacitance is further shunted by the charge transfer resistance R_{ct}, together in series with the spreading resistance R_s [14]–[16].
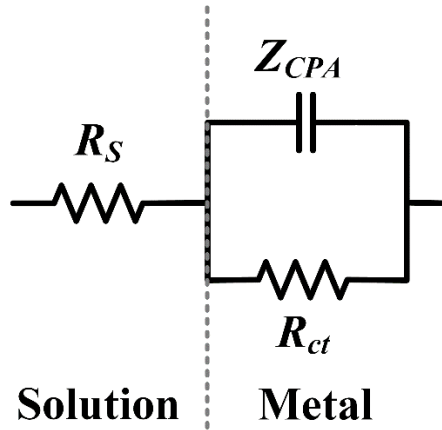
Figure 1.2: Equivalent circuit model of the electro-electrolyte interface. A constant phase angle impedance Z_{CPA}, that represents the interface capacitance impedance, shunted by a charge transfer resistance, R_{ct}, together in series with the solution resistance R_S.
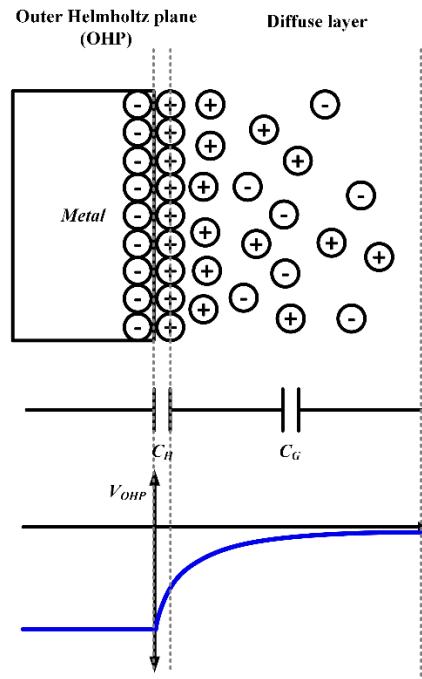
Figure 1.3: Formation of Outer Helmholtz plane (OHP) and Diffuse layer (metal-electrolyte interaction), and their contribution to interfacial capacitance, which is the combination of the C_H and C_G.

Based on the Gouy-Chapman-Stern (GCS) model, the interfacial capacitance C_I ($Z_{CPA} = 1 / j\omega C_I$) can be described by the combination of a Helmholtz capacitive layer C_H and a diffuse layer (Gouy-Chapman) capacitance C_G (Figure 1.3) [17], [18]. The capacitance can be express as

$$\frac{1}{C_I} = \frac{1}{C_H} + \frac{1}{C_G} \qquad (1.2)$$

The Helmholtz capacitance C_H assumes that the charge in the solution is concentrated in a plane (the outer Helmholtz plane, OHP) parallel to the metal surface, and the capacitance can be written as a parallel plate capacitor as

$$C_H = \frac{\epsilon_0 \epsilon_r A}{d_{OHP}} \qquad (1.3)$$

where ϵ_0 is the dielectric permittivity of free space (8.854×10^{-12} F/m), ϵ_r is the relative dielectric permittivity of the medium between the plates of capacitor, A is the surface of the metal, and d_{OHP} is the distance of outer Helmholtz plane to the metal surface.

The actual space charge region extends from the interface into the medium with a charge density gradient, which decreases from a maximum value at the interface to the bulk concentration in the medium. This layer is a result of the attraction of ions to the surface by surface forces and diffusion away from the electrode due to excess concentration. As the potential applied to the electrode is increased, the ions tend to pack closely near the metal surface reducing the thickness of the space charge region and further increasing the interfacial capacitance. The potential dependent capacitance, C_G, of the diffuse layer, is described by Guoy-Chapman model as

$$C_G = \frac{\epsilon_0 \epsilon_r \cosh\left(\frac{zV_{OHP}}{2V_t}\right)}{L_D} \tag{1.4}$$

where $V_t = k_t/q$ is the thermal voltage (~26 mV @ 25 °C), z is the charge of ions and V_{OHP} is the voltage at the outer Helmholtz plane. The Debye length, L_D, is given as

$$L_D = \frac{\epsilon_0 \epsilon_r V_t}{2n^0 z^2 q} \tag{1.5}$$

where n^0 is the concentration of the bulk medium in moles/liter of the ion and q is the charge of the electron (1.602×10^{-19} C).

From Equation (1.3) to (1.5), Equation (1.2) can be rewritten as

$$\frac{1}{C_I} = \frac{1}{A}\left(\frac{d_{OHP}}{\epsilon_0 \epsilon_r} + \frac{L_D \cosh\left(\frac{zV_{OHP}}{2V_t}\right)}{\epsilon_0 \epsilon_r}\right) \tag{1.6}$$

Equation (1.6) can be further simplified to the below expression at 25 °C

$$\frac{1}{C_I} = \frac{1}{C_H} + \frac{1}{C_G} = \frac{1}{A}\left(\frac{d_{ohp}}{\epsilon_0 \epsilon_r} + \frac{1}{2.28\sqrt{C^* \cosh(19.5V_{OHP})}}\right) \tag{1.7}$$

The interface also consists of resistance, charge transfer resistance R_{ct}, which serves as the DC path for current flow in parallel with the interfacial capacitance. For small applied voltages, this is shown to be

$$R_{ct} = \frac{V_t}{J_0 z} \tag{1.8}$$

9

where V_t is the thermal voltage, J_0 is the equilibrium exchange current density of reduction and oxidation across the electrode-electrolyte interface in the unit of A/cm^2, and z is the valence of the ion responsible for conduction. Additionally, the net resistance encountered by the current spreading out from an electrode into a conductive solution, spreading resistance R_s. The magnitude of the resistance is determined by the geometric surface area of the electrode. For a planar rectangular electrode, the spreading resistance can be expressed as

$$R_s = \frac{\rho \, ln\left(\frac{4l}{w}\right)}{\pi l} \tag{1.9}$$

where l and w are the length and width of the rectangular electrode, ρ is the resistivity of the solution. Diffusion effects can be significant and add to further terms in the equivalent circuit, but are not relevant at the low frequencies discussed here with platinum electrodes. Empirically, the interfacial capacitance has been shown to fit the model

$$Z_{CPA}(\omega) = \frac{1}{(j\omega Q)^n} \tag{1.10}$$

where $\omega = 2\pi f$, Q is a measure of the magnitude of Z_{CPA}, and n is an empirical factor constant ($0 \leq n \leq 1$) representing the surface irregularities [19].

1.2 *Ultrasonic horn transducer*

Ultrasonic horn transducers are resonators with tapered cross-sections to concentrate mechanical energy at the tip of the transducer with a small-sectional-area, therefore achieving high vibration amplitudes [20]. Consider a differential element from a rod

with a variable cross section, under the assumptions of uniform stress distribution, material homogeneity, and negligible Poisson effect, the equation of motion is given by [21].

$$-\sigma A + \left(\sigma + \frac{\partial \sigma}{\partial x}dx\right)\left(A + \frac{dA}{dx}dx\right) = \frac{1}{2}\rho\left\{A + \left(A + \frac{dA}{dx}dx\right)\right\}dx\frac{\partial^2 u}{\partial t^2} \qquad (1.11)$$

where σ is the stress acting on the cross section of the element, $A(x)$ is the variable cross section as a function of the distance along the axis of the rod, x, ρ is the density, and $u(x)$ is the displacement along the x-direction. Assume the second-order partial differential term is negligible in the limit of $dx \to 0$, Equation (1.11) can be reduced to

$$\frac{1}{A}\frac{\partial}{\partial x}(\sigma A) = \rho\frac{\partial^2 u}{\partial t^2} \qquad (1.12)$$

Substituting stress with $\sigma = E\frac{\partial u}{\partial x}$, where E is the Young's modulus, Equation (1.12) can be rewritten as

$$\frac{1}{A}\frac{\partial}{\partial x}\left(EA\frac{\partial u}{\partial x}\right) = \rho\frac{\partial^2 u}{\partial t^2} \qquad (1.13)$$

In a uniform material, E and ρ are constant along the x-direction, Equation (1.13) can be simplified as

$$\frac{1}{A}\frac{\partial}{\partial x}\left(A\frac{\partial u}{\partial x}\right) = \frac{1}{c_0^2}\frac{\partial^2 u}{\partial t^2} \qquad (1.14)$$

Alternatively, one can rewrite the above equation as:

$$\frac{\partial^2 u}{\partial x^2} + \left(\frac{\partial u}{\partial x}\right)\frac{\partial}{\partial x}\left(lnA(x)\right) = \frac{1}{c_0^2}\frac{\partial^2 u}{\partial t^2} \tag{1.15}$$

where $c_0 = \sqrt{E/\rho}$ is the speed of sound in the medium. Equation (1.15) is the Webster horn equation [22], [23]. The particle velocity is amplified at the tip of the smaller cross section of the horn when compared to the velocity at the end with the larger cross section. The amplification in particle velocity is dependent on the horn profile and the ratio of areas of the larger and smaller cross sections at the end of the horn. Several horn shapes, *A(x)*, have been previously investigated, including exponential, linear, stepped, and catenoidal horns [23]–[25]. A catenoidal horn shape allows for a large displacement amplification between the end and tip of the probe while minimizing stress concentration [24]. The shape of catenoidal horn is shown in Figure 1.4 and defined by

$$A(x) = A_1 \times cosh^2(\alpha(L - x)) \tag{1.16}$$

where

$$\alpha = \frac{cosh^{-1}\left(\sqrt{\frac{A_0}{A_1}}\right)}{L} \tag{1.17}$$

where A_0 and A_1 are the cross-sectional areas of the probe at the tip and end, and *L* is the length of the horn. In the neural probes application, the horn includes small probes which can be treated as mass loads if the length is much shorter than the wavelength.

For designing ultrasonic transducers, a material with high particle velocity is critical to have an appropriate interface for electro-mechanical actuation using piezoelectric lead-zirconate-titanate (PZT). The maximum attainable particle velocity is proportional
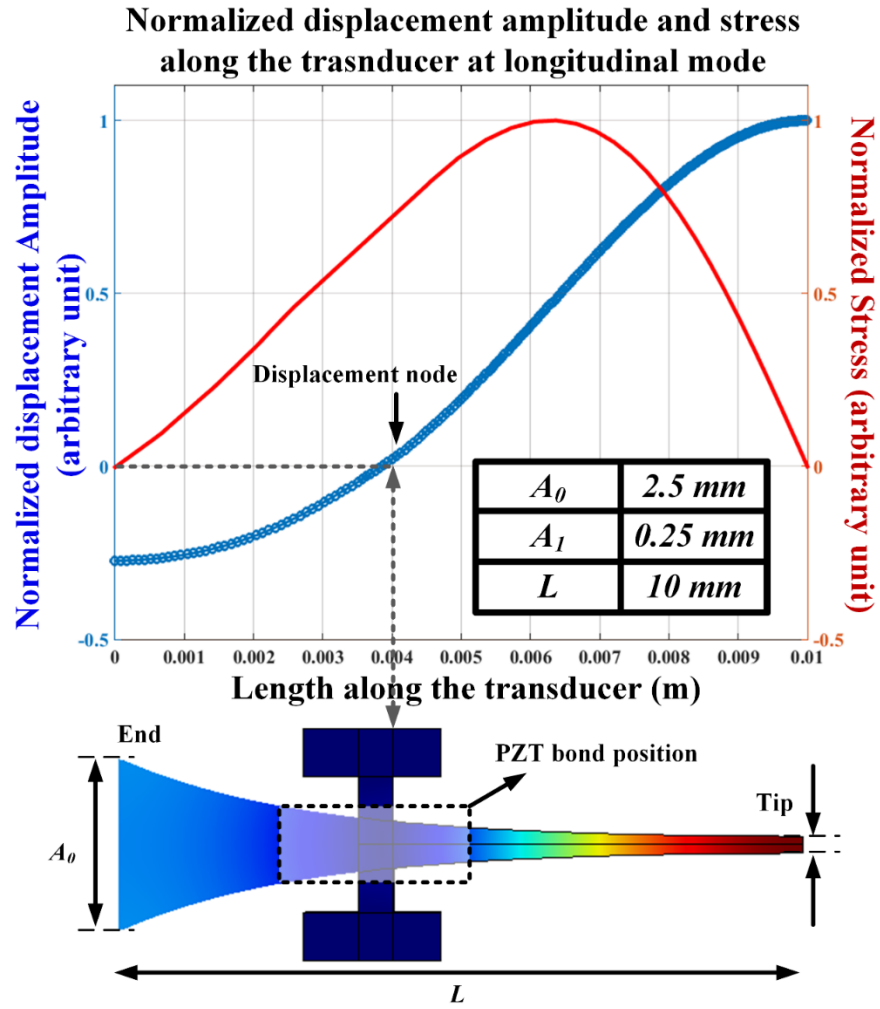
Figure 1.4: Finite element simulation of catenoidal horn longitudinal normalized displacement and stress along the transducer. An amplitude magnification of 4 is obtained between the end of the probe and the tip of the probe.

to the product $S_m c$, where S_m denotes the maximum strain that can be sustained by the material without plastic failure and c is the velocity of the sound in the material [26]. Since PZT ceramics have low $S_m c$ values (~0.93 m/s), the vibration amplitudes generated by electro-mechanical transduction is limited. A velocity transforming waveguide (ultrasonic horn) can be used for magnifying the vibration amplitude produced by the PZT to much higher levels. Titanium ultrasonic transducers are well-known instruments for ultrasonic surgery such as for phacoemulsification. However, by implementing ultrasonic transducer in silicon ($S_m c$: 335 m/s), eight times higher particle velocity can be achieved as compared to 41 m/s $S_m c$ for titanium-alloy [24]. Moreover, silicon ultrasonic transducers can contain integrated sensors for closed feedback control of the ultrasonic horn. The high thermal conductivity of the silicon and low internal loss can generate less heat, and thermal gradients compared to titanium based instruments.

The use of silicon-based MEMS in the field of ultrasonic has opened a new age and provided innovative solutions for various applications. The silicon ultrasonic horn transducer driven by bulk PZT plates in their longitudinal mode have been shown to produce high vibration amplitudes comparable to the traditional titanium-alloy [24]. Silicon ultrasonic horn based transducer have been emerging as a suitable transducer due to their superior material properties and their capability for integration of microfabrication sensor technologies. Within integrated sensors, strain, and bio-electrical potential measurement can be achieved in various applications, such as phacoemulsification microsurgery [21], testicular tubule assay [27], blood viscosity sensing [28] and ventricular fibrillation monitoring [29].

1.3 *Summary of contributions*

This thesis presents results pertaining to three areas of investigation summarized below, along with the key contribution in each area.

Ultrasonically driven neural probe for reliable neural interfaces

The key contributions in this area are listed below and presented in Chapters 2 and 3.

1. A systematic study on inserting ultrasonically driven neural probe as a function of ultrasonic driving voltage was performed The tissue damaged area consisted of highly jagged edges during normal insertion, but became compact and circular with ultrasonic insertion observed. Insertion force and acute microglial response reduction were also observed providing evidence of improved probe reliability.

2. A mouse model was developed for chronic inflammatory response study. Two-photon excited fluorescence microscopy combined with the ultrasonic neural interface are used to investigate the chronic affects with ultrasonic-assisted implantation over time. Initial results suggest improved lifetime of neural probe recording site.

3. A silicon ultrasonic horn based neural probe insertion method is developed. An ultrasonic silicon horn inserter is designed to affix different types of neural probes using the polyethylene glycol (PEG) polymer as an adhesive and a bio-dissolvable material. Neural probes with different geometries and configurations are bonded and debonded reversibly to a silicon ultrasound inserter. Insertion force reduction by 76.8% is observed in 2% agar gel tissue phantom is present. This method can potentially help inserting neural probes made in any new technology.

4. Design and testing of a miniaturized control and recording system for ultrasonic neural probe including a wireless data transmission application-specific integrated circuit (ASIC). Using this system, multiple measurements of the

ultrasonic neural probe, neural electrical activity, resonance frequency, and strain, can be extracted wirelessly.

Multimodal tissue characterization with electro-mechano silicon tweezer

The key contribution in this area is listed below and presented in Chapter 4.

1. A silicon/plastic hybrid tweezer that can be used for measuring multiple tissue electromechanical properties, Young's modulus, insertion force (penetration force) and electrical impedance, is demonstrated. A silicon tweezer structure that can perform tweezing motion without silicon fracture is demonstrated. Two different distance sensing methodologies, ultrasonic pulse-echo, and integrated strain gauge, are investigated. This tweezer device can potentially provide more tissue information for surgeons deciding on several options to suture, cut or remove tissue.

Ultrasonic viscometer with integrated submersion depth measurement

The key contribution in this area is listed below and presented in Chapter 5.

1. An ultrasonically actuated silicon viscometer with integrated immersion depth sensor and strain gauges were demonstrated. The immersion depth and viscosity information from the liquid can be measured simultaneously. This can potentially solve a major problem of depth calibration in the portable application of ultrasonic viscometers.

CHAPTER 2

ULTRASONICALLY ACTUATED INSERTED NEURAL PROBES FOR

INCREASED RECORDING RELIABILITY

2.1 *Introduction*

Advancements in the field of neural prosthetics can utilize neural interfaces to record large-scale neuronal activities, and using that information to control prosthetic limbs. This approach to prosthesis holds promise for high degree of control in prosthetics, offering potential treatment of patients who suffer from limb loss, damage after brain surgery, and other neuropathies [30]. By implanting electrodes that can record and stimulate neural activity with the necessary spatial and temporal resolution, the neural probe technologies can help bridge a patient's cortical activity to limbs or external devices. However, a major limitation in the use of neural probes is achieving a reliable long-term stable neural-probe interface, as the brain immune response typically passivates the electrodes preventing neural potentials to be measured.

Neurons only comprise approximately 25% of the brain tissue, and the rest consists of glial cells and vasculature [31]. Glial cells include oligodendrocytes, astrocytes, and microglia, each of which serves particular functions. Oligodendrocytes create myelin for the nerve fibers. Astrocytes and microglia are mediators of the brain immune response. Astrocytes compose 30-65% and microglia comprises 5-10% of the total glial cells [31]. Astrocytes normally maintain the chemical environment and mechanically support neurons, while microglia can phagocytose and serve as cytotoxic cells. Both microglia and astrocytes change form when they become activated for an immune response. To achieve a useful neural interface, the requirements are high signal-to-noise ratio, the capability to record from many units, and well-defined electrode spatial

location allowing post-processing of the recorded signals to isolate distinct unit firing activity. Neural interfaces can be categorized by the tissue damage (invasiveness level) and spatial neural signal resolution (Figure 2.1). For example, electroencephalography (EEG) monitors voltage fluctuation resulting from ionic current within the neurons of the brain by placing electrode along the scalp, which does not cause any tissue damage. However, it suffers from the low spatial resolution on the scalp and poor signal-to-noise ratio. On the other hand, electrocorticography (ECoG), similar to EEG, which places electrodes directly on the exposed surface of the brain, is more invasive but can achieve better spatial signal resolution and signal-to-noise ratio. Microelectrode arrays (MEAs), which implant multiple electrodes once into a specific location in the brain, can obtain the best spatial resolution and signal-to-noise ratio. However, MEAs typically causes significant damage to the brain tissue and leads to the most severe immune response of the brain.

Many researchers have observed that the loss of electrode function after chronic insertion leads to significant signal degradation [31]–[33]. Studies indicate two main types of reactions resulting from electrodes in tissue. The first results from the initial insertion trauma, which includes physical damage to capillaries, the extracellular matrix, and the neurons themselves. It has been observed that the initial insertion trauma causes hemorrhage and edema, in addition, to a microglia response that can fade, in some cases, after a few weeks. This phenomenon of an initial insertion trauma response is supported by control studies which examine the impact of electrode stab wounds on the tissue. These studies demonstrate little trace of electrode tracks several months after the stab wounds. The initial microglial response is followed by a chronic foreign body response where cell morphology and behavior change to reactive glial type cell. These glial cells most commonly form a glial scar surrounding the electrode a few weeks after insertion [34]. Also, various studies have pointed to different foreign body response reactions to
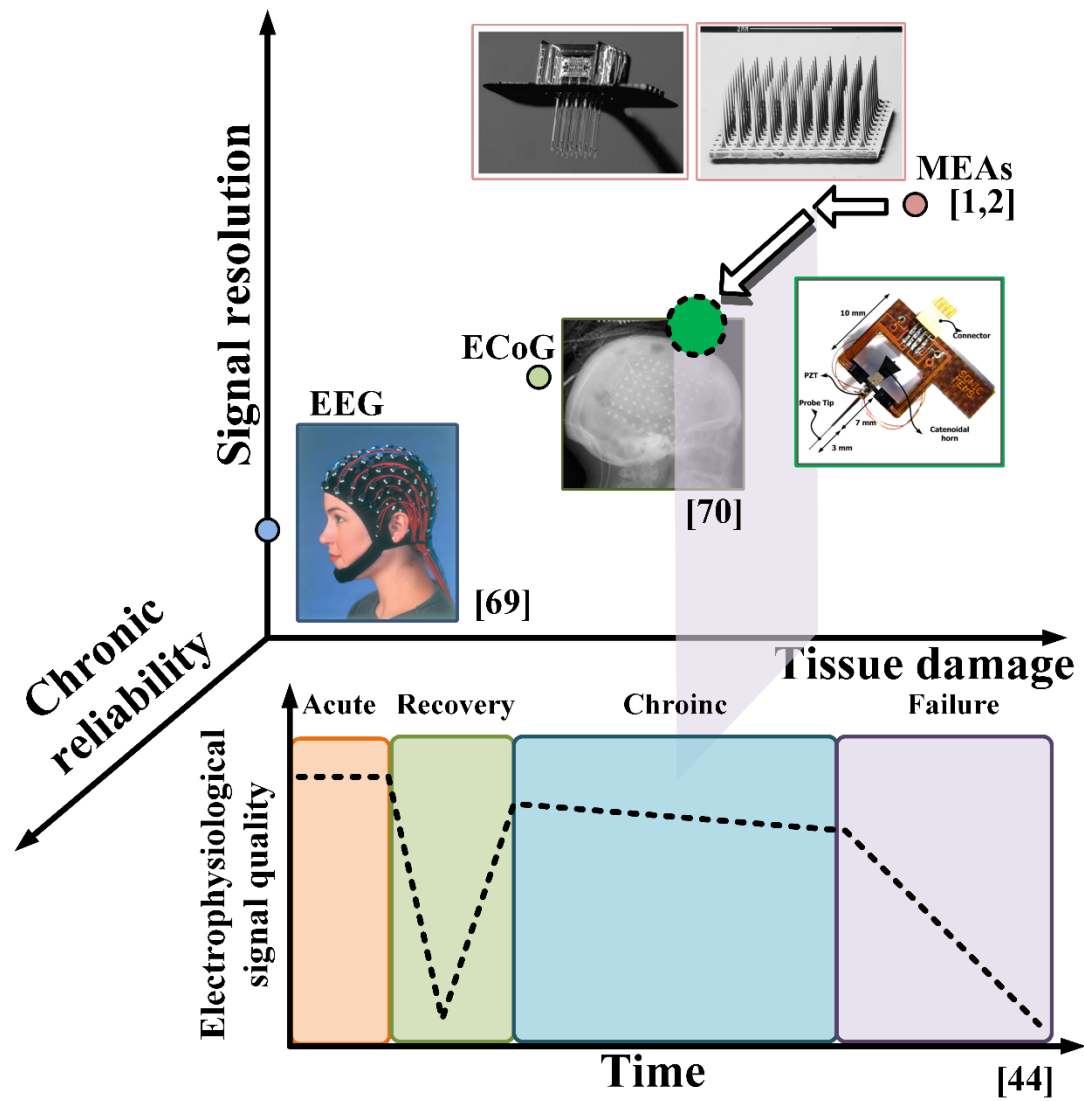
Figure 2.1: Different types of the neural interface and the reliability issues [1], [2], [35]–[37].

electrode insertion, depending on insertion material, tip-shape, insertion velocity, and other conditions. The effect of silicon electrode tip shape, probe size, tip angle, shaft number has been investigated as a potential way to reduce damage to cells [38]–[40]. It has been demonstrated that a chisel-point silicon electrode tip shape can produce a kill zone of less than 10 µm [41]. Additionally, electrode insertion velocity may have an effect on tissue response [42]. Thinner and less stiff materials are also being investigated to determine their effect on reducing tissue immune reactions [43]. However, one of the challenges of using very thin, flexible materials is that the electrode buckles during insertion. Biocompatible coating techniques to decrease electrode impedance have also been investigated. For example Poly (3, 4-ethylenedioxythiophene) (PEDOT) can decrease the initial impedance of electrodes and reduce the electrode size required to record from a given area [44], [45]. When inserted for long-term neural recordings, PEDOT-coated electrodes exhibit a lower electrode site impedance versus uncoated electrodes for a period of at least 40 days post-surgery, after an initial swelling period disappears [46].

The chronic electrical recording response includes [35] four phases: 1) acute (physical damage due to surgery), 2) recovery (inflammation impact), 3) chronic (chronic impact by neural matrix and electrodes) and, 4) failure (signal-to-noise ration become zero) (insert Figure2.1b). There are many challenges in achieving repeatable biological reactions to inserted electrodes, and creating viable solutions to allow decades-long high-quality electrical recordings from probe-based neural interfaces. However, by developing quantitative methods to assess tissue-electrode reactions *in-vivo* and *ex-vivo* in large numbers of animals, we can seek to understand better the problem. In this chapter we specific address chronic reliability in the initial induced trauma during the neural probe implantation procedure. Our hypothesis is that an ultrasonically actuated neural probe can minimize both mechanical stress and damage

during and after insertion. Furthermore, histology, two-photon microscopic stress, and electrical activity can be monitored on the probe surface, providing feedback to change the neural electrode operation actively.
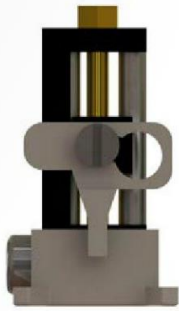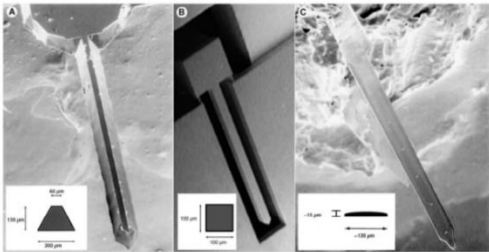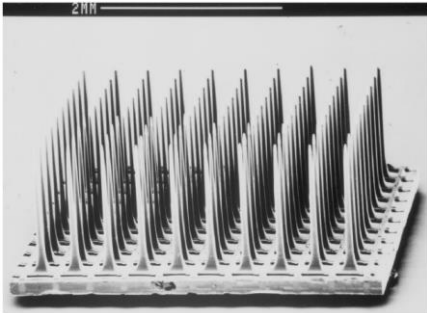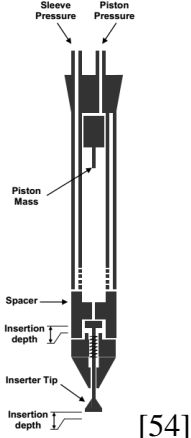
2.2 *Insertion forces model*

Different insertion methods had been reported. For example, micro-wire array is implanted by hydraulic micro positioner at the speed of 100 μm per 1-min interval [47]. On the other hand, the Utah MEA array is implanted by a high speed piston device at the speed of 8.3 mm/s [48]–[50]. Michigan style probes are implanted by using a linear motor at the speed of 2 mm/s [34], [51]. Here we purposed an ultrasonically actuated neural probe insertion method. The neural probe is implanted with a linear motor at the speed of 2 mm/s and augmented by ultrasonic vibration at the tip of the neural probe. Our hypothesis is that an ultrasonic assist neural probe implantation can lead to reduced chronic inflammation and better electrode performance by reducing the initial insertion stress and tissue damage. A summary of the different insertion methods are summarized in Table 2.1. In this section, insertion force models are presented for both non-ultrasonic actuated and ultrasonic actuated. The secondary effects from the ultrasonic actuated insertion are discussed at the end of the section.

2.2.1 Traditional insertion force

The main goal of the inserting and cutting operation is to break the internal bonds in a material by stressing structural materials with constant force. The stress within the material is directly proportional to the applied force and inversely proportional to the contact area. When the total stress exceeds the strength of the material, the inserting and cutting starts. Soft biological material tissues are predominantly characterized by viscoelastic deformation properties, for example, the ability for stress relaxation and

21

Table 2.1: Different insertion methods of neural interface

Neural probe style	Insertion instrument	Insertion speed
Microwire arrays[47]	[52]	100 μm per 1 min interval
Michigan style nerual probes [34]		2 mm/s
Uath array [53]	[54]	8.3 m/s

consequent creep relaxation and deformation. From Kelvin-Voigt model, the stress of soft biological tissue can be express as:

$$\sigma(t) = E_{tissue}\varepsilon(t) + \eta\frac{d\varepsilon(t)}{dt} \tag{2.1}$$

where E_{tissue} is the Young's modulus of tissue, η is the viscosity of the tissue, and $\varepsilon(t)$ is time-dependent strain. These time-dependent effects are caused by the scattering of deformation energy in the area when the probe tip contacts the tissue and for the expanding deformation. Therefore, to reach the yield limit of the tissue, the inserting and cutting velocities must exceed the stress relaxation velocity.

Let us look at a two-dimensional probe insertion model. A probe, infinite in depth, with a defined wedge angle α and a shank thickness of d inserts into a tissue, three zones with different deformation characteristic can be distinguished: 1) separation zone in the immediate vicinity of the cutting edge, 2) deformation zone along the wedge, and 3) compression zone along the shank of the probe (Figure 2.2). In the separation zone, upon contact with the edge of the probe, the tissue will be pushed down. The stress propagates and increases due to the resistance of the tissue until the yield stress is exceeded. The characteristic force component at this stage is the cutting resistance, F_r. In the deformation zone, the wedge leads to biaxial deformation, the magnitude of which depends on the wedge angle and the blade thickness. Lateral displacement leads to the deformation force, F_w, and friction force, F_{fw}, along the wedge surface. In the compression zone, displacement of the tissue causes the generation of lateral compression force F_l, and the relative motion develops the frictional force, F_{fl}, along the probe shank. In a plunge-style inserting configuration (insertion angle equals to zero), the total inserting force F_x is the sum of cutting resistance force and wedge
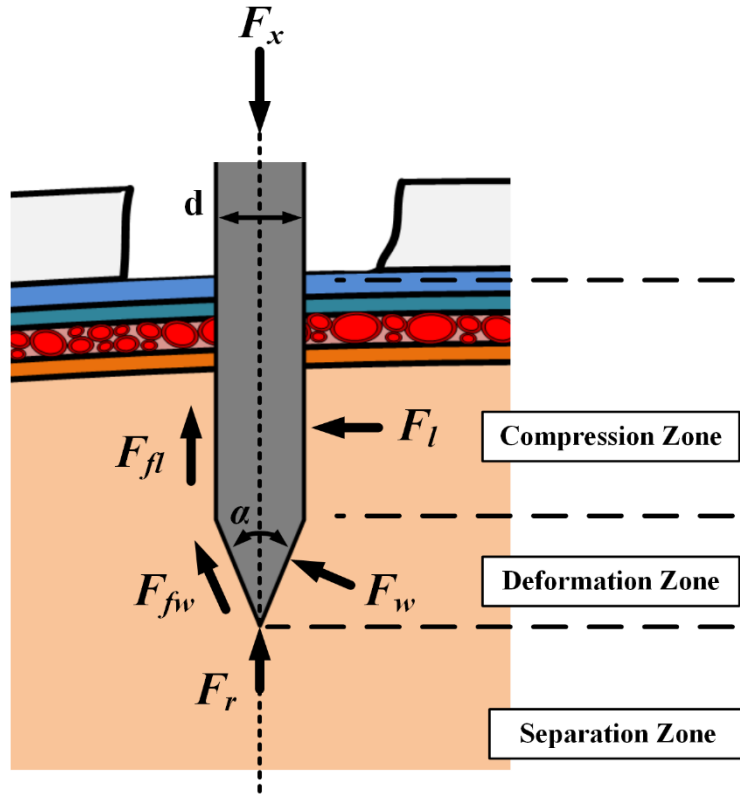
Figure 2.2: Force distribution during probe inserting/cutting into tissue.
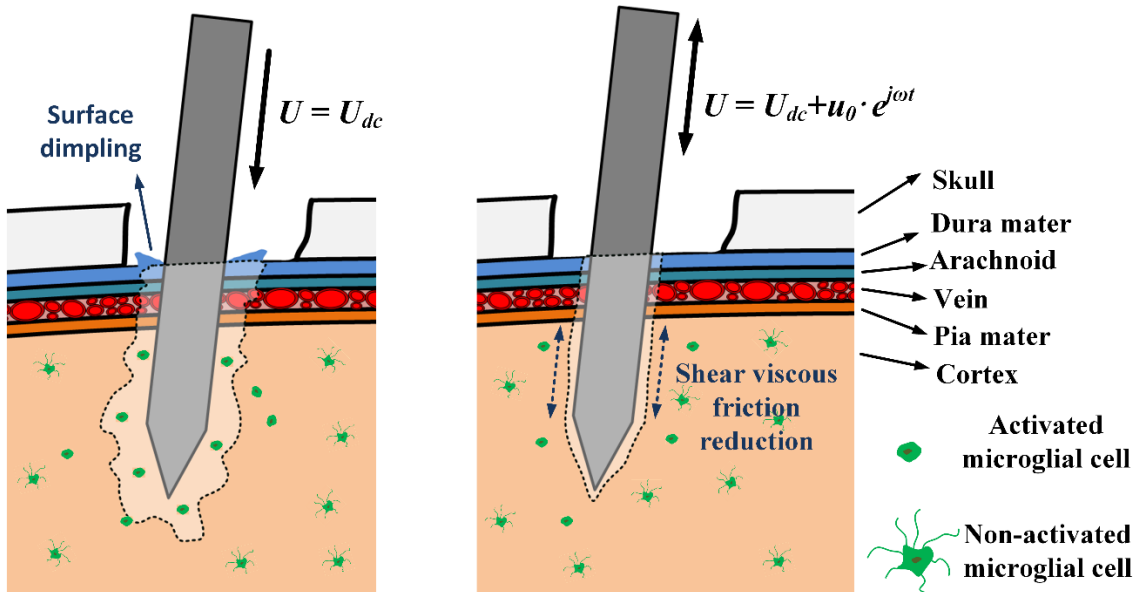
Figure 2.3: Insertion velocity components for non-ultrasonic actuation versus ultrasonic actuation.

deformation force. Additionally, the friction force from the wedge and shank need to be taken into account. The total insertion force can be express as

$$F_x = F_r + 2 \cdot F_w \cdot sin\left(\frac{\alpha}{2}\right) + 2 \cdot F_{fw} \cdot cos\left(\frac{\alpha}{2}\right) + 2 \cdot F_{fl} \tag{2.2}$$

As the inertia force of the tissue due to its acceleration is not considered, Equation (2.2) only hold for low inserting velocities. The insertion force components depend greatly on the properties of the tissue and the properties of the probe so that the cutting forces can only be determined experimentally [55].

2.2.2 Ultrasonic enabled insertion force

Ultrasonic enabled insertion can be distinguished from conventional insertion by the specific motion characteristics of the inserting tool, as the conventional movement of the device is augmented by ultrasonic vibration (Figure 2.3). In plunge-type insertion configuration (the main vibration axis and the moving axis of the inserting tool are identical, and the vibration axis is perpendicular to the tissue surface), the stress and strain action on the tissue due to the macroscopic feed motion is intensified or diminished by a periodical stress with a high frequency and a low amplitude. Stress and strain are mainly exerted in the separation zone where the tip is in contact with the tissue. The effective cutting velocity U can be expressed as the sum of the linear velocity from the feeding tool, U_{dc}, and the vibration speed, U_{us}, of the tip in the following equation:

$$U = U_{dc} + U_{us} = U_{dc} + u_0 \cdot e^{j\omega t} \tag{2.3}$$

where u_0 is the vibration amplitude, ω is the angular velocity and t is time.

The ultrasonic insertion can divide into three different phases: 1) the tip is moving into and cutting the tissue (active phase), 2) the tip is retracting away from tissue

(passive phase) and 3) the tip is approaching the tissue (passive phase). In the active phase, the actual cutting velocity approaches its maximum. As deformation per loading, cycle remains very small, cohesive bond in the tissue subjected to enormous stress. Time-dependent stress relaxation does not occur due to high-frequency cycle loading. The high deformation velocities virtually increase the stiffness of the tissue, therefore inducing local cleavage and a conversion from the ductile to brittle fracture. This results in reduced deformation and damage of the tissue and cut face. Both cutting force and energy necessary for separation are significantly reduced.

During insertion of the tissue, the probe flanks, and separating surface are in permanent contact, and a relative motion occurs. Friction force, F_F, is defined as the force which acts against the relative motion of two contacting materials. The friction force is determined by the force normal to the contact surface, F_N, (tissue push again the probe flank) and the relative motion. When the probe is inserting into tissue, an alternating vibration velocity perpendicular to the normal force, but parallel to the contacted tissue and sliding direction directly affects the relative velocity between the contacting areas. The sliding velocity is as same as the cutting velocity, expressed in Equation (2.3). Despite a continuous movement, and alternating moving direction on a microscopic scale must also be considered. The friction forces consist of sliding friction and ultrasonic friction. When the sliding motion is the opposite direction to the motion induced by the ultrasonic vibrating cycle. Sliding is supported which, on a macroscopic level, leads to a reduction of friction. The average friction force [56] can be express with as

$$F_F = \begin{cases} F_F & if\ \xi \geq 1 \\ \dfrac{2}{\pi} sin^{-1}(\xi)F_F & if\ -1 < \xi < 1 \\ -F_F & if\ \xi \leq -1 \end{cases} \qquad (2.4)$$

26

where ξ is the dimensionless velocity ration defined as

$$\xi = \frac{U_{DC}}{U_{us}} \tag{2.5}$$

From Equation (2.4), the friction force reduction diminishes when as the sliding velocity increases. For the feeder velocity of 2 mm/s and the ultrasonic vibration velocity of 548.13 mm/s, 30 V_{pp} driving voltage, the friction force can reduce by 87%.

Nabibasdekov and Plyushchenkov presented a successful model for ultrasound enhanced insertion into soft tissues [57]. Their fundamental assumption was that the force required to penetrate tissue is a constant threshold and frictional forces in fluid and tissue are negligible. Furthermore, effects of cavitation and microstreaming are not considered. The force acting on the cutting edge of the probe includes three different forces: 1) the feeding tool applies a steady force, F_x, to the neural probe which acts against the tissue being cut. 2) The force generated by the vibration transducer. 3) The tissue reaction force, f_r. Summing up these forces, the differential equation of motion for the neural probe acting against tissue can be expressed as

$$M\ddot{x} = F_x - mA\omega^2 \sin(\omega t + \varphi) - f_r \tag{2.6}$$

where the force generated by the section of the tip that is cutting the tissue can be written as the product of acceleration, ωA (ω is the angular frequency and A is the transducer tip displacement amplitude, and the effective mass of the tip, m. In the case of a resonator half-wavelength long, the effective mass is from the tip to the first displacement node (the front quarter-wavelength section). The tissue reaction force, f_r, can further expand into three different forces, 1) tissue reaction force, f_0, 2) a viscous

damping term, k_1, and 2) nonlinear dependence on velocity, k_2. The total force, F_t, can be monitored by a load cell (Figure 2.4). Equation (2.6) can be rewritten as

$$F_t = F_x - mA\omega^2 \sin(\omega t + \varphi) - f_0 + k_1 \dot{x} + k_2 \dot{x}^2 \tag{2.7}$$

where $\dot{x}$ is the feeding tool insertion velocity. Since the friction force in fluid and tissue is assume negligible, only the active phase is responsible for force contribution. Therefore, the force from the ultrasound oscillation can be substituted into a constant, γ, times the driving voltage, V, of the transducer, which will determine the oscillation amplitude. Moreover, the tissue reaction force, f_0, and the viscos term, k_1, are depends on the tissue properties and the non-linear term, k_2, can be ignore in the slow insertion velocity (2 mm/s). Therefore, equation (2.7) can be simplified as

$$F_t = \alpha Y + \beta Y \dot{x} + \gamma V + \delta \tag{2.8}$$

where, Y is the tissue properties (percentage of agar gel), which is an indication of the elasticity of the material, V is the applied driving voltage of the transducer, α, β, γ, and δ are constants. By performing a non-linear regression χ-squared minimization function with experimental results on the known substrates, transducer driving voltages, and insertion speeds [58], equation (2.8) was fitted as

$$F_t = (5.90 \pm 0.52)Y + (1.18 \pm 0.26)Y\dot{x} - (0.30 \pm 0.18)V - (3.93 \pm 0.97) \tag{2.9}$$

From equation (2.9), the calculated insertion force without ultrasonic actuation for 2% agar gel is 12.9 mN, this is comparable to the result from [42] for 100 μm diameter flat punch stainless steel cylindrical probe without removing dura and pia mater (11.594 mN) and our *in-vivo* measurement result (Figure 2.18). While applying the ultrasonic

28
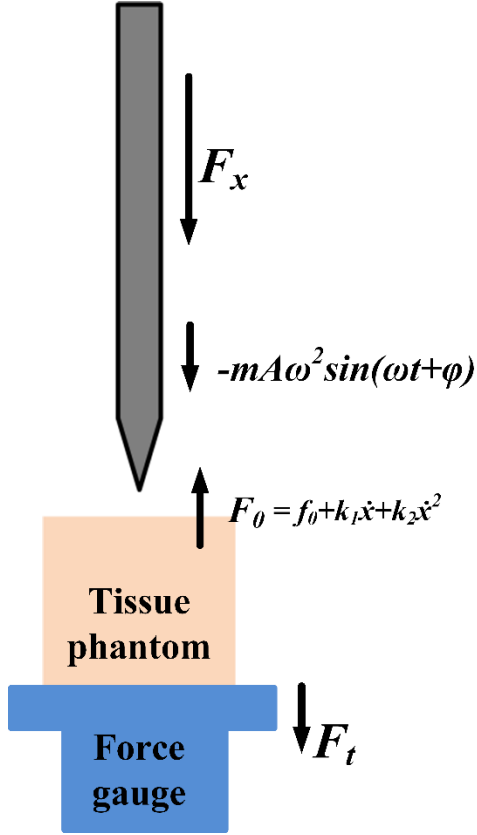
Figure 2.4: Insertion force modeling with ultrasonic assistance insertion. F_x **is the applied force, and** F_0 **is the tissue response force including a normal force,** f_0**, a viscous damping term,** k_1**, and nonlinear dependence on velocity term,** k_2**. The force from the ultrasonic vibration can be express as the effective mass of the probe,** m**, times the vibration amplitude,** A**, and angular frequency,** ω**. The overall force,** F_t**, can be measured from a force gauge.**

actuation through the horn, the high velocity vibration on the tip can reduced the penetration force. We expect that with sonic drive the zone of damage is less as cutting is confined to the tip. According to equation (2.9), the insertion force can be reduced by 3 to 9 mN with 10 V_{pp} to 30 V_{pp} driving voltage. The estimated force reduction agrees with our *in-vivo* measurement results (Figure 2.18).

2.2.3 Secondary effects of ultrasound

Due to the non-ideal elastic behavior of tissue, acoustic wave does not propagate indefinitely, but the energy of the wave declines by a conversion of mechanical energy into thermal energy. Depending on residence time and the amount of the converted energy, absorption causes an increase in tissue temperature. The major absorption loss is viscous loss. Viscous losses occur whenever there is relative motion between adjacent portions of the medium. From Navier-Stokes equation

$$\rho\left(\frac{\partial u}{\partial t} + u \cdot \nabla u\right) = -\nabla p + \eta \cdot \nabla^2 u + f \tag{2.10}$$

where ρ is density of medium, u is the velocity of ultrasonic vibration, p is the pressure, η is the viscosity coefficient, and f is the external force. Assuming external force and pressure gradient are not presented, and the medium is incompressible. Equation (2.10) can be simplified as

$$\rho\frac{\partial u}{\partial t} = \eta\frac{\partial^2 u}{\partial z^2} \tag{2.11}$$

The velocity of ultrasonic vibration can be written as

$$u = u_0 e^{\frac{z}{\delta}} e^{j\omega t} \tag{2.12}$$

where u_0 is the amplitude of the vibration. Substituting Equation (2.12) into Equation (2.11), we can get the following expression

$$\rho j\omega = \frac{\eta}{\delta^2} \tag{2.13}$$

Rearranging (2.13), δ can be expressed as

$$\delta = \frac{\sqrt{2}}{1+j}\sqrt{\frac{\eta}{j\omega}} \tag{2.14}$$

From Equation (2.14), Equation (2.12) can be rewritten as

$$u = u_0 e^{-\frac{z(1+j)}{\sqrt{\frac{2\eta}{\rho\omega}}}} e^{j\omega t} = u_0 e^{-\frac{z}{\delta_0}} e^{j\left(\omega t - \frac{z}{\delta_0}\right)}$$

$$\tag{2.15}$$

$$\delta_0 = \sqrt{\frac{2\eta}{\rho\omega}}$$

where δ_0 is the viscous penetration depth, the acoustic boundary layer thickness. The mechanical power loss into medium can express as force, F, times, velocity, u. The force can be written as

$$F = WL \int \eta \frac{\partial^2 u}{\partial z^2} dz \tag{2.16}$$

where *W* and *L* are the dimensions of the probe tip. From Equation (2.15) and Equation (2.16), the total mechanical power loss into medium can be estimated as

$$P = F \cdot u = WL\eta \frac{\partial u}{\partial z} \cdot u \cong W \cdot L \cdot \frac{\eta}{\delta_0} \cdot u^2 \tag{2.17}$$

Studies [59], [60] have shown an increase in temperature of up to 65 ℃ was observed when using ultrasonic scalpels for cutting of flesh tissue. The ultrasonic transducers they used are high-power low-frequency transducers (20-30 watts output power and 40-60 kHz operation frequency) made with titanium alloy, which has order-of-magnitude lower thermal conductivity than silicon. The good thermal conductivity property of silicon can help heat removal from the cutting area and reduced heat generation. Figure 2.5 shows a thermal image of the silicon-based ultrasonic neural probe operating at 408.95 kHz with different driving voltages over time in the air. The maximum increase of temperature is less than 1.5 ℃ after ten minutes of continuous operation. At least 4 ℃ temperature elevation is required for harmful bioeffects [61], and the thermal conductivity of silicon ($149\ W/m \cdot K$) is three orders of magnitude higher than biological tissue (Brain: $0.502 - 0.527\ W/m \cdot K$) [62]. During the neural probe implantation procedure, the ultrasonic actuation time is normally less than 20 seconds, depends on the depth of the implant. Most of the heat will be dissipated from silicon structure. Very limited amount of temperature elevation will not cause any tissue thermal damage during the ultrasonic enabled neural probe implantation.

2.3 *Integrated polysilicon piezoresistive strain gauge*

Conventionally, three type of materials are used to fabricate piezoresistors: metal, diffused single-crystal silicon, and diffused polysilicon. For metal piezoresistor, iron-nickel-chromium and iron-nickel-molybdenum are commonly used. Though thin film

IR image of the probe actuation under different driving voltages in air for 10 mins
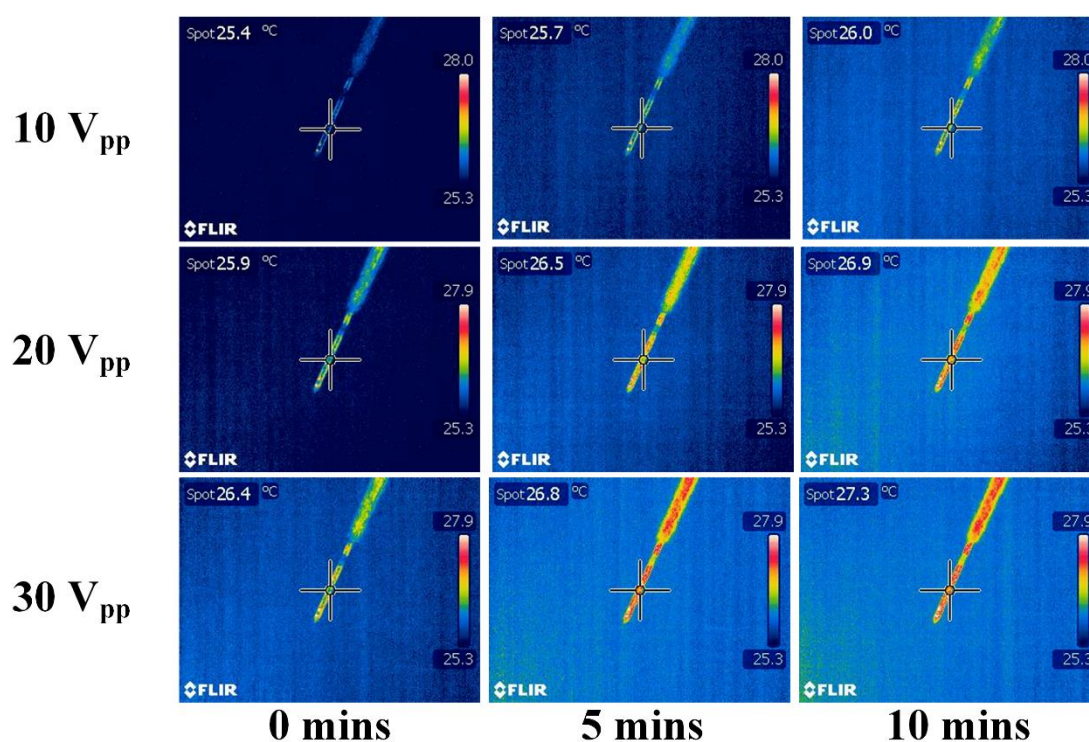
Figure 2.5: Heat generation for the ultrasonic horn transducer under different driving voltages over time in the air.

metal strain gauges are simple to fabricate and have a lower temperature coefficient, the gauge factors are relatively small, in the range of 2 or 3 [63], [64]. Diffused single-crystal silicon piezoresistor are fabricated by diffusing impurities into single crystal silicon in a shape amplifying strain in one direction. Though the single-crystal piezoresistors have higher gauge factors in the range of 50 to 150, this gauge factor is strongly non-linear as a function of temperature [65], [66]. Also, it can suffer from leakage current from the resistor to the substrate in the reverse biased isolation diode. Polysilicon has a larger gauge factor than metal by at least one order of magnitude, but smaller than that for single crystal silicon. However, polysilicon is less sensitive to temperature (low temperature coefficient of gauge factor, TCGF) by three times with proper fabrication, and results in lower offset voltage change due to temperature changes [67]. In a Wheatstone bridge configuration, the temperature-dependent common mode output can be eliminated, but the fabrication variations between each piezoresistors can still induce the offset voltage. The output signal change of polysilicon piezoresistor is a linear function of temperature. Moreover, polysilicon piezoresistors do not have leakage current to substrate because they can have a dielectric insulation layer between the piezoresistor and the substrate. In this work, we choose polysilicon as our piezoresistor material.

Two variable (R_1 and R_4) and two constant (R_2 and R_3) polysilicon resistors are arranged in a Wheatstone bridge configuration such that the strain sensitivity along the length of the needle structure is amplified over the other possible direction (Figure 2.6). As the probe cantilever bends, the resistance of the variable polysilicon resistors change allowing monitoring of the ultrasonic strain and the strain due to forces during penetrating tissue. In the strain gauge, the resistance of all four piezoresistor changes as a function of strain on the axis of principal stress. However, the strain experienced by R_1 and R_4 is significantly larger than R_2 and R_3 due to the thickness difference of the

Table 2.2 Piezoresistor materials summary

Material	Gauge factor	Pros and Cons
Metal	2 - 3	Simple to fabricate, low temperature coefficient
Diffused single-crystal silicon	50 - 150	Gauge factor is a strongly non-linear function of temperature. Also, it suffers from leakage current from the resistor to the substrate in the reverse biased isolation diode.
Polysilicon	Medium	Less sensitive to temperature, a linear function of temperature, no leakage current
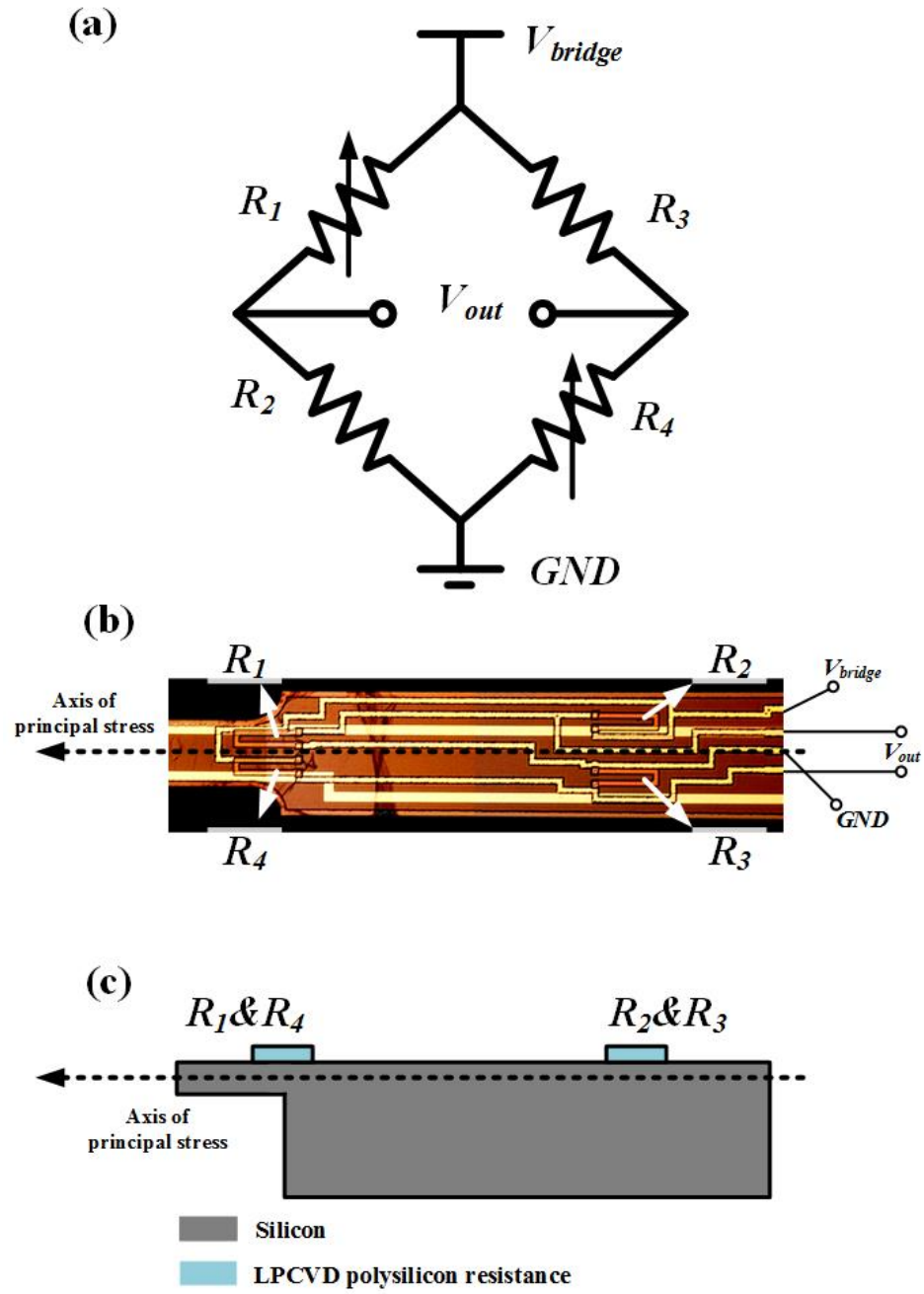
Figure 2.6: Schematic drawing (a), optical image (b) and cross-section (c) of the arrangement of piezoresistor in a Wheatstone bridge configuration.

silicon structure (Figure 2.6 (c)). By applying voltage V_{bridge} over the Wheatstone bridge, the output measured voltage depends on the non-variable resistor, R_2 and R_3 whose values are assumed to be approximately equal, and the variable resistor R_1 and R_4 which will have a resistance change of ΔR_1 and ΔR_4, assuming both resistor feels the same strain. The expression for the measured output voltage can be written as

$$V_{out} = V_{bridge} \left(\frac{R_4 + \Delta R_4}{R_3 + R_4 + \Delta R_4} - \frac{R_2}{R_1 + R_2 + \Delta R_1} \right) \tag{2.18}$$

To simplify the expression, assume that all four polysilicon resistors are identical with the same resistance, and R_1 and R_4 both feel the same strain. The expression from equation (2.18) can be rewritten as

$$V_{out} = V_{bridge} \left(\frac{R_1 + \Delta R_1}{2R_1 + \Delta R_1} - \frac{R_1}{2R_1 + \Delta R_1} \right) = V_{bridge} \left(\frac{\Delta R_1}{2R_1 + \Delta R_1} \right) \tag{2.19}$$

Assuming ΔR_1 is much smaller R_1 and a gain of A from an amplifier is used to amplify the output voltage. The output voltage can be further simplified as

$$V_{out} = A \cdot V_{bridge} \cdot \frac{\Delta R_1}{2R_1} \tag{2.20}$$

From equation (2.20), we can see that the output voltage is proportional to the resistance change, which is proportional to the strain experienced by the piezoresistive resistors.

The sensitivity of the piezoresistive strain gauge is governed by the gauge factor (GF), defined as

$$GF = \frac{R_s - R_o}{R_o \varepsilon} = \frac{\frac{\Delta R}{R}}{\varepsilon} \tag{2.21}$$

where R_S is the resistance with strain ε and R_o is the original resistance [68]. From equation (2.20) and (2.21), substitute $\Delta R/R$ with GF, the overall force sensitivity (S_F) can be expressed as

$$S_F = \frac{V_{out}}{F} = \frac{1}{2} \frac{A \cdot V_{bridge} \cdot GF \cdot \varepsilon}{F} \tag{2.22}$$

assume the cantilever is a linear elastic cantilever beam, the force sensitivity from equation (2.22) can be further expanded as

$$S_F = \frac{1}{2} A \cdot V_{bridge} \cdot GF \cdot \frac{1}{E_{silicon}} \cdot \frac{1}{Area_{tip}} \tag{2.23}$$

where $E_{silicon}$ is Young's modulus of silicon and $Area_{tip}$ is the cross section area of the tip.

The sensitivity of the piezoresistive strain gauge is limited by two primary sources of noise: thermal noise and flicker (*1/f*) noise [69].

Thermal noise: Thermal noise, the result of thermal motion of carriers within resistive elements, consists of both 1/f and white noise which is independent of frequency. The noise is dependent on the resistance R and temperature T of the resistor, and the noise power spectral density (V^2/Hz) for a single resistor is

$$\overline{S_t^2} = 4 k_B T R \tag{2.24}$$

where k_B is Boltzmann's constant. The thermal noise of a balanced Wheatstone bridge is equal to the thermal noise of a single resistor so that the overall thermal noise power of the Wheatstone bridge can be express as

$$\overline{V_t^2} = 4k_B \cdot T \cdot R \cdot BW = 4k_B \cdot T \cdot \frac{L}{W} \cdot \rho_s \cdot BW \qquad (2.25)$$

where BW is the frequency bandwidth of operation, L is the length of the piezoresistor, W is the width of the piezoresistor and ρ_s is the sheet resistance of piezoresistive material.

Flicker (1/f) noise: Flicker noise is a fluctuation in resistor conductance which can be attributed to defects in the bulk of the material. In contract with thermal noise, which is a voltage noise, flicker noise is a conductivity noise and the noise voltage depends on the bridge voltage. The noise is independent of the resistance and is inversely proportional to the number of carriers in the resistor. The voltage power spectral density of a single piezoresistor has been empirically modeled as

$$\overline{S_f^2} = \alpha \frac{\left(\frac{1}{2}V_{bridge}\right)^2}{Nf} = \alpha \frac{\left(\frac{1}{2}V_{bridge}\right)^2}{D \cdot L \cdot W} \frac{1}{f} \qquad (2.26)$$

where α is Hooge's constant, N is the total number of carriers in the resistor, D is dose of ion-implantation, L is the length of the piezoresistor, W is the width of the piezoresistor and f is the frequency. The Wheatstone bridge is composed of two piezoresistor which are uncorrelated *1/f* noise source so the *1/f* noise power is increased by a factor of 2 (voltage increased by $\sqrt{2}$), and the integrated voltage noise power is

$$\overline{V_f^2} = \frac{\alpha V_{bridge}^2}{2 \cdot D \cdot W \cdot L} ln\left(\frac{f_{max}}{f_{min}}\right) \tag{2.27}$$

where BW is the bandwidth of operation and f_l is the lower cut-off frequency.

The minimum detectable force (F_{min}) can be calculated from the integrated voltage noise and the force sensitivity (Equation (2.23)) of the piezoresistive strain gauge as

$$F_{min} = \frac{\overline{V_{noise}}}{S_F} \tag{2.28}$$

where $\overline{V_{noise}}$ is the sum of the uncorrelated noise source from Equation (2.25) and equation (2.27). The overall root mean square voltage noise can be written by

$$\overline{V_{noise}} = \sqrt{\overline{V_t^2} + \overline{V_f^2}} \tag{2.29}$$

The minimum detectable force and the force sensitivity depends on the piezoresistor design, silicon cantilever, and the operation frequency range. Decreasing the size of the piezoresistor can increase the strain measurement localization. However, with the smaller piezoresistor, high resistance will increase both thermal and flicker noise [70]. From Equation (2.23), we characterized the integrated strain gauge in Wheatstone bridge configuration with cantilever dimensions of 3 mm in length, 100 μm in width and thickness, 10 volts peak-to-peak bridge voltage and 65 dB amplifier gain with resulting gauge factor of 23.7 and the force sensitivity of 140 V/N. The Johnson noise of the strain gauge is 1.87×10^{-14} V^2 and the flicker noise is 1.15×10^{-12} V^2. From Equation (2.28), the minimum resolvable force is calculated as 7.76 nN.

2.4 *Device design, fabrication, and characterization*

2.4.1 Structure design

To enable ultrasonic vibration for a neural probe during insertion, a silicon-based neural probe co-fabricated with a catenoidal ultrasonic horn is designed (Figure 2.7). The detail of designing silicon ultrasonic horn is described in Chapter 1.2. A prong with a width of 100 μm off the main horn forms the neural probe. The prong consists of two platinum electrical sites (35μm $\times$ 35μm) and integrated strain gauges at the interface of the horn and the prong for optimum strain measurement. As the tip bends, the resistances on the variable polysilicon resistors change allowing monitoring of strain on the probe. Including holes (60 μm $\times$ 60 μm, with 80 μm pitch) in the probe tip may help promote biocompatibility or allow for better signal transduction. Sieve electrodes have been often used in nerve regeneration studies and peripheral nerve recording and have demonstrated promising results in allowing neurite growth and good electrical contact [71]. The mass of the tips are small compared with the mass of the ultrasonic horn and so do not significantly affect the motion of the horn. A Matlab GUI (graphical user interface) program is developed to quickly generate different ultrasonic horn dimension with neural probe in CIF (Caltech intermediate form) format (Appendix 6.1).

2.4.2 Fabrication process flow

The fabrication process flow, similar to [29], for the ultrasonic enabled neural probes are shown in (Figure 2.8). The process starts with four inches <100> silicon wafer coated with 600 nm thick film of LPCVD (low-pressure chemical vapor deposition) silicon nitride on both sides of the wafer. This insulation layer serves to isolate the metal signal line from the silicon substrate and impede the formation of Schottky electrical contacts. After LPCVD nitride deposition, 600 nm of LPCVD polysilicon is deposited. The polysilicon film is then ion-implanted with boron at a dose of $2\text{x}10^{15}$ ions/cm^2 at 100 keV with 7 degrees of tilt angle. The measured sheet resistance of the film, after

(a)

Catenoidal horn ultrasonic transducer

Neural Probe

1.4 mm

2.3 mm

6.4 mm

2.5 mm

3 mm

10 mm

(b)

Polysilicon piezoresistors

60 μm x 60 μm holes in the probe tip

80 μm

35 μm x 35 μm Platinum electrode

250 μm

100 μm

3 mm
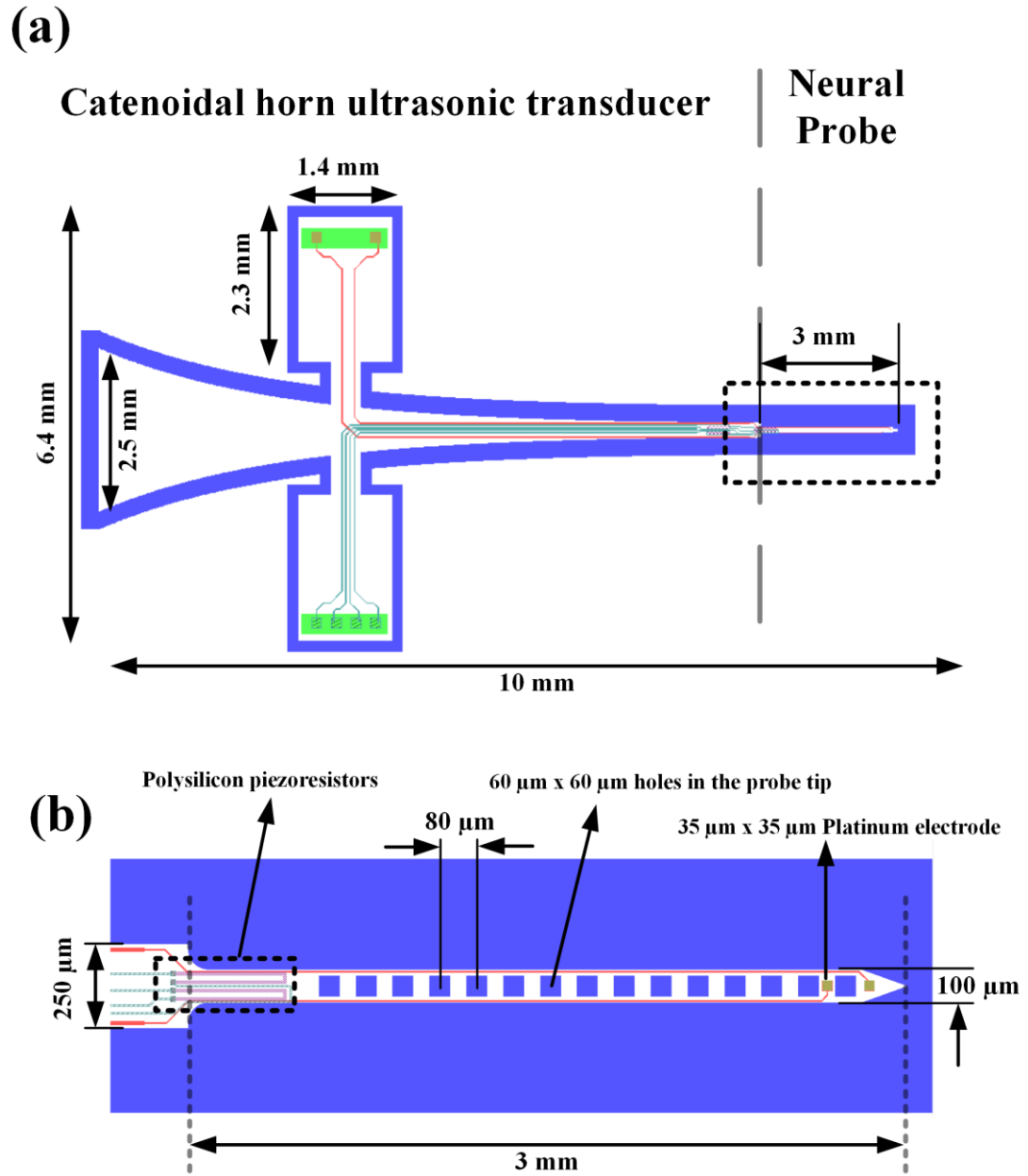
Figure 2.7: Layout of the integrated neural probe (a) Catenoidal horn and neural probe and (b) integrated polysilicon piezoresistors and platinum recording electrodes.

42

annealing in nitrogen at 950 $^\circ$C for an hour, is around 180-190Ω/□. After polysilicon annealing, 300 nm of thermal oxide is grown on top of the patterned polysilicon as an insulation layer for the polysilicon piezoresistors and patterned to expose the polysilicon to form electrical contacts. Aluminum alloy (aluminum + 1% silicon) metal lines are sputtered for the electrical contact to the pizeoresistors. The wafers are then annealed at 250 $^\circ$C with 5% hydrogen and nitrogen again to activate the dopants and produce a good contact between the aluminum and polysilicon. Insulating PECVD (plasma-enhanced chemical vapor deposition) low-stress nitride is deposited at 250 $^\circ$C to ensure thermal compatibility with the low melting temperature metal on the wafer, followed by platinum evaporation to define electrical recording sites. Platinum is selected as the metal interface to the electrolyte due to its good biocompatibility and chemical stability. To promote adhesion of platinum to silicon nitride, a 25 nm layer of chrome is evaporated first as an adhesion layer followed by 250 nm of platinum. Another insulating PECVD low-stress nitride is deposited to define the electrical recording sites and the bond pad area. Two step of the DRIE (deep silicon reactive ion etch), front-side and back-side, is performed to release the shape of the structure. The probe tip thickness, 100 μm, is define by front-side DRIE with careful control of etching loops. For back-side etching, a polymer coating, Protek SR-25, is spun to protect the front-side feature during DRIE probe release. The detailed process recipe and tool parameter is listed in Appendix 6.2.

2.4.3 Device assembly

A dummy horn structure without prong is adhesively bonded to the device for balancing the transverse motion during ultrasonic actuation. Two PZT piezoelectric plates ($3.55 \times 1.25 \times 0.5$ mm^3) are affixed to the zero-displacement nodes of the longitudinal mode shape. The PZT is actuated at its $\lambda/2$ resonance, which matched to
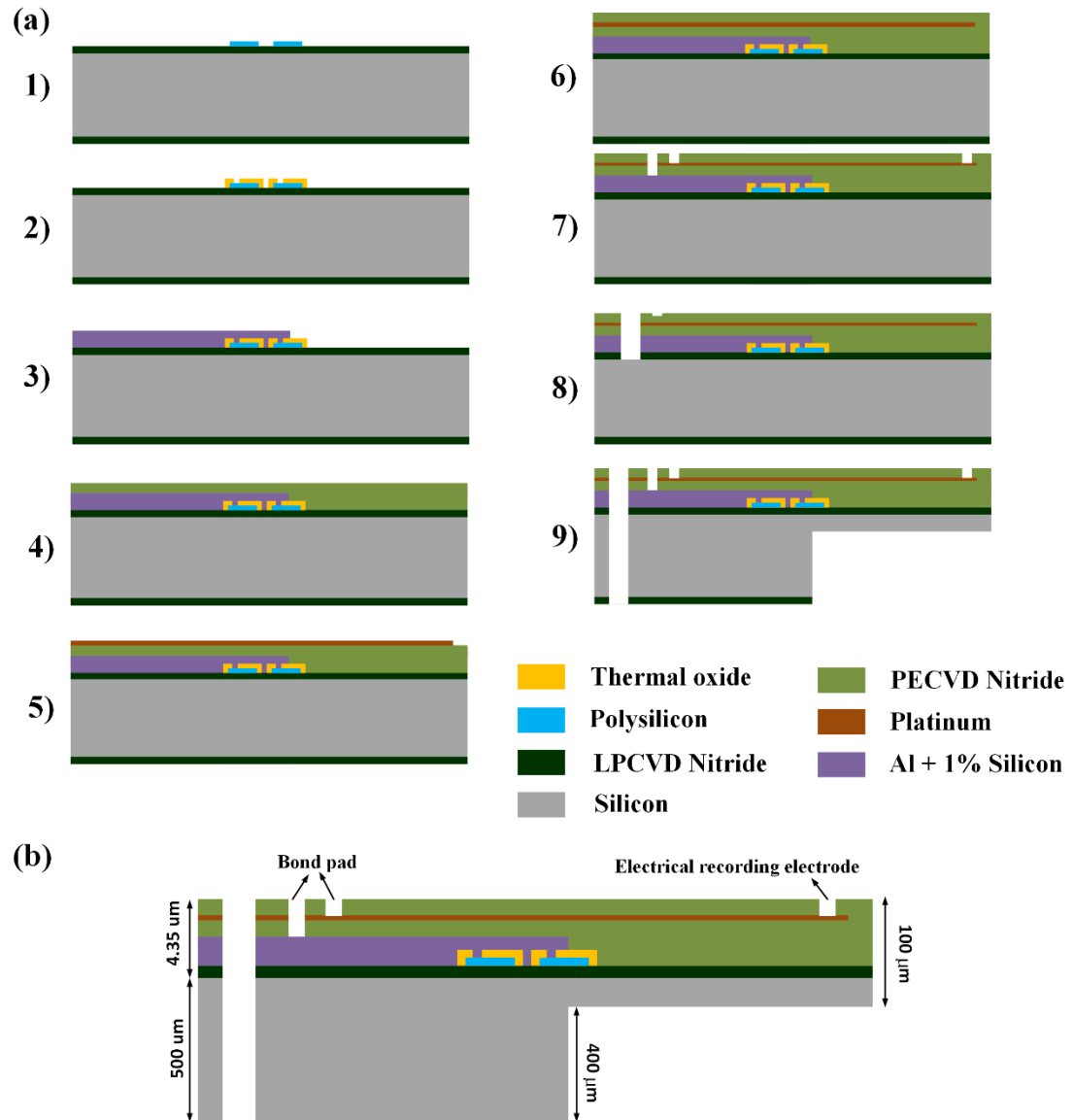
Figure 2.8: Fabrication process flows for ultrasonic neural probe with integrated strain gauges.
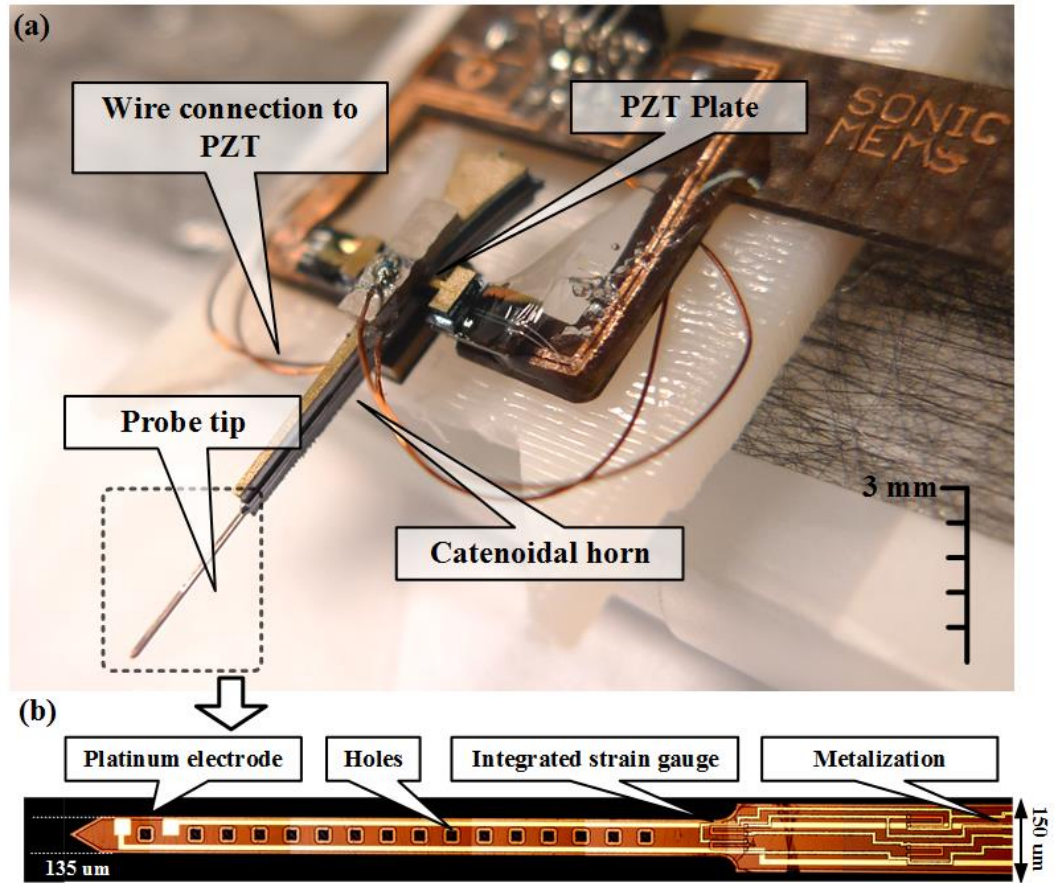
Figure 2.9: Picture of the final device (a) Miniature silicon horn with piezoelectric plates to drive the probe at its longitudinal resonance. (b) Microphotograph of probe tip with integrated strain gauges and platinum recording sites.

the longitudinal resonance of the silicon probe to maximized the energy coupling from PZT plates to the silicon structure. The entire structure is then placed on a custom printed circuit board (PCB) with a 3D printed head stage for the chronic animal implantation (Figure 2.9).

2.4.4 Device characterization

2.4.4.1 Ultrasonic transducer characterization

Finite element simulation of the ultrasonic neural probes indicates that the longitudinal resonance frequency is around 408.95 kHz (Figure 2.10). The silicon horn displays an approximately four-fold displacing amplification between the end of the probe and the tip of the probe. Interferometric measurements of the ultrasonic horn displacement were performed to verify the probe tip displacement through a frequency range around the anticipated longitudinal resonance frequency. The interferometer measures the phase shift between a laser directed at the sample and a reference laser beam (Polytec OFV2700). A Stanford Research Systems lock-in amplifier (SR 844) was used to extract the amplitude and phase of the measured interferometer signals with respect to the drive signals generated by a function generator (Agilent 33250A). LabVIEW code was used to control the function generator frequency and read in the lock-in amplifier data through a GPIB interface (Figure 2.11). Due to the limited interferometer range of focus, the probes were driven under sub 1 V_{pp} sinusoid waves, instead of the typical 10-30 V_{pp} used during neural probe insertion. As expected, the frequency sweep of the ultrasonic probe revealed the maximum displacement at a frequency of 418.13 kHz (Figure 2.12), which matches closely to the longitudinal resonance of the ultrasonic probe (408.95 kHz) given by finite element simulations. Small variations in probe longitudinal resonance are expected to arise from fabrication tolerances and bonding alignment. The measured values of oscillation amplitude under different driving voltages and fit are shown in Figure 2.13. Assuming an approximately linear PZT drive and tip displacement relation which would hold given a general forced response to a sinusoidal input driving function, the tip displacements for the probe with driving voltage can be estimated as
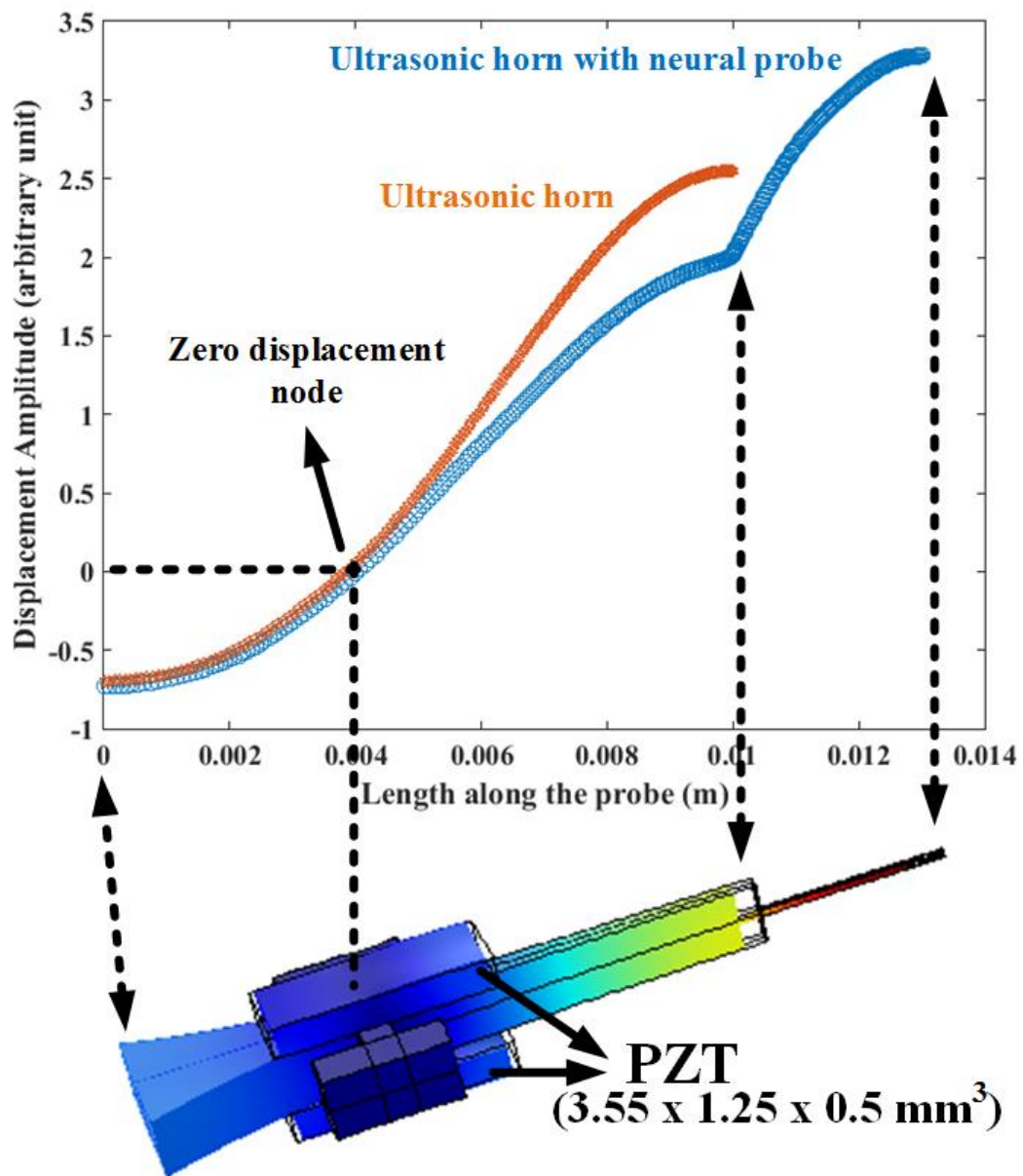
Figure 2.10: Finite element simulation for the displacement amplitude of the longitudinal mode with and without the integrated probe.
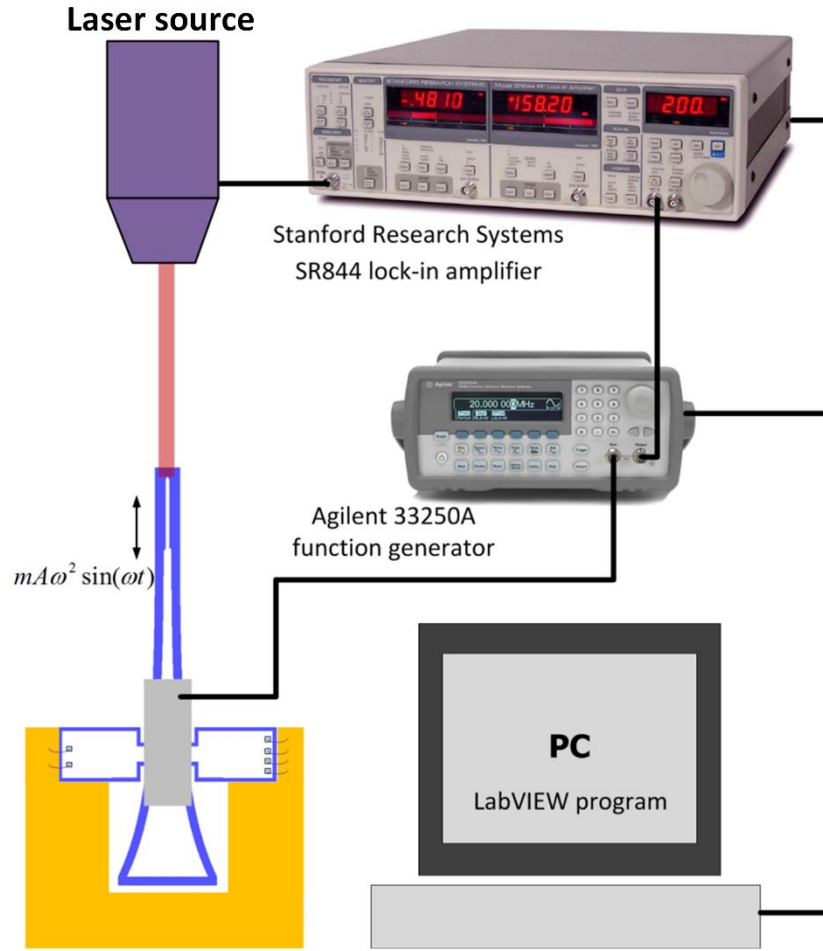
Figure 2.11: Interferometer measurement setup.

$$Amplitude\ (nm) = 7.11 \times Voltage(V) + 0.0234 \qquad (2.30)$$

From Equation (2.30), the estimate tip displacement amplitudes at driving voltages of 10, 20 and 30 V_{pp} are 71.12 nm, 142.22 nm, and 213.32 nm, respectively. Using the expression $v = 2\pi f u_0$, (where v is the tip vibration velocity, f is the frequency and u_0 is the tip displacement), the tip vibration velocity than can be calculated as 182.74 mm/s, 365.44 mm/s, 548.13 mm/s, respectively, which are two order of magnitude higher than the insertion feeder velocity, 2 mm/s.
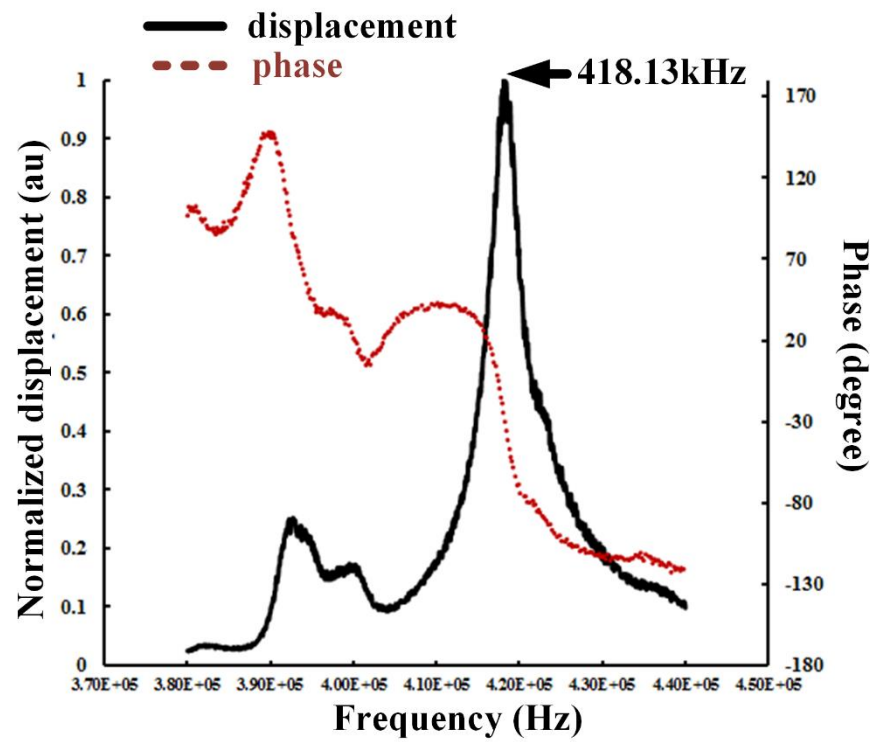
Figure 2.12: Interferometric measurement of the longitudinal displacement
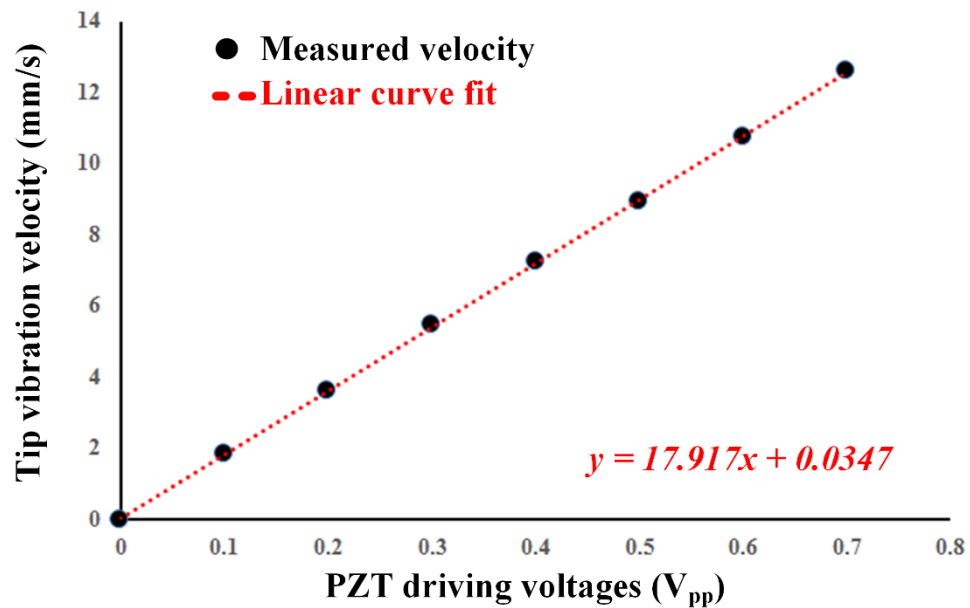
Figure 2.13: Probe tip vibration velocity versus driving voltages

2.4.4.2 Recording electrode impedance characterization

Electrochemical impedance spectroscopy (EIS) is used to measure the electrode impedance. A three-electrode configuration is used with a Gamry FAS2 potentiostat, with the setup shown in Figure 2.14. The silicon ultrasonic probe serves as the working electrode whose impedance is of interest. A platinum sheet with a larger area (2 cm^2) compared to the working electrode (35 μm) is used as the counter electrode, and a silver/silver chloride (Ag/AgCl) probe is used as the reference electrode. Cyclic voltammetry is first performed on the electrode sites to allow cleaning of the electrode surface prior to impedance measurements to remove any excess dirt. During the tests, the electrodes are immersed in 0.9% physiological saline. A 1 mV sinusoidal wave is applied between the counter electrode and the reference electrode. The resulting current required to maintain a constant voltage between the working electrode and the reference electrode is measured. The electroe-electrolyte interface properties were measured and fit to the model presented in the previous chapter, with the spreading resistance R_s, the interfacial capacitance, Z_{CPA}, and the DC path characterized by the charge transfer resistance, R_{ct}. The measured and fit circuit parameters for the silicon ultraosic probes are shown in Figure 2.15 [72], [73].

2.5 *Miniaturized recording system*

The control system with multiple features, neural signal recording, ultrasonic transducer driving and sensing, and strain monitoring, of the ultrasonic neural probe, is developed (Figure 2.16). An integrated circuit was designed in AMS 0.35-μm process with low-noise neural amplifiers and a voltage controlled oscillator (VCO) as a radio transmitter for neural signal recordings (Appendix 6.4). A two-stage amplifier topology composed of differential stage followed by a common source stage resulted in a 1.25 µV input refereed noise and 50 dB gain over 10 kHz bandwidth. The VCO is designed
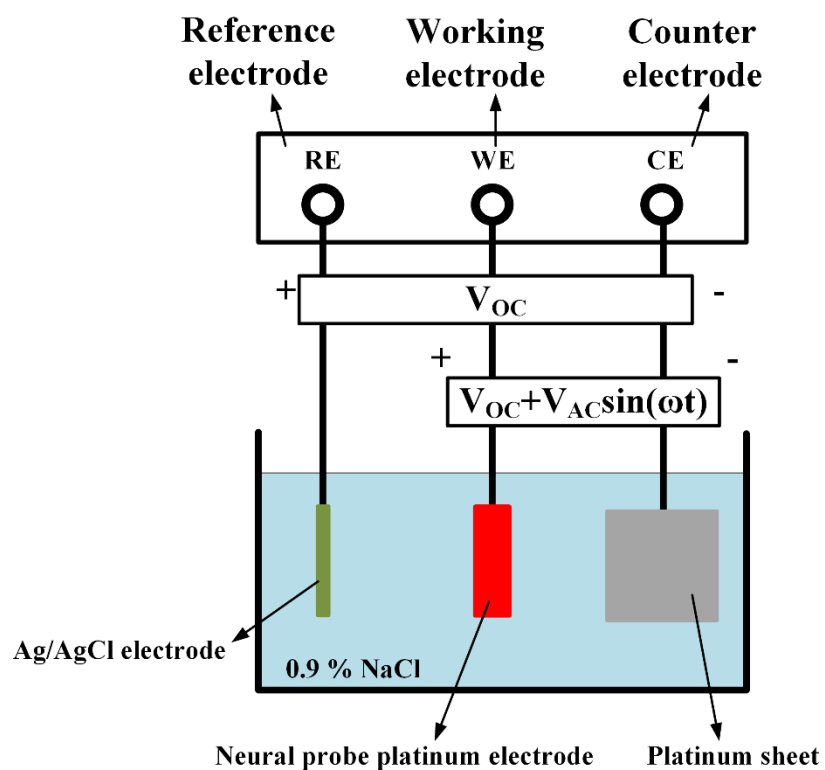
Figure 2.14: Experimental setup for electrochemical impedance spectroscopy (EIS). The counter electrode is a 2 cm² platinum sheet. The reference electrode is a nonpolarizable Ag/AgCl electrode, and the working electrode is the microfabricated probe of interest.

(a) EIS measurements

$OCP = -142.580\ mV$

(b) Equivalent circuit parameters

$Z_{CPA} = 1/(j\omega Q)^n$

Fitted values:

Rs	$7.76 \times 10^3\ \Omega$
Rct	$5.79 \times 10^9\ \Omega$
Q	9.37×10^{-11}
n	0.896
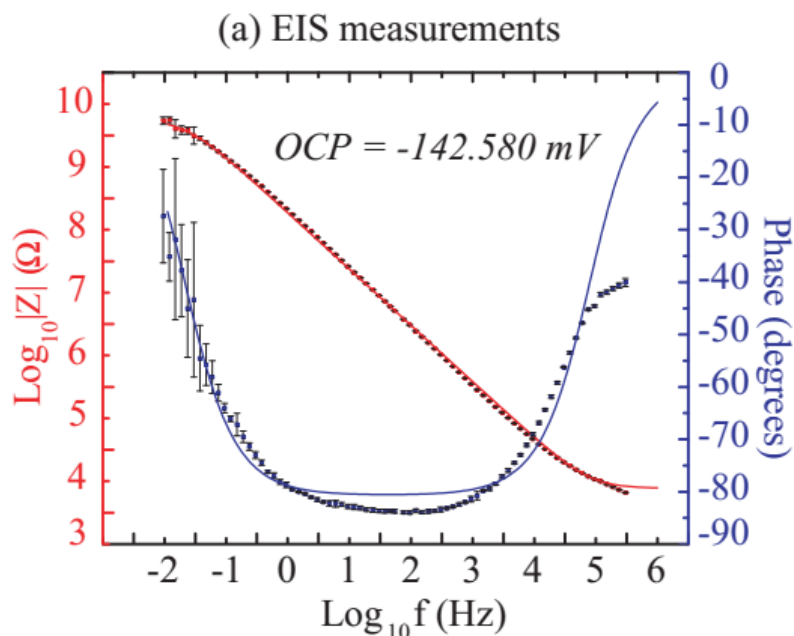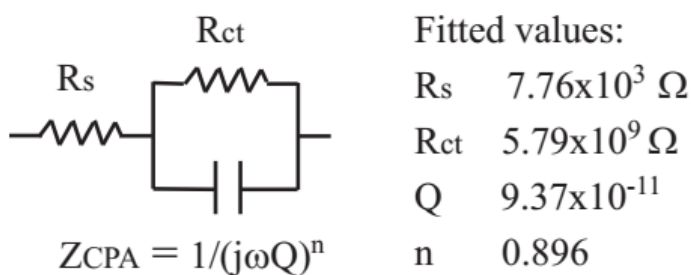
Figure 2.15: Measured and fit electrode-electrolyte equivalent circuit parameters. The equivalent circuit consists of a spreading resistance, R_s, a charge transfer resistance, R_{ct}, and an interfacial capacitance, Z_{CPA} (adapted from [72]).

using a differential ring oscillator topology to avoid external components. The telemetry frequency range is designed to be 82 to 84 MHz. The strain signal is amplified with an instrument amplifier with gain of 200 and sent to the analog-to-digital converter in the microcontroller (TI CC2530). A programmable waveform generator (AD9833) provides sinusoidal frequency waves with voltage amplitudes up to ±5V for ultrasonically actuating the probe. By performing a frequency sweep and locating the frequency at which the motion current through the PZT is greatest, we can measure the resonance frequency of the neural probe. Resonance frequency shifts are detected and monitored during insertion with different loading cells. A LabVIEW interface allows for user control and a ZigBee RF interface is used for wireless data transmission.
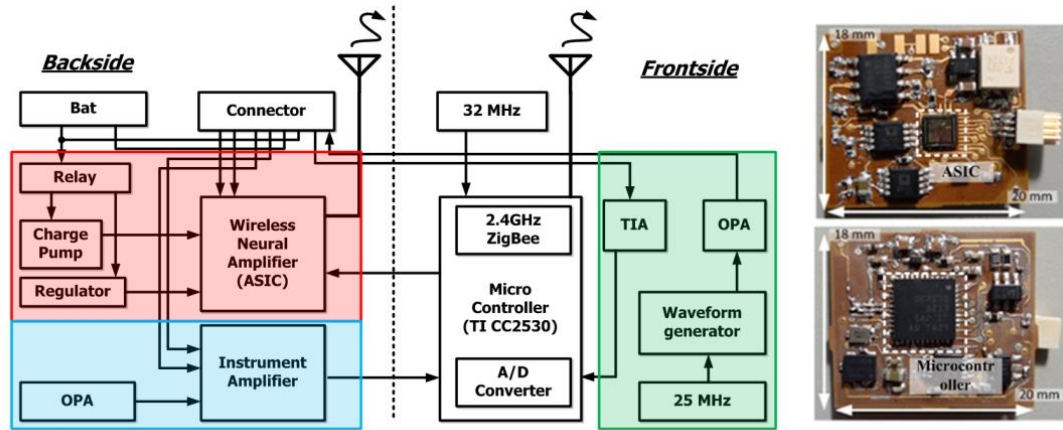
Figure 2.16: Block diagram of miniaturized control and recording system for ultrasonic neural probe. Different color correlated to the different functionalities: neural recording (red), insertion force (blue), and ultrasonic motion current monitoring (green).

2.6 *Experimental results*

2.6.1 Insertion forces reduction

The effect of ultrasonic actuation driven at different vibration velocity on the insertion force of the probe is evaluated and compared to the insertion force exhibited by regular insertion (no ultrasonic vibration). The ultrasonic horn is driven by PZT at different voltages at half wavelength frequency during insertion. The vibration velocities, 182.7 mm/s, 365 mm/s, and 548 mm/s, are controlled by the driving voltage of 10, 20, and 30 V_{pp}, respectively. Different driving voltages versus the insertion forces were characterized with a various percentage of agar gel as brain tissue phantom (Figure 2.17). A small initial peak occurs as the probe breaks through the surface of the substrate. The forces steadily increase as the shear and damping forces increase. Finally, probe motion is stopped in the substrate, and damping forces dependent on the insertion velocity disappear, revealing the residual force in the substrate. This force can be used to monitor excessive stress caused by insertion. The integrated stain-gauges were used to measure the longitudinal strain during the probe insertion *in vivo*. Total 16 mice with 160 insertions were performed with randomized location and driving voltages. Results demonstrate ultrasonic actuation in the cortex of the mouse significantly decreased the insertion force in a voltage-dependent manner (9.6 ± 0.7 vs. 3.8 mN $\pm$ 0.5, 0V vs. 30V, $p < 0.05$; Figure 2.18) and the average stress around the probe. Ultrasonic insertion causes the tissue-probe interface to have reduced insertion force by a factor of 2.6 and net-stress by a factor of 1.5, due to the ultrasonic cutting leading to less average stress and providing stress relief.
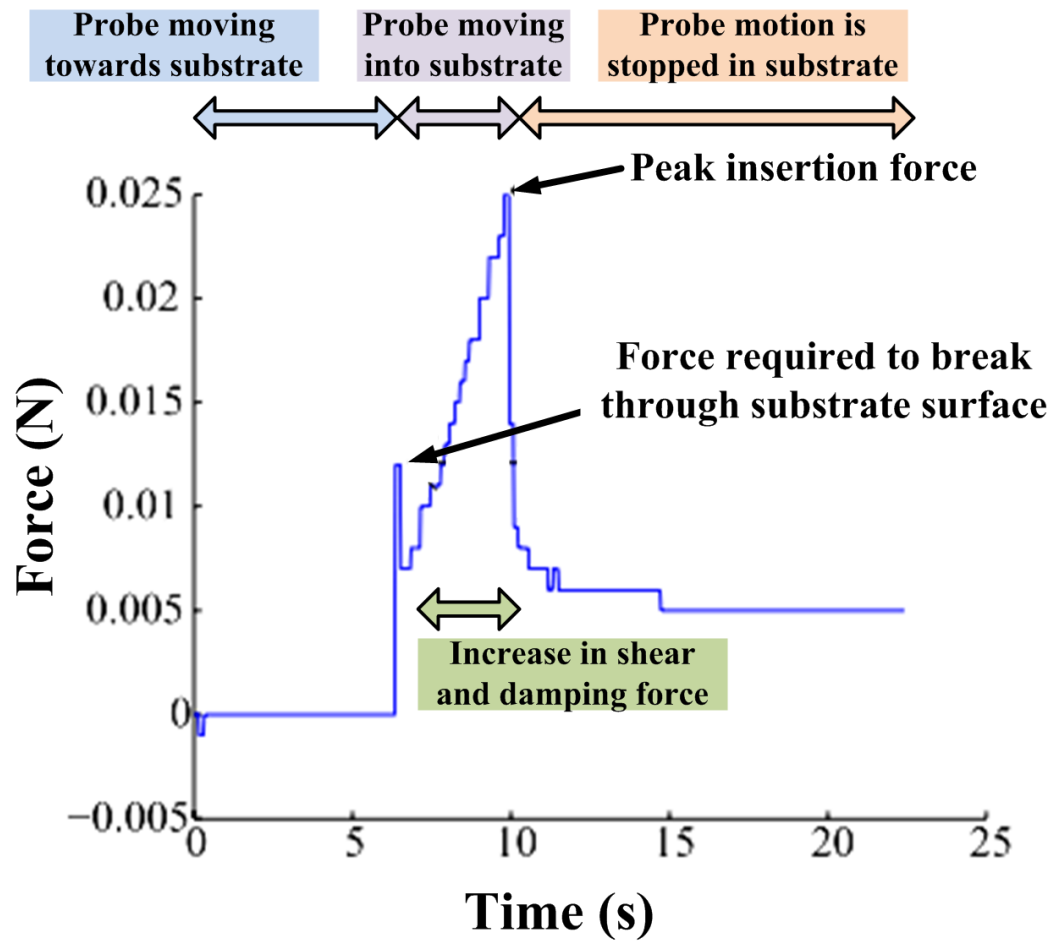
Figure 2.17: Measured insertion force profile for ultrasonic horn probe driven at 20 V_pp and inserted into 4% agarose at 2.4 mm/s. (adapted from [58])
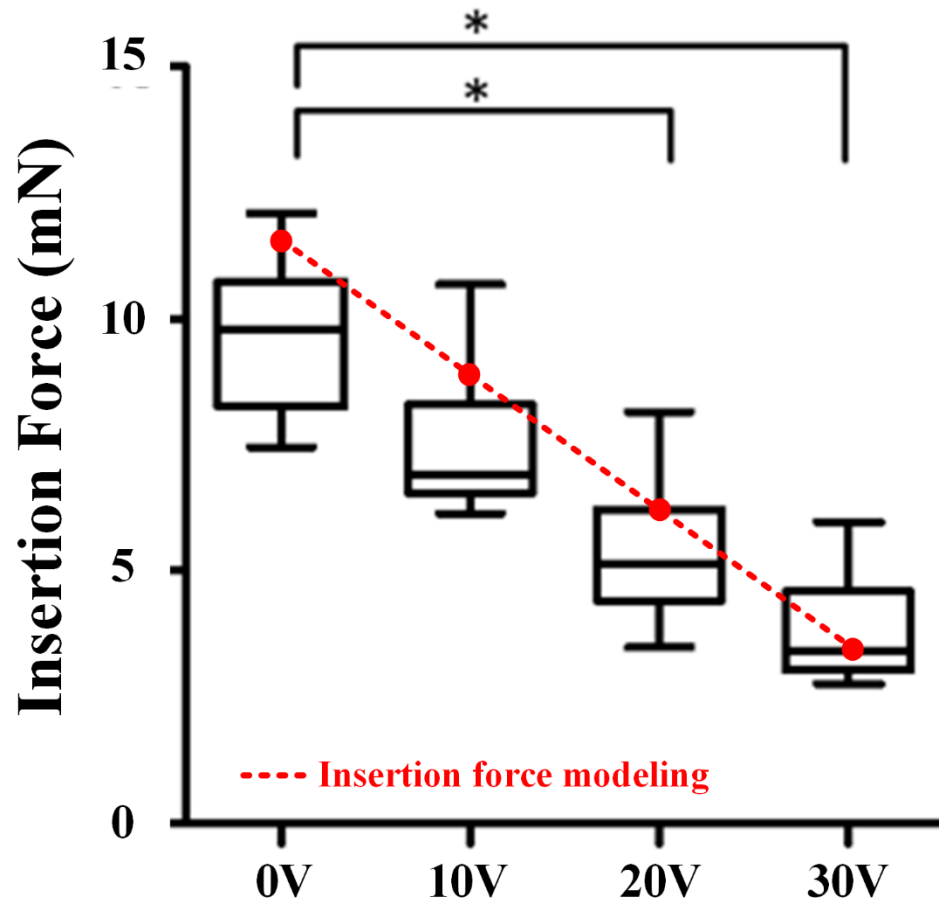
Figure 2.18: *In-vivo* **insertion force of different PZT driving voltages and the model predicted insertion force for 2% agar gel with 2 mm/s insertion speed (*p<0.05).**

2.6.2 Histology analysis

Histology analysis of the probe insertion sites is performed on the brain tissue sampled an hour after the insertion procedure. Mice were anesthetized and perfused transcardially with phosphate-buffered saline (PBS, pH 7.4, SigmaAldrich) followed by 4% paraformaldehyde (PFA) (ThermoFisher Scientific) in PBS. Following perfusion brains were removed and immersed in 30% (w/v) sucrose in PBS until saturated. For sectioning, brains were frozen in optimal cutting temperature (OCT) compound (Tissue-Tek), and 30 µm sections were cut on a cryotome (Microm HM550, ThermoFisher Scientific). Horizontal sections of the brain slice were captured with an Olympus BX41 wide-field fluorescence microscope (Figure 2.19) (The microglia cells were identified with green fluorescent protein (GFP)). From the horizontal tissue specimen, the initial area of tissue damage is evaluated. Compared to the area of control insertions (0V), actuation at 10, 20 and 30V significantly reduced damaged tissue, caused by the inserted electrode (56246 ± 6889 vs. 34141 ± 5613 pixels, 0V vs. 30V, p< 0.05; Figure 2.20). To characterize the shape of the hole, a measure of circularity was performed to determine whether the damaged caused was more "circular" vs. "jaggered." For example, a measure of 1 would indicate a perfect circle, 0 would be the least circular shape (or more jaggered). As illustrated in (Figure 2.19), insertion at 0V resulted in the damaged area consisting of highly jaggered edges, indicative of tissue that had been ripped during the act of insertion. In comparison, insertion with actuation created a more compact and circular hole (Figure 2.21).

Inflammation on the acute phase is evaluated by using microglia response. The number of microglia within a 200 μm area of the electrode track were quantified in 30 μm thick histological sections that were sectioned perpendicular to the electrode insertion direction. There was a trend in the reduction of microglia with increase actuation, compared to control, which only perform the craniotomy without probe
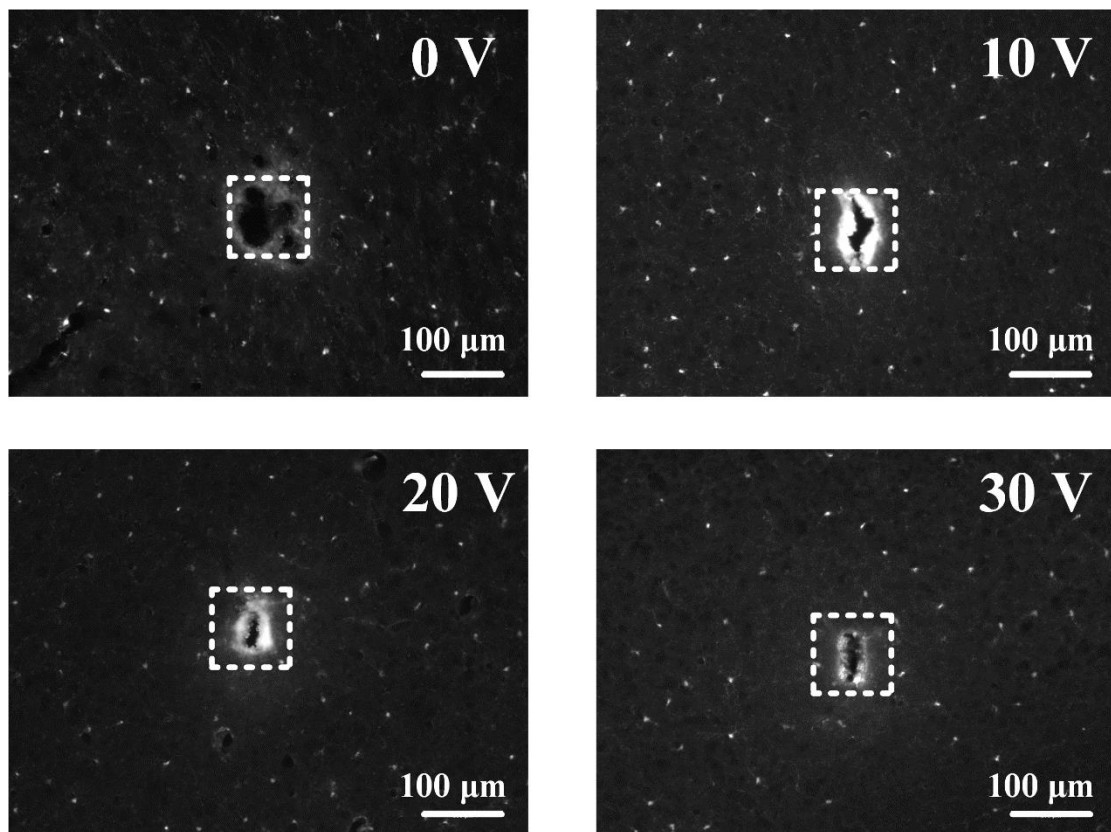
*microglia labeled with GFP

Figure 2.19: Histology slides of insertion spot after one hour post-implant with different ultrasonic driving voltage. The white dotted square is the insertion probe tip size, and white dot is the activated microglia cells labeled with green fluorescent protein (GFP).
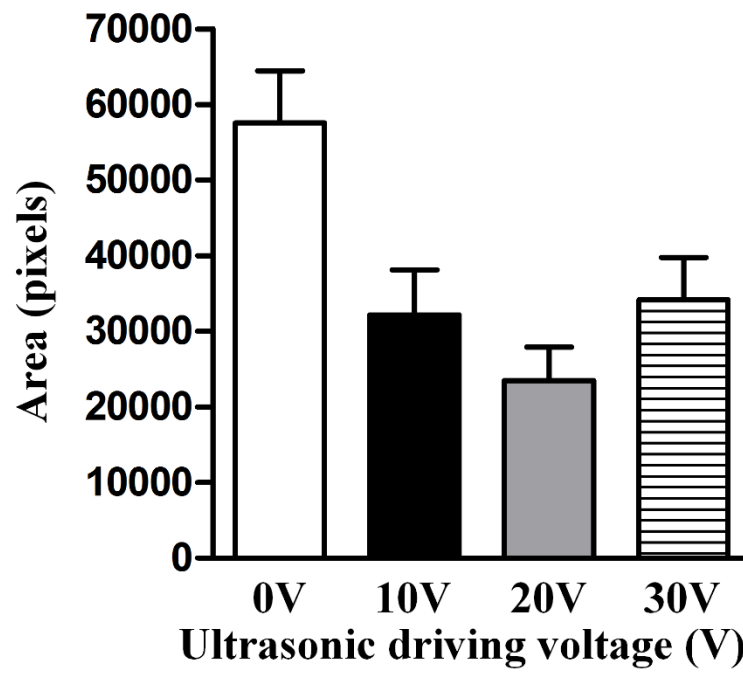
Figure 2.20: Area of the insertion site under different driving voltages.
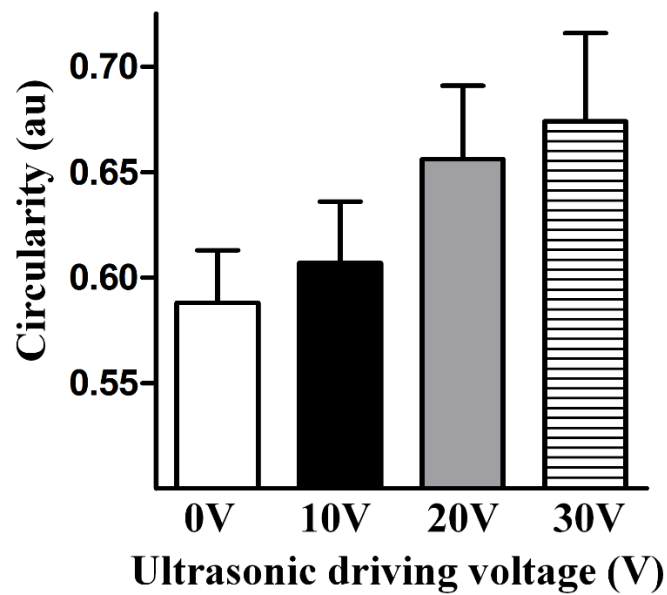
Figure 2.21: Calculation of the circularity over the insertion site with various driving voltages.

insertion. Figure 2.22 shows that number of microglia count under different driving voltage (56 ± 6 vs 34 ± 7 # microglia, 0V vs. 30V, $p<0.05$). Taken together, these data suggest that ultrasonic actuation during electrode insertion dramatically reduces acute microglial activation, to baseline levels, indicating a technological advancement to potentially increase neural microelectrode performance.

Collectively; these data demonstrate a reduction of insertion force, area damage, extent of damage, as characterized by circularity, and acute inflammation response with ultrasonic actuation. Based on these results we hypothesized the acute inflammatory response to ultrasonic neural electrode implantation would be attenuated due to a reduced insertion force thereby creating less tissue damage.
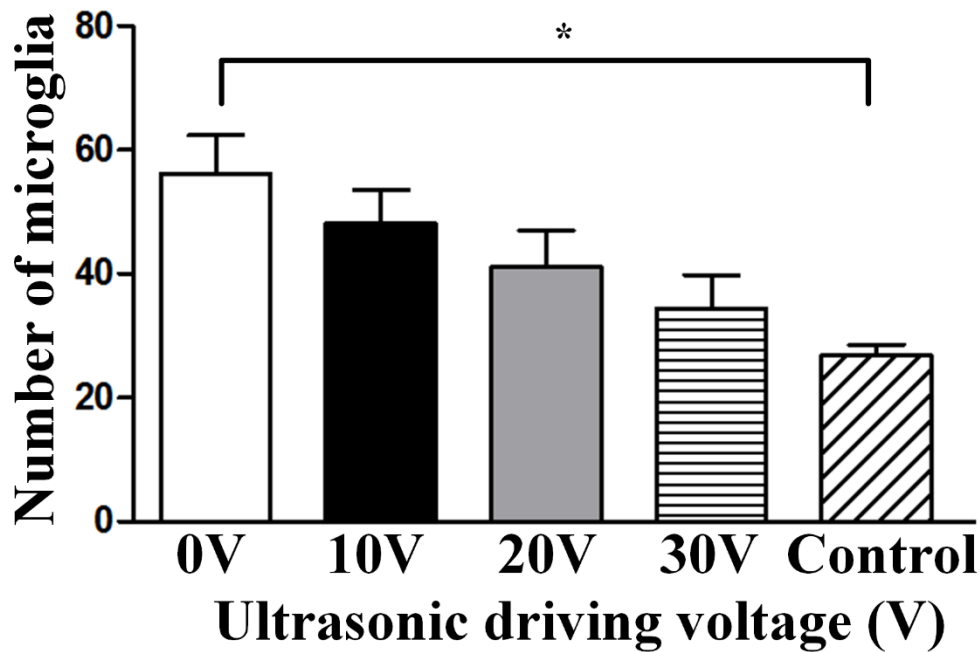
Figure 2.22: Number of Microglia count under different driving voltages. Control is the only craniotomy without any insertion (*$p<0.05$).

2.7 *Chronic optical and electrical recording over time*

To further evaluate whether actuation reduces the chronic inflammatory response. The neural probes are tested for biological efficacy by inserting them into the motor-sensory cortex region of genetically modified (cx3cr1) mice brain, which the microglia cells were identified with GFP. We used the advanced optical technique of two-photon excited fluorescence microscopy, and imaged the brains of transgenic mice that express fluorescent proteins in microglia through chronically-implanted cortical windows, centered over inserted electrodes (Figure 2.23). These ambulatory studies enabled us to identify dynamic interactions of microglia and to determine if they contributed to microelectrode failure. In addition, we investigated whether the immune response was reduced in response to actuation versus control electrode insertion. The chronic animal model implantation procedure and chronic studies results are described in the following sections.
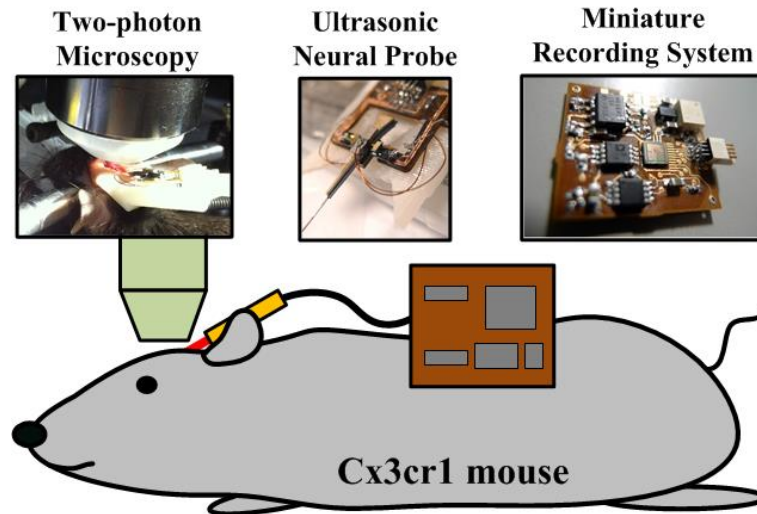
Figure 2.23: Chronic animal model with optical access window for two-photon excited fluorescence microscopy, ultrasonic neural probe, and miniature recording system.
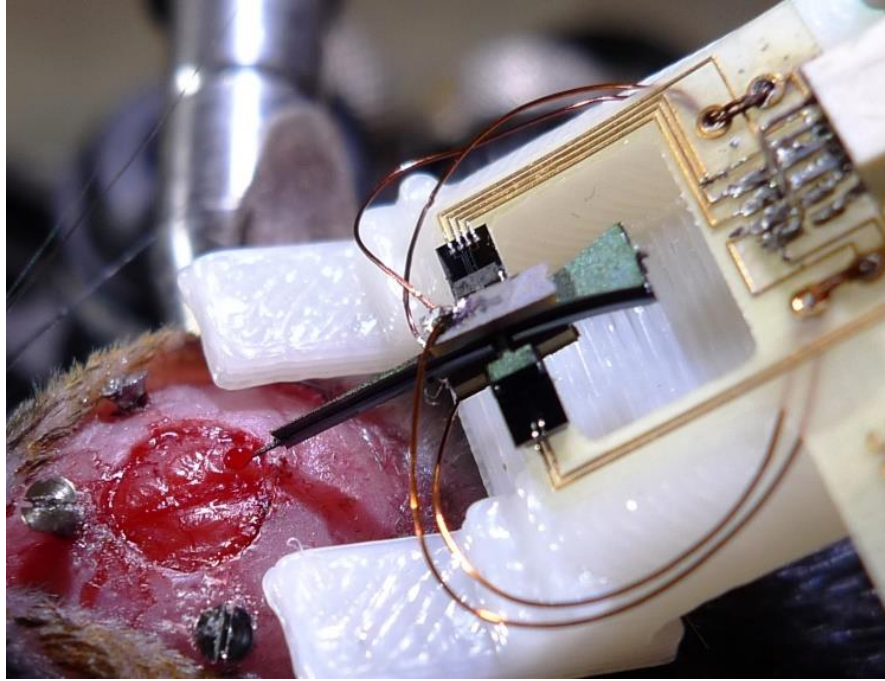
Figure 2.24: Picture of the implanted ultrasonic neural probe.

2.7.1 Chronic animal model preparation and implantation procedure

In-vivo implantation: Preoperative care is administered using aseptic techniques for chronic animals. For chronic surgeries, instruments and materials are sterilized by autoclaving. Anesthesia is administered by 5% isoflurane (VetOne) and is maintained at 1.5-2% for the duration of the experiment. At the beginning of the surgery, mice receive an injection of glycopyrrolate, an anticholinergic, intramuscularly at 0.002 mg/100g to assist in keeping the airways clear of fluid build-up and Ketoprofen (5 mg/kg) and Dexamethasone Sodium Phosphate (0.2 mg/kg) are administered subcutaneously. The mouse is secured in a stereotaxic frame by standard ear bars. After surgical preparation of the area on the head, bupivacaine 0.125% (~0.1 ml) is injected subcutaneously above the skull. A short incision is made on top of the mouse's skull, and the connective tissue is scraped away, exposing the bone. The dry skull is coated with a thin layer of cyanoacrylate adhesive (Vetbond). Three screws are placed in the

skull to provide a framework for the dental cement to create a strong adhesion. A 5mm diameter opening is drilled inside the chamber, leaving a bone flap in the center. After the bone flap is lifted off, the dura mater is kept moist with artificial cerebrospinal fluid (ACSF) and the chamber is filled with ACSF.

Insertion of electrode probe: The probe is secured and slowly lowered to the base of the craniotomy by a fine-precision motorized micromanipulator. The probe is gently inserted and advanced into the brain until it is approximately 200 µm under the surface of the cortex. The probe is secured to the base of the skull with dental cement. A glass coverslip is glued above the craniotomy site with cyanoacrylate and dental cement. The skin is closed around the margins of the cranial window with cyanoacrylate.

2.7.2 Chronic study results

A similar chronic neural recording trend, separated into four different stages [35], is observed (Figure 2.25). The signal-to-noise ratio (SNR) is defined as the average action potential peak-to-peak height (maximum – minimum, AP_{height}) divided by the standard deviation of the background noise (STD_{noise}) over 0.3 ms preceding all spikes and can be expressed as [74]

$$SNR = 20 \, log_{10}(\frac{AP_{height}}{STD_{noise}})$$

(2.31)

The recording failed over time and on the date of 48 post implantation. *In-vivo* chronic two-photon microscopy images shows the dynamic interactions of the microglia cells and the probe insertion site (Figure 2.26). On day 3, the image is blur due to hemorrhage causing by the neural probe implant, on the day 10, the microglia cells start to migrate toward the implant site, and on the day 21, a large amount of microglia completely cover the electrode sites, and the electrical signal begins to decrease and finally vanished. The
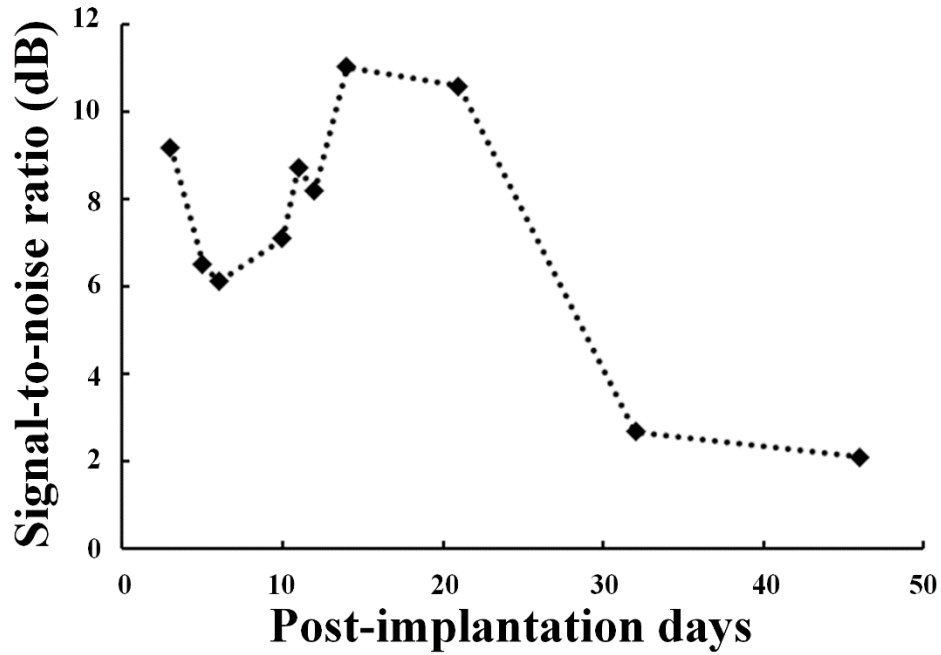
Figure 2.25: Signal-to-noise ratio versus post-implantation days.

functional recording days is longer in average with ultrasound actuated insertion versus non-ultrasound insertion (Figure 2.27). The percentage of the fractional volume of microglia cells, the population of microglia cells around the implant site, in the two-photon microscopy image is also quantified (Figure 2.28). The percentage of the fractional volume of the microglia cells is higher for the non-ultrasound actuated insertion than with ultrasound actuated. Total of 14 chronic mice, 7 with ultrasound actuation implant, 6 without ultrasound actuation implant, and 1 control (no implantation, only cortical windows) were studies.

2.8 *Conclusion and future directions*

The emerging field of neural interface technology has begun to provide valuable insights into electrode failure and as such, revealed a complex, multi-faceted problem. Therefore, therapeutic strategies will require interventions from many different angles.

64
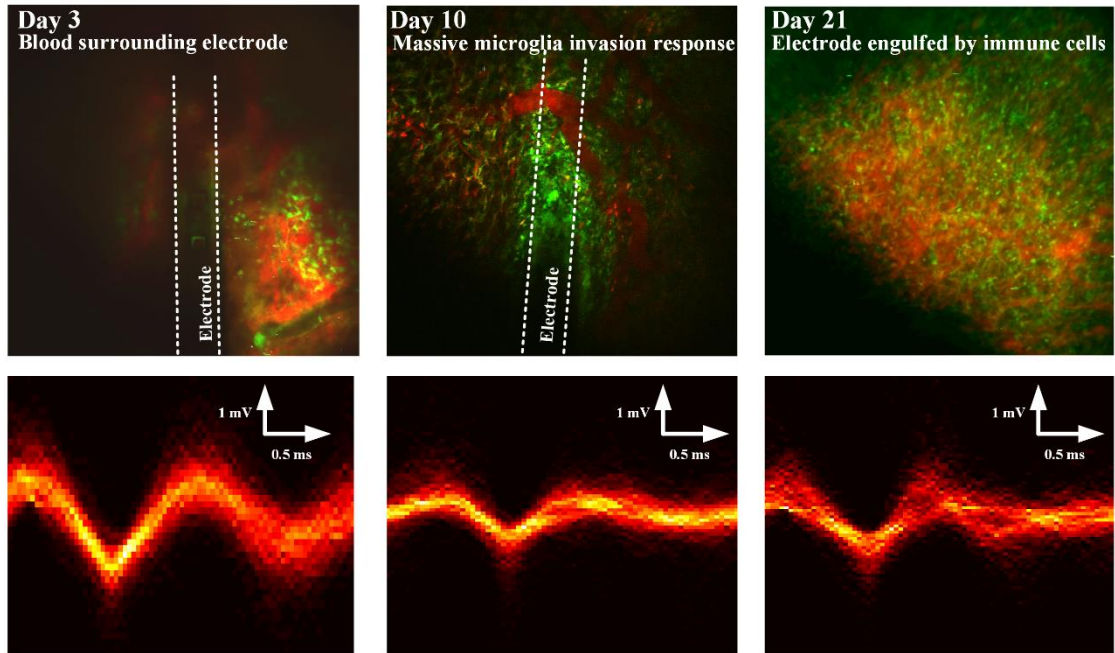
Figure 2.26: Two-photon image and electrical recording signal over time. The green fluorescent is microglia cell, and red fluorescent is the vasculature. In day 3, the two-photon image is blurry due to hemorrhage from the implantation. In day 10, massive microglial cells migrate to the implantation site. On day 21, recording electrode is engulfed by microglia cells.
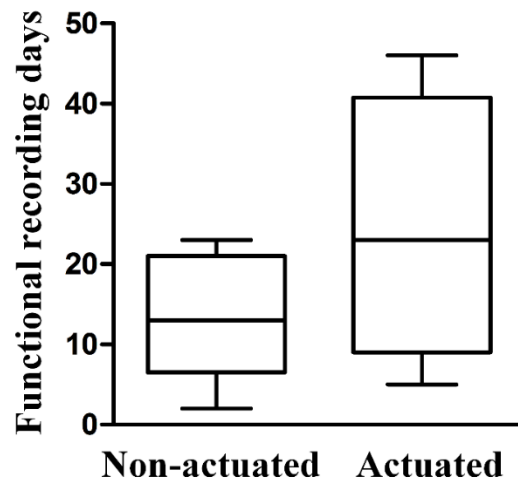
Figure 2.27: Functional recording day comparison between non-actuated and actuated. The functional recording day is longer for ultrasonically actuated insertion.
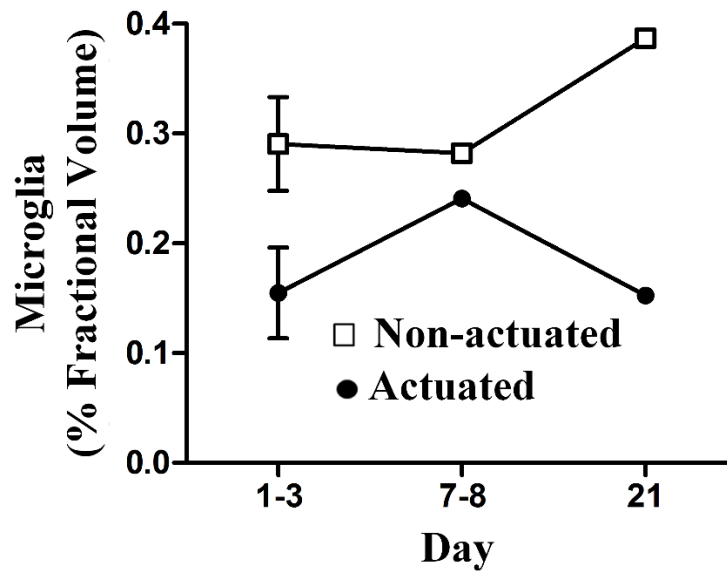
Figure 2.28: Percentage of fractional volume of microglia cell of the two-photon image. Ultrasonic actuated insertion has less microglia volume than non-actuated insertion over time.

In this chapter, we have demonstrated a systematic insertion study with different ultrasonic vibrating velocity. A damaged area consisting of edges with a high degree of randomness corresponding to a great number of jagged edges, during normal insertion compare to more compact and circular implantation site during ultrasonic insertion were observed. Insertion force and acute microglial response reduction were also demonstrated to provide essential qualities to characterize and improve neural probe reliability and importantly, extend the overall lifetime of the electrode. Based on these results, we hypothesized that ultrasonic actuation would likely lead to reduced chronic inflammation and better electrode performance. This hypothesis is supported by the chronic animal studies. Within ultrasonic assisted neural probe implantation, the functional recording in average is longer and the volume fraction of microglia cells over time is less than non-ultrasonic assisted implants.

The ultrasonic neural probe, comprise a neural probe, an ultrasonic transducer, and integrated strain gauge, can be implanted with less insertion force and tissue damage and further boost the neural interface performance. However, the whole structure is relatively large compared to other types of neural probes. During our chronic animal study, several mice suffer from catastrophic damage due to large head stage structure. Moreover, neural scientists prefer to use their own application specific neural probes for their own researches. In the following chapter, a method for implanting any other type of neural probe ultrasonically is developed.

CHAPTER 3

DETACHABLE ULTRASONIC ENABLED INSERTER FOR NEURAL PROBE

INSERTION USING BIODISSOLVABLE POLYETHYLENE GLYCOL (PEG)

3.1 *Introduction*

As introduced in Chapter 2.1, a reliable long-term stable neural interface is limited by the foreign body response of the brain against neural probes. As the immune reaction to probe insertion is caused by the presence of foreign material in the body, thinner and less stiff materials are being investigated to determine their effect on reducing tissue immune reactions [43]. Flexible polymer probes have been developed to reduce the stiffness mismatch between probe and tissue. One of the major challenges with very thin flexible materials is that the probe can buckle during insertion. Several insertion strategies had been developed for avoiding buckling, especially for the thin flexible neural probe, during insertions. Altering probe geometry, for example to fabricate probes with ribs or layers of other material for increasing the stiffness of part of compliance neural probe have been investigated. In addition, encapsulating polymer neural probe with biodegradable material or integrating microfluidic channel filled with biodegradable material for temporarily stiffening the probe have been developed [43], [75]–[77]. Smaller Young's modulus of biodegradable material than silicon results in larger dimensions to achieve the same stiffness for the coated flexible probes. Moreover, rounded tips due to probe coating leads to higher penetration force and qualitatively increasing the difficulty of insertion. Another approach is applying stiffeners during insertion and removing them after insertion. One of the methods is adhering the polymer probe onto a shuttle probe coated with self-assembling monolayers that customized the surface interaction with probes by using electrostatic force [78]. Another method is

using bio- dissolvable polymer to affix the probe to a silicon stiffener during insertion [79]. However, all these strategies mentioned above can still induce the initial insertion trauma.

In the previous chapter, we had shown that ultrasonic enabled neural probe insertion can decrease the initial insertion trauma with reduced insertion forces due to tissue stiffening and high-velocity micro-cutting. We demonstrated the microglia count reduction by a factor of 1.63, which indicates reduced immune response. However, the combined ultrasonic horn transducer and neural probe were too large to apply for chronic operation as described in Chapter 2.8. In this chapter, we demonstrated a detachable design using bio-dissolvable polymer to attach neural probe onto an ultrasonic actuator to achieve reduced insertion force and small neural probe. We selected polyethylene glycol (PEG) as bio-dissolvable adhesive material in this study. PEG has been used widely in implant applications such as neural probe and drug delivery [80], [81].

Ultrasonic drive can also effectively ″stiffen″ neural probe make with more flexible material against buckling. From the Euler's compression buckling formula, the maximum force, F_b, a beam can withstand before buckling is

$$F_b = \frac{\pi^2 E w t^3}{12 K l^2} \tag{3.1}$$

where $K = 2$ for a fixed-roller beam, w is probe width, t is probe thickness, l is probe length, and E is the Young's modulus of the probe material. Here we define the force margin, F_m, as difference between the buckling force, F_b, and the force, F_i, required to implant probe into tissue ($F_m = F_b - F_i$). If $F_m > 0$, then buckling will not occur, on the other hand, if $F_m \leq 0$, buckling will occur. To prevent the buckling event, larger force margin is preferred. From Equation (3.1), given the same probe geometry, the buckling

69

force is a function of the Young's modulus of the probe material. Material with less stiffness will suffer from less buckling force and hence small force margin. However, with ultrasonic actuated insertion, as described in Chapter 2, the insertion force can be reduced by 60 % at 30 V_{pp} driving voltage. We can predict that the buckling would occur less from the increased force margin and the tolerance for material stiffness can be lower with ultrasonic actuation insertion technique.

3.2 *Device design, fabrication, and characterization*

3.2.1 Structure design

A silicon catenoidal horn with 40 mm length and 10 mm to 1 mm end-to-tip width ratio is used as an inserter for the neural probes (Figure 3.1(a)). A neural probe attaching platform (1×3 mm^2) for different neural probe configurations is defined at the tip of the ultrasonic horn structure. A 25 μm thick trench is designed at the tip of horn for affixing different neural probes. Two 500 μm diameter holes are included in the trench to bind and release neural probes severing as adhesive leak cavities during bonding and enable very thin bond films of $4 - 6 \mu$m (Figure 3.1(b, c)). Four different neural probes model with various number of prongs and width of prongs are designed to mimic the commercial neural probes (Figure 3.1(d)). The dimension and effective contact area of each neural probes model are summarized in Table 3.1.

Table 3.1: Dimensions of three different probes design.

	Prong width	# of prongs	Prong contact area
Probe 1	200 μm	1	200 μm^2
Probe 2	150 μm	2	300 μm^2
Probe 3	100 μm	3	300 μm^2
Probe 4	200 μm	2	400 μm^2
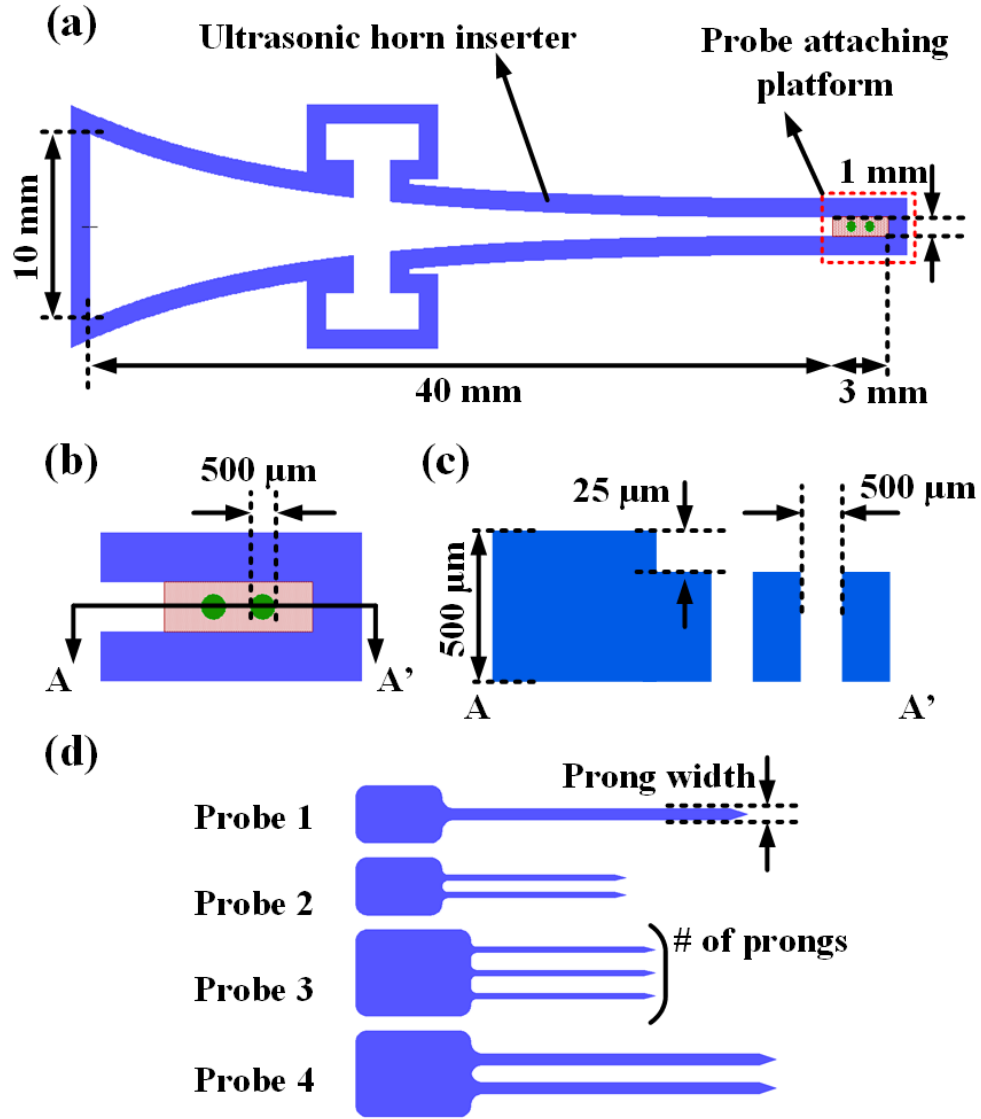
Figure 3.1: (a) CAD design for ultrasonic inserter and probe attaching platform. (b) Zoom in and (c) cross-section for the probe adhesive platform. (d) Four different type neural probe models are designed, with different prong width and number of prongs, to evaluate the performance of the ultrasonic inserter.
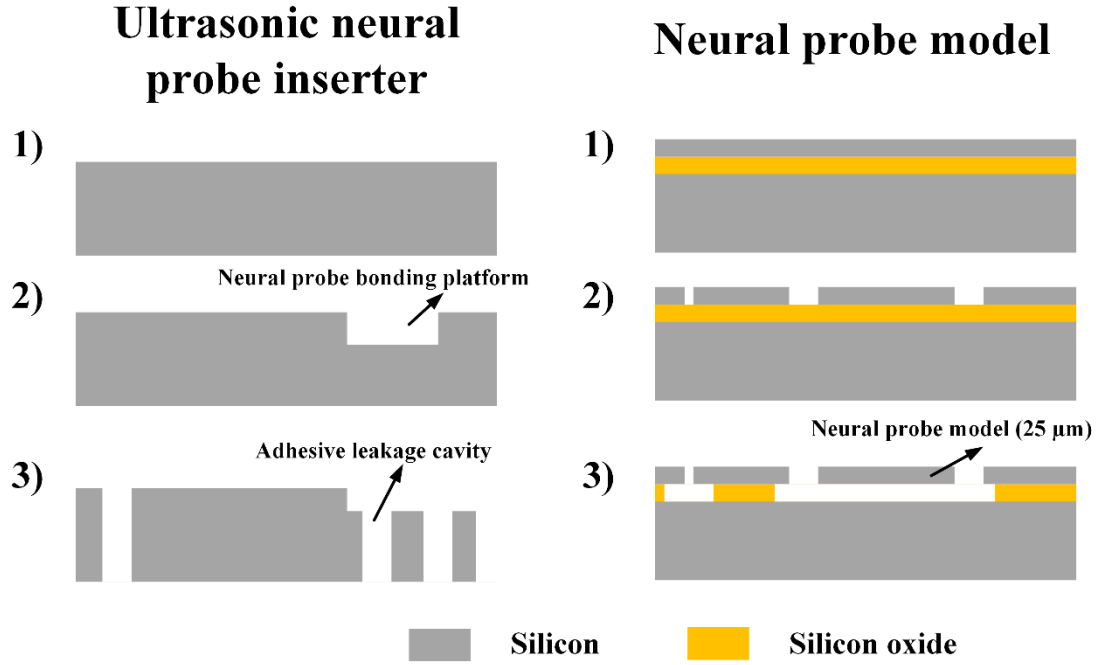
Figure 3.2: Process flow for (a) ultrasonic inserter and (b) neural probes model.

3.2.2 Fabrication process flow

The ultrasonic horn inserter is fabricated from a 500 μm thick silicon wafer using two-step DRIE dry etch utilizing the standard Bosh process. The etch process is similar to the one described in Chapter 2.4.2. During the first etching step, the thickness of neural probe attaching platform is defined. The secondary etching step defined the shape of ultrasonic horn and the adhesive cavity holes (Figure 3.2(a)). Neural probe model structures are fabricated from a 25 μm device thickness silicon-on-insulator (SOI) wafer. The probe geometries are defined by DRIE, and the structure is released by etching away the insulator layer with vapor hydrofluoric acid (HF) (Figure 3.2(b)).

3.2.3 Device assembly

Two PZT piezoelectric plates (4.5 $\times$ 13.3 $\times$ 0.5 mm^3) are affixed to the zero-displacement nodes of the half wavelength longitudinal mode onto the horn structure

for coupling and amplifying the motion from PZT to the tip. The entire structure is then mounted on a 3D-printed holder. Thin, 25 μm thick neural probes with multiple prongs geometries were bonded to the ultrasonic actuator using PEG (Figure 3.3(a)). The PEG (average molecular density of 10,000 g/cm^3) starts in solid platelets form and can be liquefied by heating up to around 70℃. After heating, a pipette is used to transfer the liquid PEG into the leak cavity holes. The liquid PEG flows into the holes forming a thin adhesive layer in the gap between the adhesive platform and the probe as a result of capillary forces. Once the temperature decreases to room temperature, the PEG is solidified and bonds the neural probe to the ultrasonic inserter.

3.2.4 Device characterization

Finite element simulation of neural probe affixed to the ultrasonic horn inserter indicate that the longitudinal resonance frequency is much lower than integrated neural probe design (Figure 3.3(b)), since the length of the ultrasonic horn structure is longer (40 mm). The resulting half-wavelength resonance frequency is approximately 105.2 kHz. The long length of ultrasonic transducer can also increase the strain amplification to achieve higher vibration velocity at the tip. Interferometry measurement (MSA-400, Polytec) is used to compare with the simulation results (Figure 3.4). The bode chart indicates the maximum longitudinal velocity is 473.7 mm/s with 10 V_{pp} driving voltage at 105.2 kHz. The velocity is higher than the integrated neural probe described in Chapter 2, as expected, since larger PZT plates can provide more energy coupling for more efficient actuation. Figure 3.5 shows the tip velocities versus longitudinal resonance frequency for different configurations of probe affixing on the ultrasonic horn inserter through PEG. The displacement of the ultrasonic horn resonator can be expressed as

(a) Anchor, Lead Zirconate Titanate Oxide plates for actuation, Holes for adhesive leak cavities faster release, Neural probe, Ultrasonic actuator, Adhesive platform

(b) Longitudinal mode @ 105.2 kHz
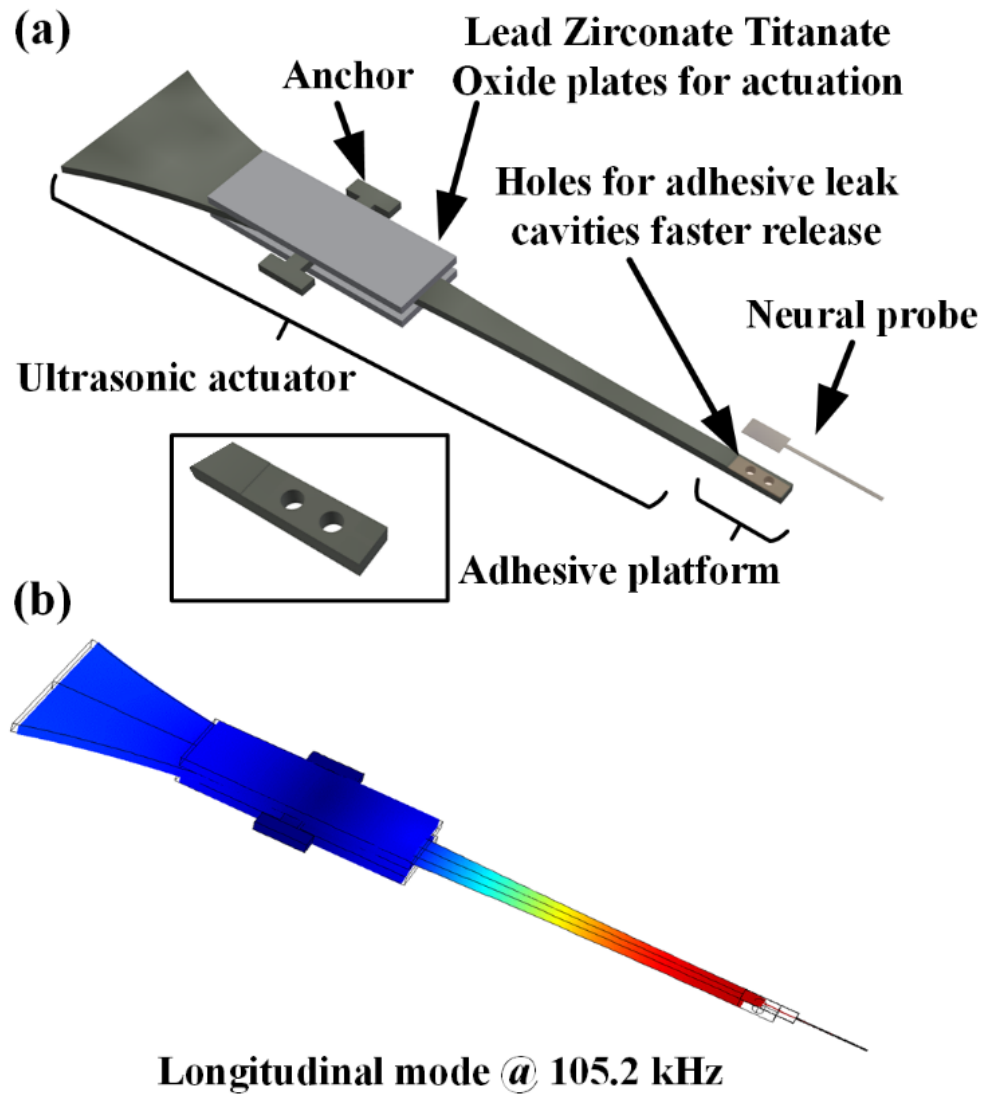
Figure 3.3: (a) The assembly diagram of the ultrasonic inserter. Two PZT plates are affixed to the displacement node of the ultrasonic actuator. A neural probe is attached to the adhesive platform with two 500 μm holes for adhesive leak cavity. (b) 3D COMSOL® simulation to evaluate the longitudinal resonance frequency of the ultrasonic inserter affixes with a single prong neural probe. The longitudinal resonance frequency is at 105.2 kHz.
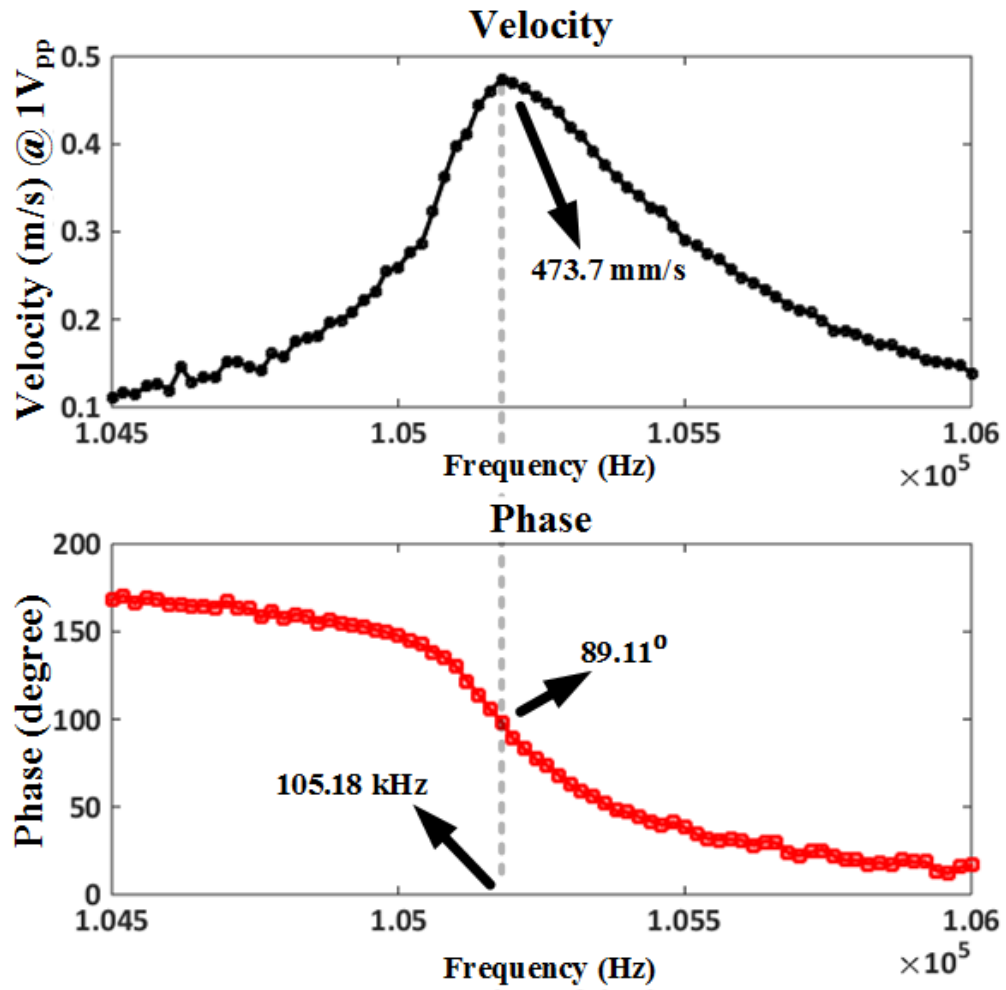
Figure 3.4: Velocity and phase versus frequency bode chart of the ultrasonic inserter affixes with a single prong neural probe model from the interferometric measurement. The maximum longitudinal velocity, 473.7 mm/s, is measured at 105.18 kHz with phase angle of 89.11°.
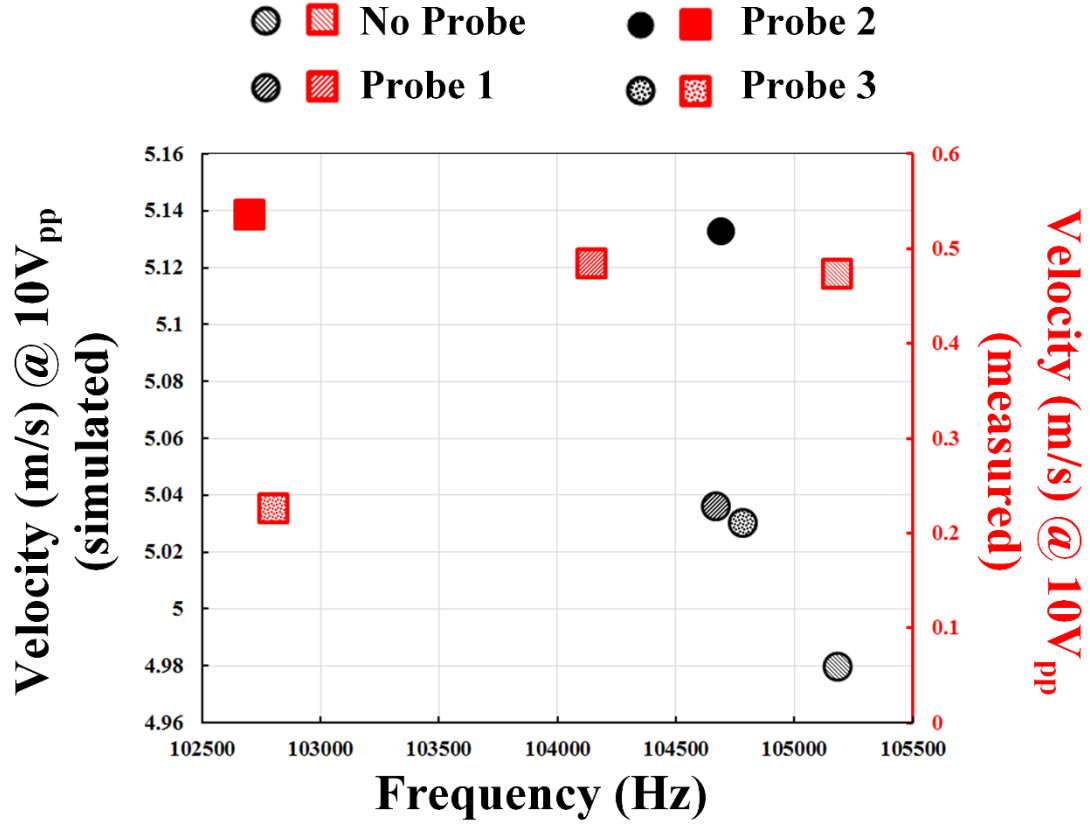
Figure 3.5: Summary of the finite element simulation and interferometric result with different neural probe models affix to the ultrasonic horn inserter. The measured velocity is one order magnitude lower than the simulation result. This is due to no loss mechanism is considered during the simulation. The shift of the resonance frequency come from the ultrasonic inserter assembly and neural probe model bonding procedure with PEG. The amount of the adhesive material is not well controlled. Note that, with no probe bonded to the ultrasonic inserter; the measured resonance frequency is very close the simulation results.

$$u = \frac{f/k}{\left(1 - \left(\frac{\omega}{\omega_0}\right)^2\right) + \frac{j\omega}{Q\omega_0}} \tag{3.2}$$

where ω_0 is the resonance frequency, ω is the operation frequency, f is the force, and k is the spring constant. The resonance frequency decreased due to increase in resonator length due to neural probe attachment. The measured velocity is less than the simulated results, due to the difference of quality factor in the ultrasonic horn resonator. In the finite element simulation, the quality factor is very high (~3000), however, the measured quality factor (~300) is lower results from air damping, anchor losses, and other loss mechanisms. Probe2 and probe3 configurations show slightly lower resonance frequency, this might be because from the amount of PEG affixing to the inserter is not well controlled. Nevertheless, the tip velocity is in the range of 226 mm/s to 1.59 m/s from 10 V_{pp} to 30 V_{pp} driving voltage, which is two orders of magnitude higher than the insertion stage velocity. This high velocity vibration at the tip is sufficient for cutting the tissue and reduce insertion force, as demonstrated in the previous chapter.

Ultrasonic waves are reflected at boundaries where there is a difference in acoustic impedance (Z_{act}) of the material on each side of the boundary. Z_{act} can be calculated by speed of sound times the density of the medium. The difference in Z_{act} is commonly referred to as the impedance mismatch. The greater the impedance mismatch, the greater the percentage of energy that will be reflected at the boundary between one medium and another. The fraction of the incident wave intensity that is reflected can be derived because particle velocity and local particle pressure must be continuous across the boundary. Here we want to estimate the efficiency of acoustic wave propagation from ultrasonic inserter through adhesive layer to neural probe model. We modeled the structure into three sections: 1) ultrasonic inserter (silicon), 2) adhesive platform
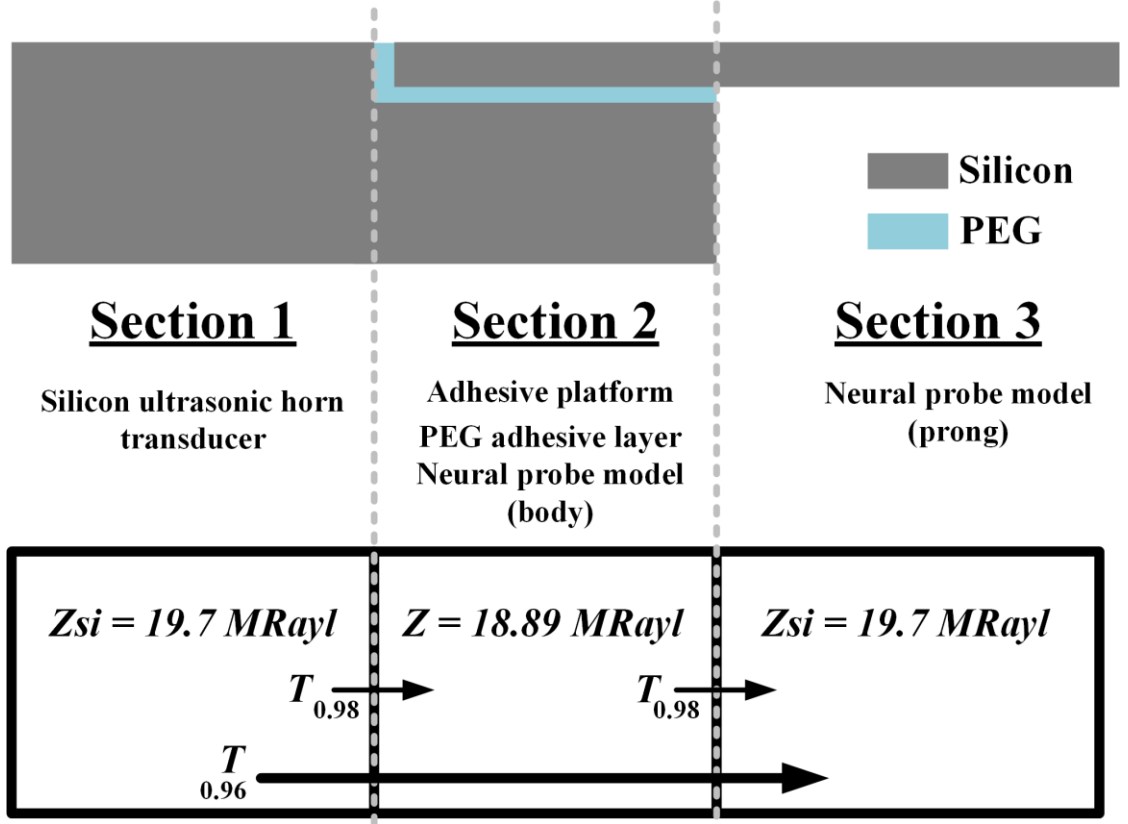
Figure 3.6: Acoustic energy transmission model. We model the structure into three sections: 1) ultrasonic inserter (silicon), 2) adhesive platform (silicon), adhesive layer (PEG) and neural probe body (silicon), and 3) neural probe prong (silicon).

(silicon), adhesive layer (PEG) and neural probe body (silicon), and 3) neural probe prong (silicon) (Figure 3.6). The first and last part is pure silicon, however, the second part consists of silicon and a thin layer of PEG. The effective density, ρ_{eff} can be estimated as

$$\rho_{eff} = \frac{\rho_{si} \cdot V_{si} + \rho_{PEG} \cdot V_{PEG}}{V_{si} + V_{PEG}} \tag{3.3}$$

where ρ_{si} is the density of the silicon (2329 kg/m³), ρ_{PEG} is the density of the PEG (1070 kg/m³), V_{si} is the volume of the silicon and V_{PEG} is the volume of PEG. The effective density of second part can be estimated as 2240 kg/m³ with the acoustic impedance of 18.89 MRayl. The transmission coefficient, T, is

$$T = 1 - \Gamma = 1 - \left(\frac{Z_{si} - Z_{in}}{Z_{si} + Z_{in}}\right) \tag{3.4}$$

where Γ is the reflection coefficient. The Z_{si} here is the acoustic impedance of the silicon (19.7 MRayl). The transmission coefficient from first part to the third part is 0.96. Most of the acoustic power can be transfer from the inserter to the neural probe model.

3.3 *Experimental results*

The experimental setup is shown in Figure 3.7. A tissue phantom (1% agarose gel) is placing on top of the load cell (GSO-10, Transducer Technique). The inserter with neural probe affix on top of it controlled by a motorized micromanipulator (MP285, Sutter Instrument). Insertion forces were measured at the rate of 60 Hz while the inserter is moving toward the neural tissue phantom with constant velocity (2 mm/s). A sample of the insertion force monitored by the load cell is shown in (Figure 3.8). A function generator (33521A, Keysight) and a piezo amplifier (EPA-104, Piezo Systems) are used to drive the inserter at resonance frequency with different voltage levels. A frequency tracking system is used to track frequency shift during each insertion procedure to ensure the ultrasonic transducer is driving under maximum efficiency. Once the insertion procedure is complete, a syringe with 0.9 % phosphate buffered saline is used to flush PEG away through holes at the back side of the platform. The average dissolving time for the PEG is around 5 minutes. The inserter is then retracted by the manipulator and leave the neural probe inside the tissue model (Figure 3.9).
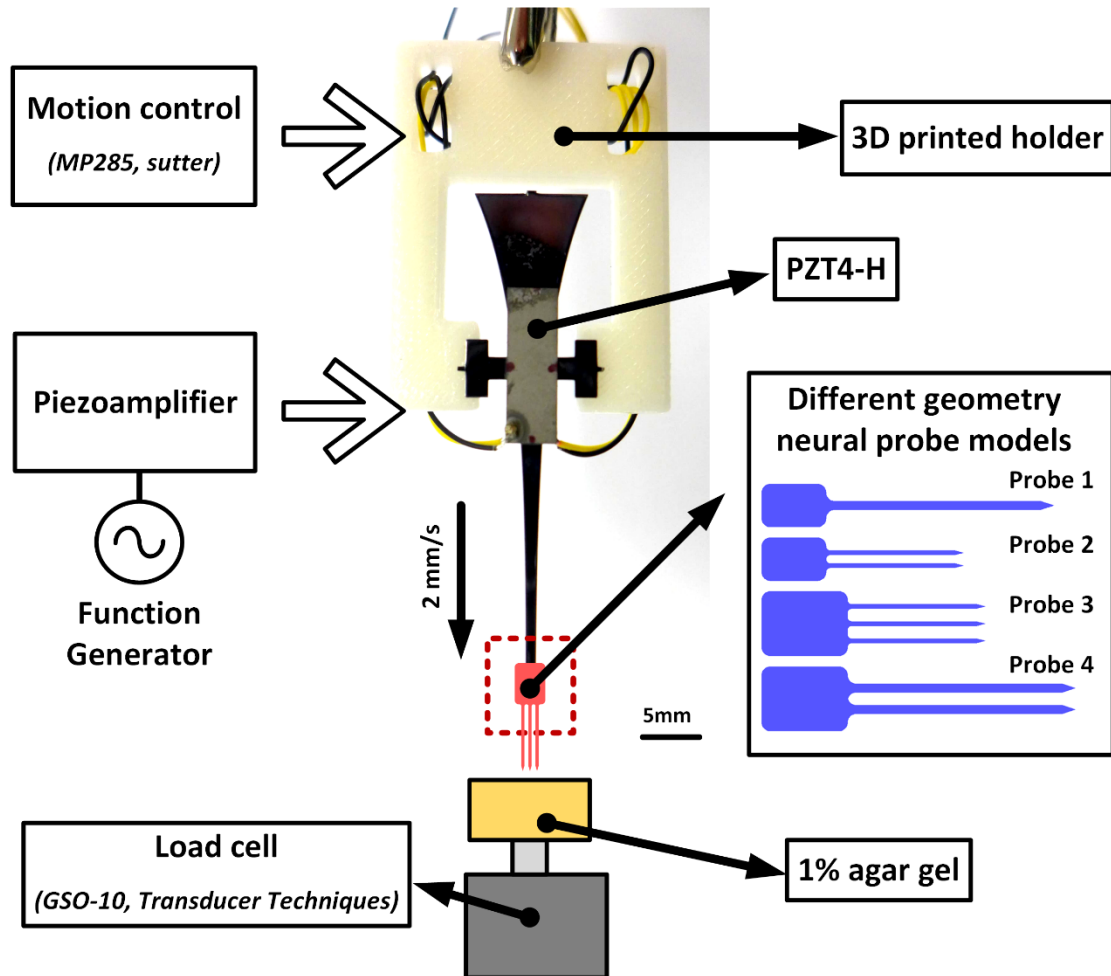
Figure 3.7: Diagram of the experiment setup. The motion of ultrasonic inserter is controlled by a high precision motorized micromanipulator. A function generator and a piezoamplifier are used to actuate the ultrasonic inserter with different voltage and frequency. Insertion forces are monitored by a load cell of different neural probe models.
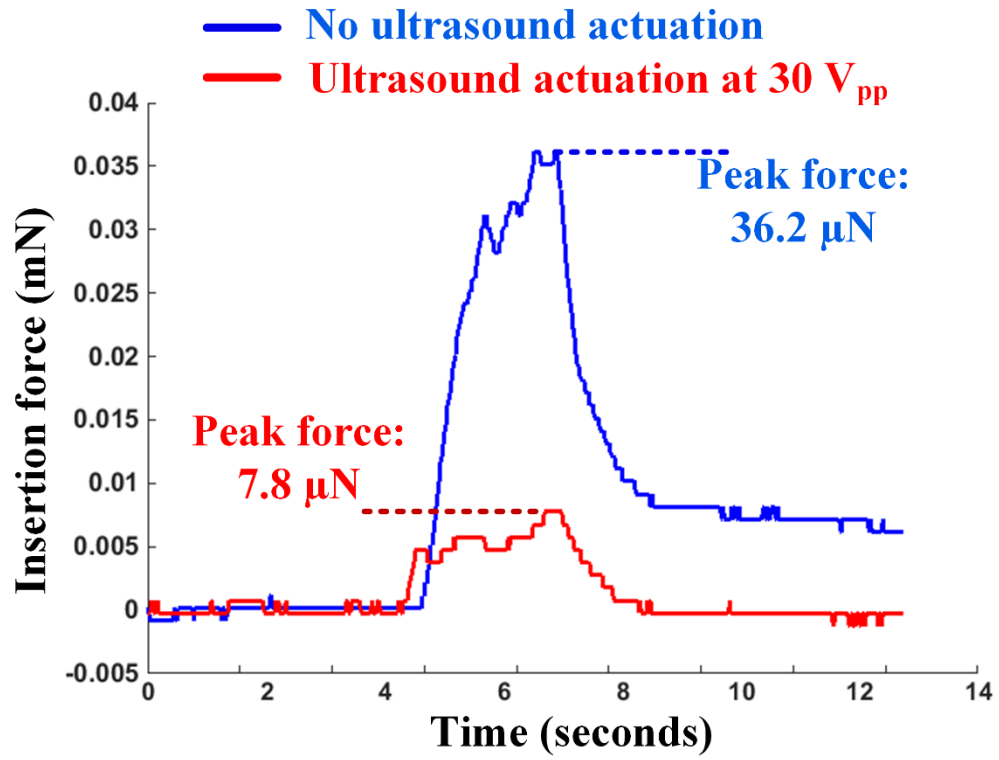
Figure 3.8: Insertion force profile measured by the load cell. With ultrasound actuation, the peak insertion force reduced 78.5% compare to non-ultrasound actuation.
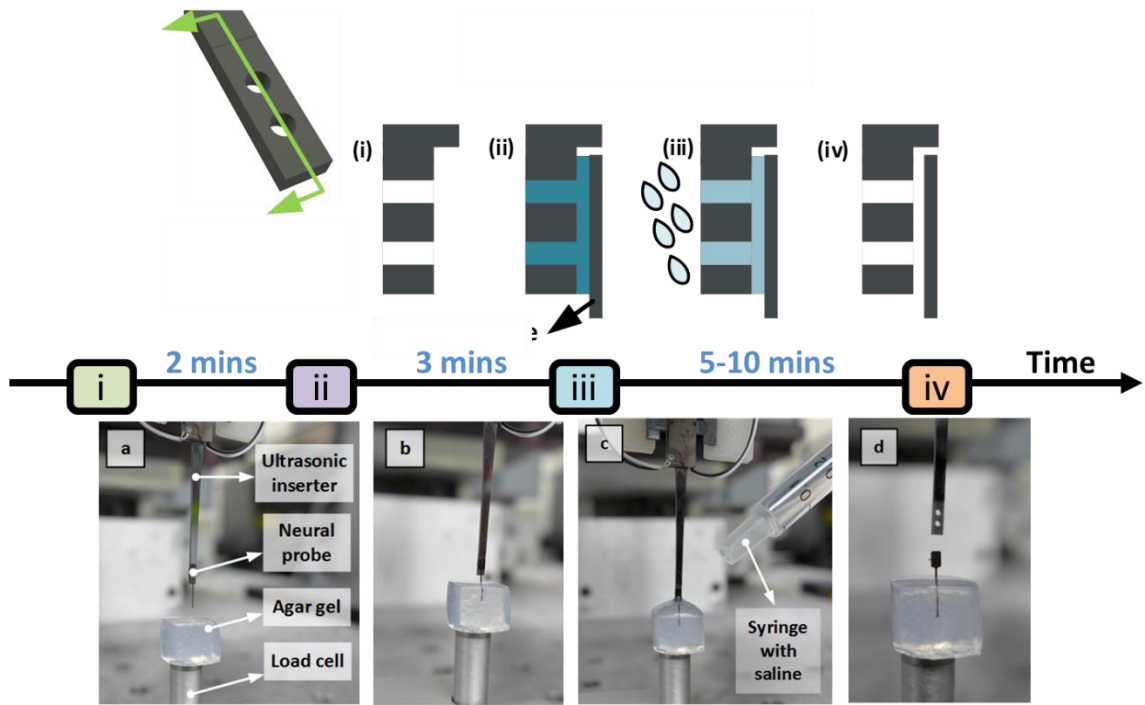
Figure 3.9: Cross section of the adhesive platform and assembly process. (a) Assembled neural probe with the ultrasonic inserter. (b) Insert the probe into tissue phantom. (c) Apply saline to the holes of the inserter to dissolve PEG. (d) Inserter retraction.

To further investigate the ultrasonic enabled neural probe insertion technique and the performance of detachable ultrasonic inserter design, insertion force for three different experiment configurations are performed: 1) detachable design versus non-detachable design, 2) longitudinal versus transverse mode actuation, and 3) different designs of detachable probes. Total ten runs with randomized driving voltage sequences were performed for each configuration.

3.3.1 Detached versus non-detached design

Detachable single prong neural probe model and the co-fabricated with ultrasonic inserter neural probe are evaluated. The ultrasonic transducers are both driving at half wavelength longitudinal resonance frequency. The insertion force profile between these two designs versus different actuation voltages is shown in (Figure 3.10). As we can see from the figure, the non-detachable design yields more force reduction (83.7%) than the detachable design (76.8%) at 30 V_{pp} driving voltage. This is due to the decrease in quality factor of the resonator cause from the PEG adhesive layer and non-perfect probe alignment. The force reduction from the detachable design is still significant.

3.3.2 Longitudinal mode versus transverse mode

In this section, two different actuation modes, longitudinal and transverse, under different driving voltages are investigated. Single prong non-detachable design is used for the experiment. The insertion forces profile between two different modes are shown in (Figure 3.11). Interestingly, for both longitudinal mode and transverse mode, the insertion force can be reduced. However, due to the low quality factor of the transverse mode, the reduction of force is limited. An amplitude modulation with the carrier frequency, f_c, of 122.95 kHz and modulating frequency, f_m, of 17.75 kHz driving scheme

is also applied to the ultrasonic inserter to evaluate the insertion force. The driving function can be express as

$$y(t) = \frac{AM}{2}[sin(2\pi(f_c + f_m)t + sin(2\pi(f_c - f_m)t]$$ (3.5)

where A is the amplitude of the carrier frequency, and M is the amplitude of the modulation frequency. Two frequency components for both longitudinal and transverse (105.2 kHz and 140.7 kHz) are co-exist in the output modulated waveform with amplitude of $AM/2$. The insertion force reduction for the amplitude modulation driving is in between the longitudinal and transverse mode actuation.

3.3.3 Different design of detachable probes

Four different configurations of the neural probe models with different prong contact area were evaluated. The insertion force under different ultrasonic driving voltages measurement results are summarized in (Figure 3.12). The insertion force is proportional to the contact area of the neural probes. The probes with the larger contact area due to more prongs presented a different resonance frequency and coupling of energy but were able to get similar force reductions. Nevertheless, the insertion force can still be reduced more than 70% for all four different neural probe models, while driving at 30 V$_{pp}$ longitudinal mode (Figure 3.13). Note that all experiments were performed by using the same inserter, to detach and reattach probes indicating the reusability of the inserter.

3.4 *Conclusion and future directions*

In this chapter, we presented a silicon ultrasonic neural probe insertion method. An ultrasonic inserter is designed to affix different types of neural probes using PEG
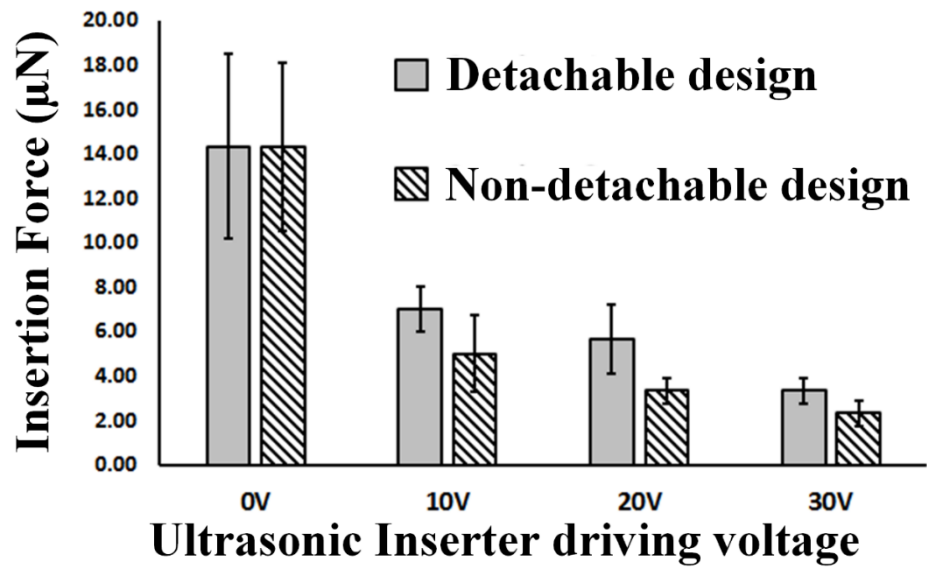
Figure 3.10: Insertion force of detached versus non-detached design with different inserter driving voltages at longitudinal mode resonance frequency.
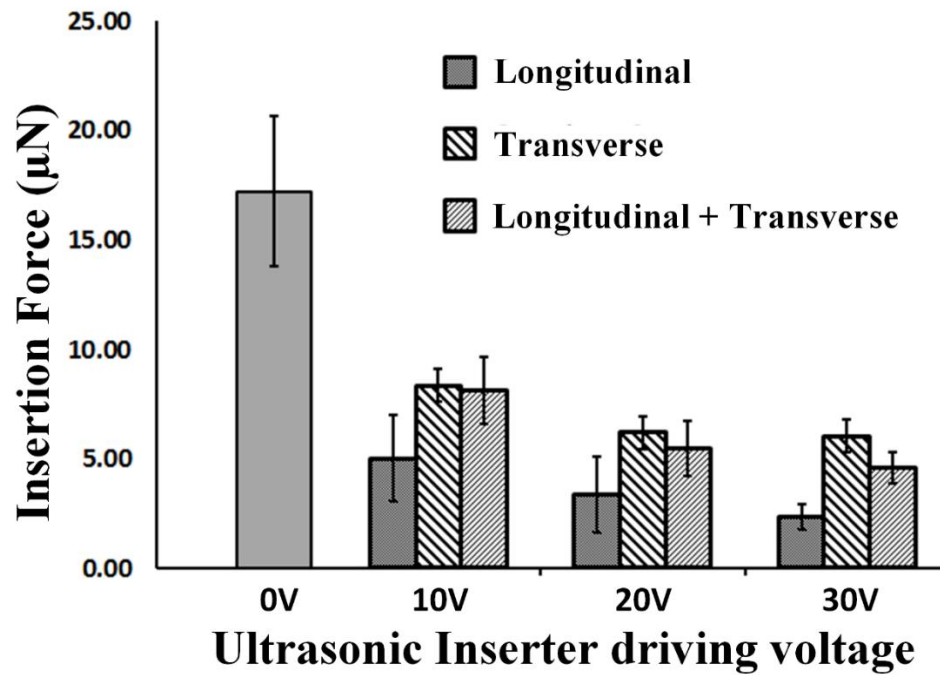
Figure 3.11: Insertion force measurement of different driving modes with different inserter driving voltages.

85
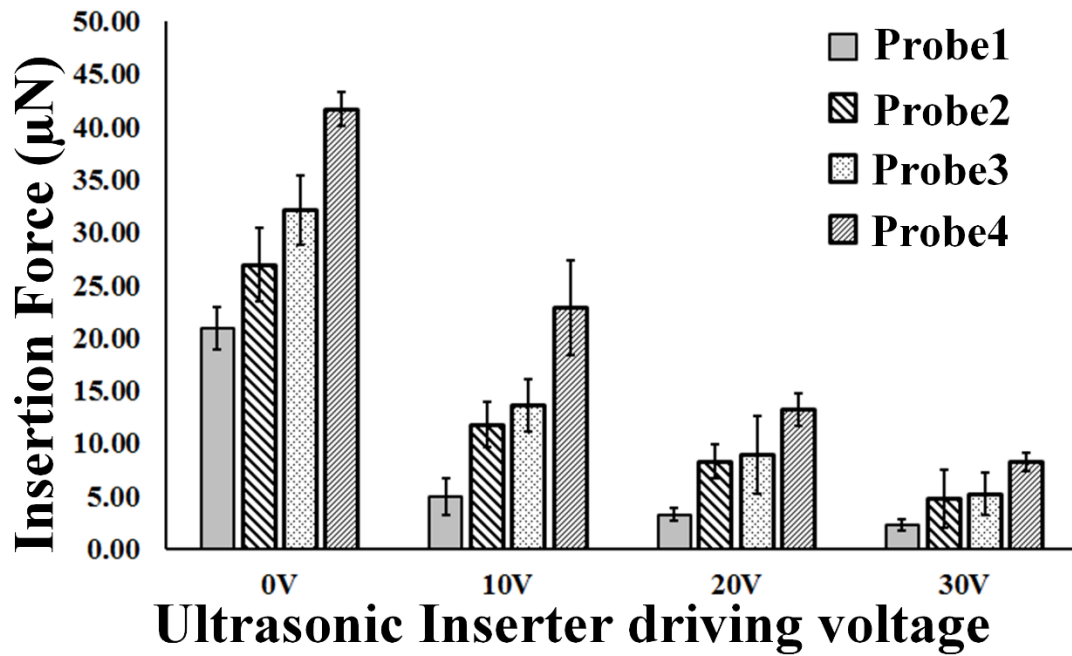
Figure 3.12: Summary of insertion force of different neural probe models affix to ultrasonic inserter under different actuating voltage at longitudinal mode resonance frequency. Within the increase of the contact area, from Probe1 to Probe4, the required peak insertion force is increased.
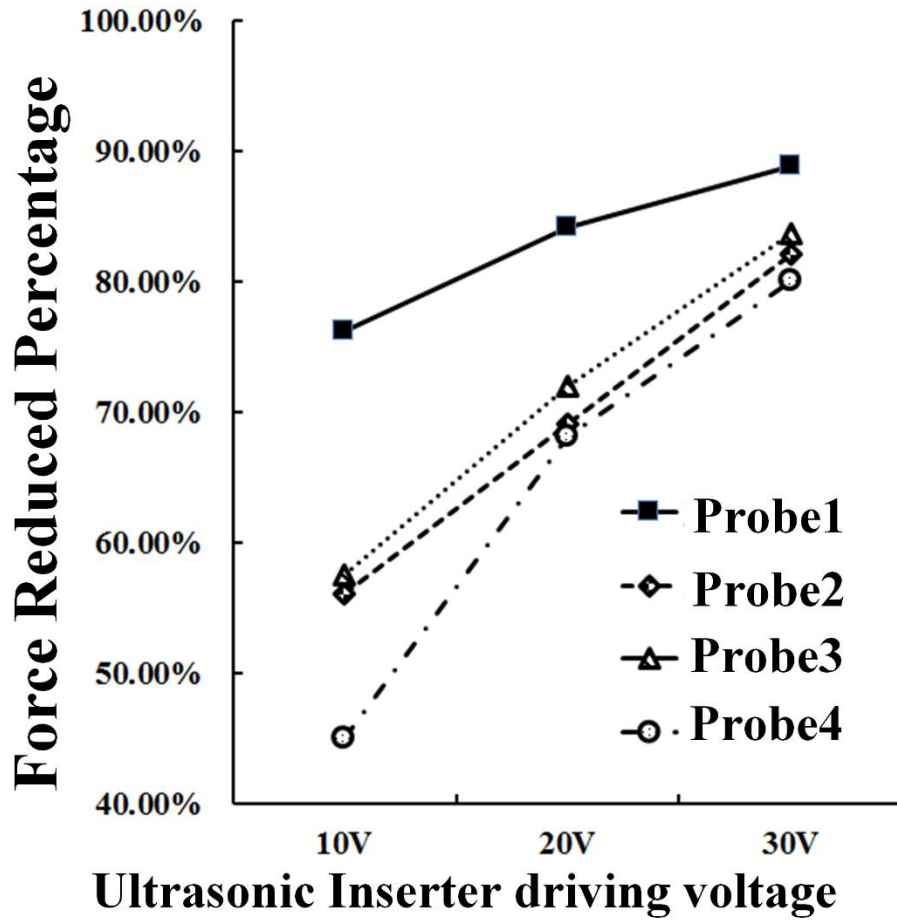
Figure 3.13: Force reduction percentage of different probe geometries with different inserter driving voltages. The insertion force reduction percentage is all above 75% for four different neural probes.

polymer as an adhesive and a bio-dissolvable material. The method can reversibly bond neural probes onto the ultrasonic inserter, taking advantage of the ultrasonic micro cutting induced reduced damage, and debonded after the implantation procedure by aqueous dissolution. We have demonstrated the insertion force reduction over 70% with four different neural probe models with 30 V_{pp} driving voltage at longitudinal mode actuation (105.2 kHz). This method can help inserting neural probes made in any new

technology and address a critical problem in increasing lifetime of neural probe recording sites.

In the future, neural probe bonding procedure needs to be improved with better adhesive quantity control and probe alignment technique to reduce the variation between each experiment. Moreover, similar to the previous chapter, strain gauges can be integrated with the ultrasonic inserter for monitoring the condition of the ultrasonic vibration amplitude. Last but not least, *in vivo* experiments with the ultrasonic inserter bonded to commercial available neural probes need to perform for further investigating the chronic reliability.

CHAPTER 4

A SILICON ELECTRO-MECHANO TISSUE ASSAY SURGICAL TWEEZER

4.1 *Introduction*

Surgeons make decisions on the use of different surgical tools providing a spectrum of contact forces to cut and manipulate tissue. These decisions are mostly made without quantitative data about the mechanical integrity and mechanical properties of the tissue. Different physical modalities, for example, tissue electrical impedance, tissue Young's modulus, and tissue insertion force, can be used to measure tissue and material electrical and mechanical properties.

Tissue electrical impedance (Bioimpedance): Bioimpedance describes the passive electrical properties of biological materials and serves as an indirect transducing mechanism for physiological events, often in cases where no specific transducer for that event exist. Impedance, Z, is a general term related to the ability to oppose ac current flow, expressed as the ratio between an AC sinusoidal voltage and an AC sinusoidal current in an electric circuit. Impedance is a complex quantity because a biomaterial, in addition to opposing current flow, phases-shifts the voltage with respect to the current in the time-domain. Admittance, Y, is the inverse of impedance ($Y=1/Z$). The common term for impedance and admittance is immittance. Tissue is composed of cells with poorly conducting thin cell membranes; therefore, tissue has capacitive properties: the higher the frequency, the lower the impedance. Bioimpedance is frequency-dependent, and impedance spectroscopy, hence, gives important information about tissue and membrane structures as well as intra and extracellular liquid distributions. Recent studies [82]–[84] cancerous and normal tissue was investigated using a tetrapolar electrode. Electrical admittivity (conductivity and permittivity) was recorded at 31

discrete frequencies of 0.1 to 100 kHz from each of *ex-vivo* human prostates. Discriminatory power of admittivity properties of cancer and other tissues was proven by receiver operating characteristic (ROC) analysis for *in-vitro* tissue studies. Conductivity is reported significant less in the malignant (140 ± 32 mS/m) than benign tissue (150 ± 31 mS/m). Another study [85] also investigated cancerous and benign tissue using transrectal ultrasound guided sextant needle biopsy at the frequency range from 100 kHz to 4 MHz *ex-vivo*. Electrical impedance at 100 kHz is reported significantly higher in cancerous tissue (1312 ± 265 Ω) than benign tissue (1123 ± 245 Ω). Hence, the measurement of electrical impedance could provide a confidence level high enough for tissue characterization. These studies, however, were on *in-vitro* tissue, which can be different from *in-vivo* tissue. Experiments could not be done on *in-vivo* experiments because the probe and electronics are not small enough for *in-vivo* measurements.

Tissue Young's Modulus (Elastic properties): Young's modulus describes the ability of an elastic material to resist deformation to an applied stress and is defined as the ratio of applied stress (σ) to resultant strain (ϵ) ($E = \sigma/\epsilon$). Stress is the force divided by the area over which it is applied. Strain is a dimensionless quantity defined by the stress-induced change in length of a material divided by its unstressed length ($\Delta L/L$). Soft tissues are not perfectly elastic materials or homogeneous, and they typically display both viscous and elastic properties that are dependent on time and typically display nonlinear stress-strain function. For perfectly elastic materials a single Young's modulus value defines the response of material to deformation. For soft biological tissues, the resistance to deformation typically increases as the applied stress increases. Therefore, Young's modulus is not constant and depends on the specific applied stress, which is particularly important as tissues *in-vivo* typically exist in a pre-stressed state [86]. However, soft tissues are typically assumed to behave as elastic solids if a

significant linear regime of stress-to-strain exist in the limit of small strain response to applied stress [87]. In [88], viscoelastic properties were used to characterize the mechanical stress relaxation data measured from human prostate tissue samples. The measurement results show that the viscoelastic properties of cancerous prostate tissue are greater than normal tissue by a factor of approximately 2.4. Moreover, in [89] the measurement of prostate viscoelastic properties indicates the normal tissue Young's modulus is 15.9 ± 5.9 kPa, while the cancerous tissue is 40.4 ± 15.7 kPa. Studies have also shown that resonance properties of piezoelectrically driven actuators in tissue have significantly different resonance frequencies, and loss-factors [27]. Moreover, the viscosity of cancer tissue was found higher than normal tissue [90].

Tissue Insertion Force: In [91] a needle with a centimeter-scale force gauge was used to characterize insertion force into prostate tissue. It was intended to be used in robotic brachytherapy where a needle is inserted into the tissue, force-torque data collected and results show that cancer tissue is harder, prostate density and prostate-specific antigen (PSA) have significant effects on mean forces. Moreover, in [6], the penetration force in tissue can be used to image fine vessels and measure morphology of tissue at 25-50 µm resolution. Hence, measurement of insertion force could differentiate healthy from the unhealthy tissue.

Many previous works have demonstrated individual modalities for tissue characterization. A summary of three different modalities for tissue characterization is shown in Figure 4.1. Given that different approaches can be used to characterize tissue, it would be beneficial to the surgeon to have a surgical tool that can measure the various properties during surgery with minimal effect on the surgery time or procedure. With multimodal tissue characterization, the surgeons can narrow down the patient-specific criteria. In particular, during intestinal anastomoses (the joining of two intestinal loops after removal of a diseased intestinal segment) are commonly performed with stapling
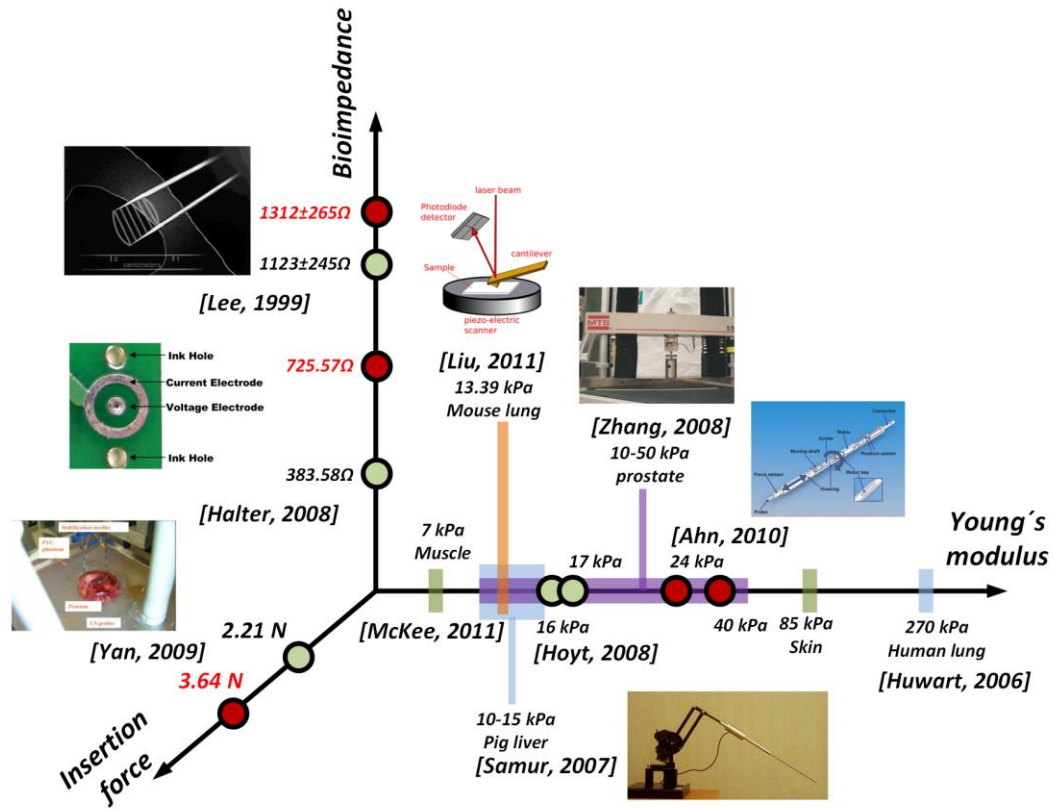
Figure 4.1: Summary of different modalities for the tissue characterization, including bioimpedance, Young's modulus, and insertion force. Cancerous tissue (red dot) tends to have a higher impedance, Young's modulus, and insertion force than benign tissue (green dot).

devices. To compensate for the difference in intestinal wall thickness due to individual patient variability and different pathologic conditions, stapling devices come loaded with staples of different height. The most common staples, when fired, have a profile height that varies between 1.0 mm and 2.0mm. Despite the high reliability of stapling devices, intestinal anastomosis fails to heal appropriately in about 1-7% of cases [92]. The failure is called a "dehiscence." Dehiscences are catastrophic events for patients regarding additional morbidity, the need for additional interventions, increased length of hospital stay and recovery, occasional mortality, and overall increased the cost of the healthcare system [93]. It is calculated that dehiscences add an average of $30,000 to 50,000 to the expense of a simple bowel resection. Intestinal resections and anastomoses are common procedures. With close to 500,000 intestinal resections each year for cancer, acute and chronic inflammatory bowel disease, hemorrhage, obstruction and congenital malformations, the cost of caring for 1-7% of patients suffering a dehiscence amounts to millions of dollars. There are many reasons for the non-healing of intestinal anastomosis. Two of them are 1) the mismatch between the size of the staplers and the thickness of the intestine, and 2) a decrease in compliance and pliability of the intestinal wall. In the first case, the intestinal wall may be too thick even for the largest staple; in the second case, the intestinal wall may be too rigid to accept a staple without being fractured. At present, most gastrointestinal surgeries do not use any tissue monitoring devices. The surgeons' expertise drives the choice of anastomotic technique and, if a stapling device is chosen, the size of the staples to be used. A device which could accurately measure both intestinal wall thickness and compliance could help surgeons to choose the appropriate size staples or to identify situations where alternative methods to perform an anastomosis should be used, for example, hand sewn anastomosis rather than stapled anastomosis.

(a)

Readouts:
Insertion force
Stiffness
Electrical impedance

Tissue

**Electro-mechano tissue
assay tweezer**
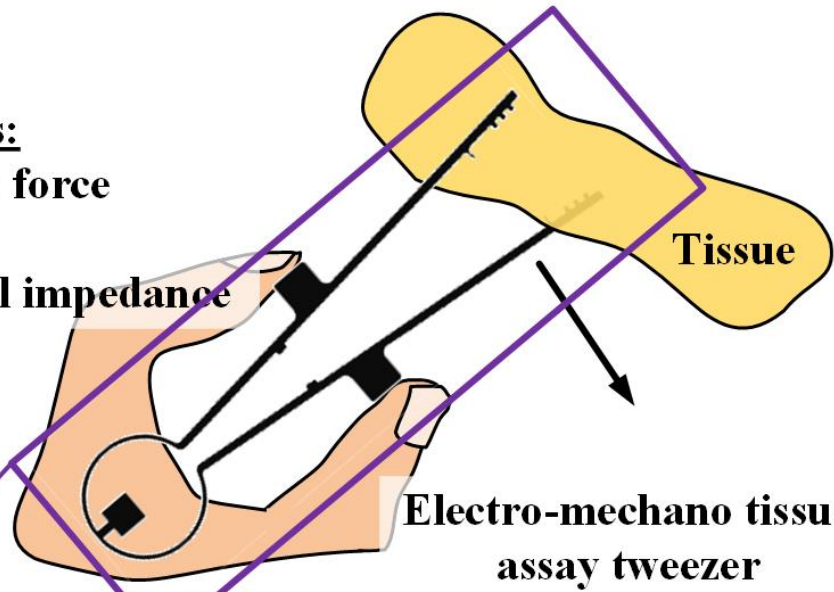
(b)

Hinge {

Stopper {

Arm {

Leg {

(c)

**Polysilicon staring
gauges for displacement**

(d)

**Polysilicon staring gauges
for insertion force**

**Platinum electrode for
impedance measurement**

**Polysilicon staring gauges
for indentation force**

Figure 4.2: **(a) Schematic of the silicon tissue multimodal assay tweezer. Three different tissue properties (insertion force, Young's modulus, and electrical impedance) can be measured simultaneously. (b) The tweezer structure consists four three parts: 1) hinge, 2) arm and leg, and 3) microprobes. (c) Polysilicon piezoresistor strain gauge are integrated into the hinge structure as a displacement sensor. During the tweezing motion, the building stress along with the circular hinge can be used as an indicator for indentation distance. (d) Two different geometry of the microprobes for indentation force (round probe) and insertion force (sharp probe) measurement. The force is measured by polysilicon piezoresistors configured in Wheatstone bridge. Two platinum electrodes are integrated on the sharp probe for tissue electrical impedance measurement after insertion.**

In this chapter, we presented a surgical tool in tweezer structure to provide a platform for the clinical use during surgery (Figure 4.2(a)). Instead of attaching sensors on to an existing tweezer [94] and probe-like tissue stiffness tactile sensors, an all-silicon structure offers several advantages. These include: (1) repeatability between tweezers (Figure 4.2), a wide variety of sensors, and sensor matching, (2) Highly accurate placement of sensors across from one handle of the tweezer to the opposing side, and (3) the potential integration of complementary metal-oxide semiconductor (CMOS) into the tweezer for a highly integrated system. The lithographic precision of a few microns over a 10-cm tweezer provides 1-10 part-per-million repeatability of spring constants and force sensitivity. The all-silicon structure also enables extensive embedded sensor integration, potentially alongside CMOS circuits, for a highly functional surgical tweezer. Multimodal measurements can also help tease out differences in seemingly similar tissue samples without time-consuming tissue assays.

4.2 *Device design, fabrication, and characterization*

4.2.1 Structure design

The silicon tissue multimodal assay tweezer was designed in three different parts (Figure 4.2(b)), including 1) hinge, 2) leg and arm, and 3) microprobes.

Hinge design: The silicon tweezing radius-of-curvature is designed for taking less than the maximum silicon fracture stress to avoid in-use fracture. However, different fracture stresses of silicon have been reported range from 0.6 to 6.9 GPa [95]–[97]. The silicon tweezer structure with different radius and width of circular hinge design was trial and error along with finite element simulation. A simulated stress versus hinge radius and width is shown in (Figure 4.3(a)). The hinge with a radius of 7.5 mm, width of 400 μm and maximum von Mises stress of 286 MPa is chosen to have the reliable and repeatable performance (Figure 4.3(b)).
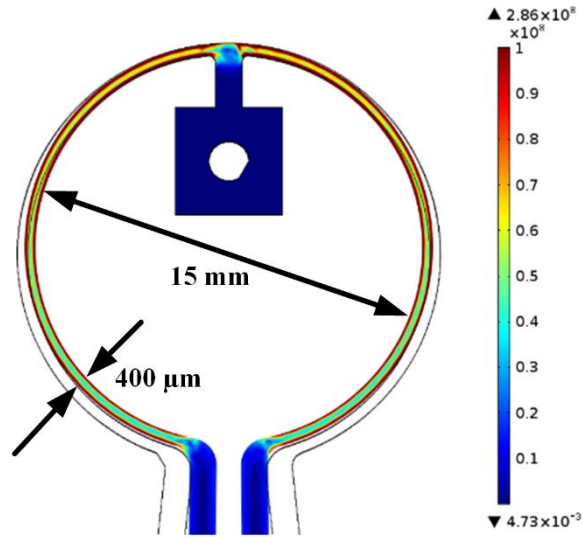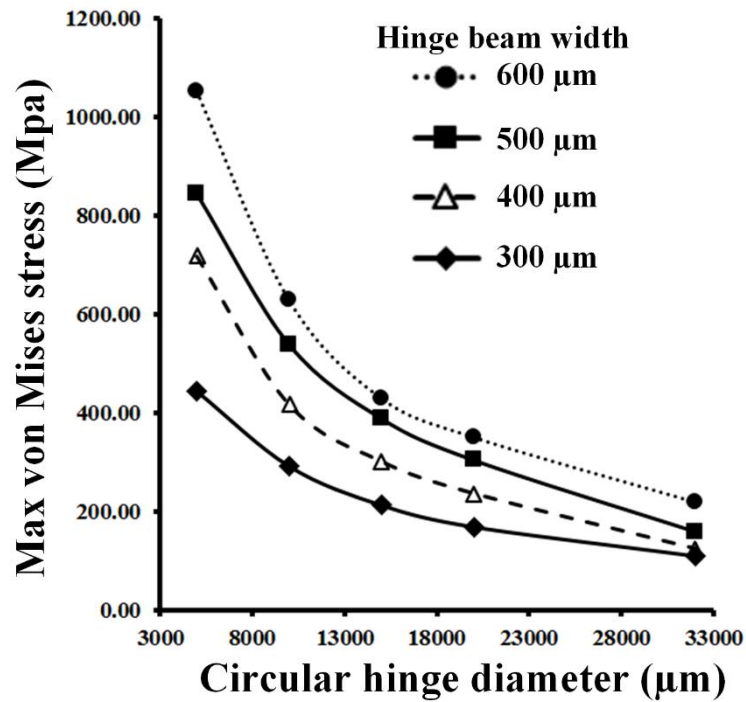
Figure 4.3 Finite element simulation for *von Mises* stress on the hinge structure during tweezing motion. (a) The maximum stress for hinge structure with a diameter of 15 mm and width of 400 *μ*m is 286 MPa. (b) Summary of maximum stresses of different diameters of circular hinge structure with different width.

The spring constant for the circular hinge can be calculated by using Castigliano's Theorem,

$$\delta = \frac{\partial U}{\partial F} \tag{4.1}$$

where δ is the displacement of the point of application of force F, and U is strain energy. Due the symmetry, the hinge structure can be simplified as the beam shown in Figure 4.4(a) with the force applied on the arm structure. Since the ratio of radius-of-curvature, R, and thickens of the hinge beam, h, is larger than 10 ($R/h > 10$). Only the moment is considered. The moment from AB (Figure 4.4(b)) is

$$M_{AB} = Fx \tag{4.2}$$

and the moment from BC (Figure 4.4(c)) is

$$M_{BC} = FL + FR(1 - cos\theta) \tag{4.3}$$

The total strain energy from the moment can be written as

$$U = U_{AB} + U_{BC} = \int_0^L \frac{M_{AB}^2}{2EI_{arm}} dx + \int_0^{0.94\pi} \frac{M_{BC}^2}{2EI_{hinge}} R d\theta \tag{4.4}$$

From Equation (4.2)-(4.4), we can obtain the displacement in Equation (4.1) as

$$\delta = \int_0^L Fx \frac{x}{EI_{arm}} dx + \int_0^{0.94\pi} (FL + FR(1 - cos\theta)) \frac{(L + R(1 - cos\theta))}{2EI_{hinge}} R d\theta \tag{4.5}$$

98
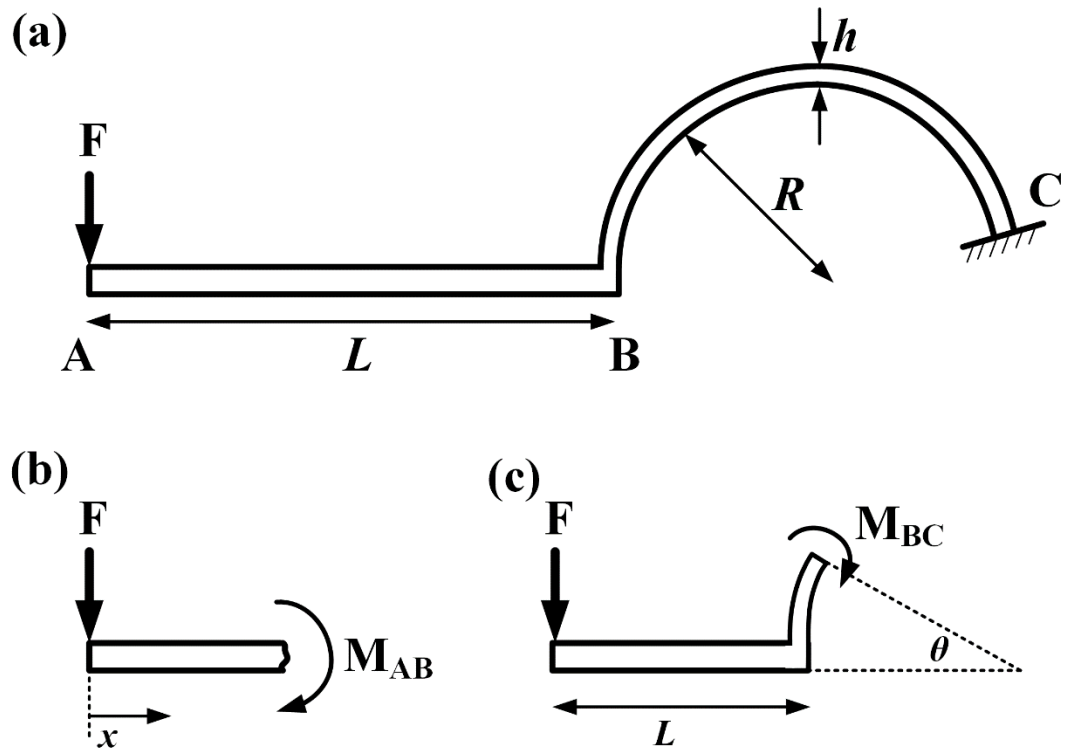
Figure 4.4: (a) Simplified half circular hinge structure. The force is applied at distance *L* away from the hinge (the location of the tweezer arm). The ratio of radius-of-curvature and thickness of the hinge is 18.75. **(b)** The moment from A to B. **(c)** The moment from B to C.
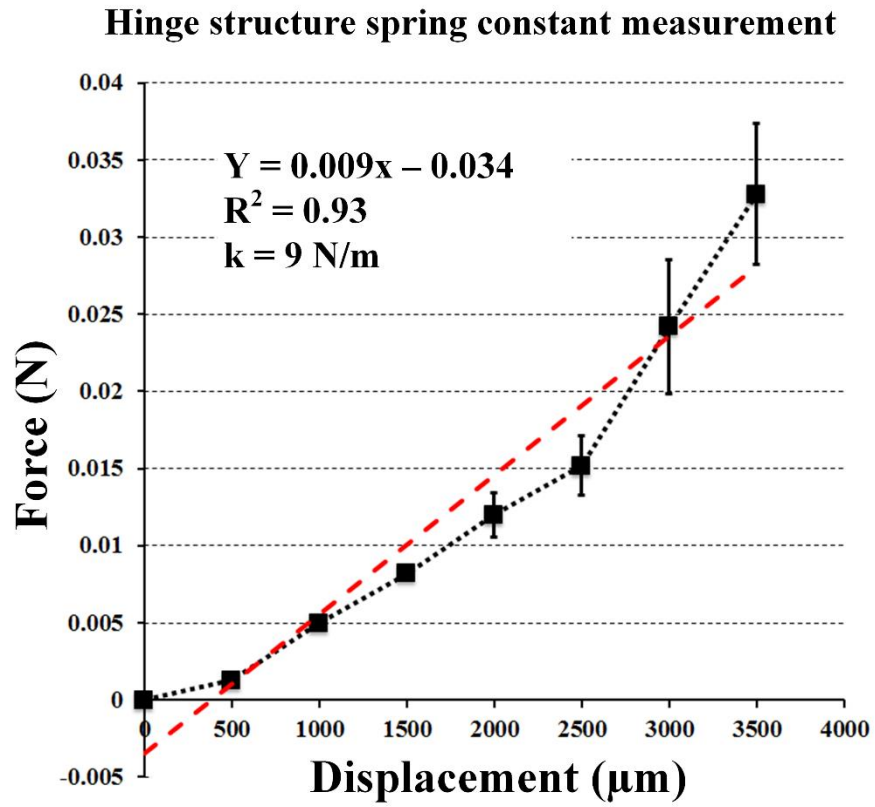
Figure 4.5: Spring constant measurement results and curve fit. The spring constant for the radius of 8 mm and width of 400 μm is 9 N/m. The measured results is closely matched to the model estimated value (Equation 4.3), 9.33 N/m.

The final expression for the displacement is

$$\delta = \frac{F}{EI_{arm}}\left(\frac{L^3}{3}\right) + \frac{F}{EI_{hinge}}(1.48L^2R + 5.52LR^2 + 1.95R^3) \tag{4.6}$$

The spring constant can be calculated from F/δ. For the tweezer structure with hinge radius of 16 mm and with of 400 μm, and arm with length of 21 mm and thickness of 1 mm. The spring constant is calculated as 9.33 N/m. The value is very close to the measurement results, 9 N/m (Figure 4.5). This is sufficient for human tweezing motion compared to the regular stainless steel tweezer spring constant is in the range of 30-40 N/m.

Four polysilicon piezoresistors in Wheatstone configuration is integrated along with the hinge structure as displacement sensor (Figure 4.2(c)). By monitoring the stress along the hinge structure during the tweezing motion, the displacement of the tweezer can be measured. A 4 mm by 4 mm square structure with 1 mm width connection structure is designed as an electrical interface for the displacement sensors and wire bonding area. A hole with 750 μm radius on the square platform is designed for alignment during assembly.

Legs and arms: The leg with a width of 1 mm carried interconnects from the microprobes to the tweezing-arm for the electronic interface. At the same time, a set of stopper structure was designed to confine the motion of the tweezer avoiding crashing of the probe tips on opposing sides (Figure 4.2(b)).

Microprobe design: Two types of microprobe geometries with a thickness of 200 µm are designed to measure indentation force (rounded probe) and insertion force (sharp probe) (Figure 4.2(d)). Polysilicon strain gauges were integrated at the junction of the leg and the microprobe to measure the longitudinal and flexural strain due to tissue

contact. The sharp probe is designed to penetrate tissue; it includes strain gauges in half Wheatstone bridge configuration for the insertion force monitoring. On the other hand, the rounded probe is designed not to penetrate but to compress tissue. It includes a set of strain gauge in single balanced Wheatstone bridge configuration for indentation force measurement. Four platinum electrodes were also co-fabricated into the sharp probe to measure electrical impedance. Total of six indentation probe and two insertion probe were integrated at the end of each tweezer legs. Simultaneous measurements of tissue stiffness, insertion force and electrical impedance at different points provide fast measurement in time critical surgeries.

4.2.2 Fabrication process flow

The fabrication process is similar to the ultrasonic neural probe as described in Chapter 2.4.2. Briefly, polysilicon strain gauge resistors are realized by LPCVD polysilicon film implanted with boron at a dose of 2×10^{15} ions/cm^2 at 100 keV. The resistors are electrically contacted with aluminum alloy (Al + 1% silicon) metal lines. Insulating PECVD silicon nitride is deposited, followed by platinum evaporation to define electrode sites. Two step, front-side and back-side, DRIE etching is used to release the device from the wafer. The front side etching defines the tweezer structure and thickness of microprobes and the back-side etching release the entire structure. A polymer coating, Proteck SR-25 is spun on the front-side to protect features during the back-side etching process.

4.2.3 Device assembly

The fabricated silicon tweezer device is placed on a 3D printed plastic package. The silicon/plastic composite structure increased the out-of-plane rigidity. The Young's modulus of the plastic material is 3091.7 MPa, and provides the 18 times more flexural

rigidity as silicon at a thickness of 5 mm. To further enhance the out-of-plane rigidity, a z-direction motion confined structure is also designed in the 3D printed package to further limit the z-direction motion (Figure 4.6(a)). The plastic package can also provide the robustness during tweezer operation as human hands will find it easier to manipulate a plastic surface as opposed directly contacting the silicon surface. A PCB affixed on the on the top of 3D printed package hinge area interfacing the displacement sensors and two flexible cables is used to interfacing sensors from the microprobe. An assembled tweezer is shown in Figure 4.6(b).

4.3 *Experimental Results*

The experimental setup is shown in Figure 4.7(a). The silicon tweezer is attached on a 3D printed holder with the custom printed circuit board (PCB) and flexible cable. Tissue sample is placed between two tweezer legs. One side of the arm is fixed while the other size of the arm is moved by a high precision micromanipulator (MP285, Sutter Instrument) with 0.2 µm resolution for motion control. Strain gauge signals of the insertion force, indentation force and displacement from the microprobe and silicon hinge are amplified through a four channel instrumental amplifier (EX-400, Dagan) with a gain of 500 and continuously monitored during the tweezing motion.

Two different fish (tuna and salmon) tissue samples were used due to similarity to clinical tissue. Two different tissue freshness, fresh (from the market) and non-fresh (stored for 3 days in 4℃), were performed with a total of ten tests on measuring different tissue properties. The tissue electrical impedance is measured by using impedance analyzer (HP4194A) through the platinum electrodes located on the sharp probe. Total twenty sets of impedance data are collected in air and tissue. All data is collected by a data acquisition system (USB-6259, National Instrument) to a host computer and processed by MATLAB program. An example data set for insertion force, indentation
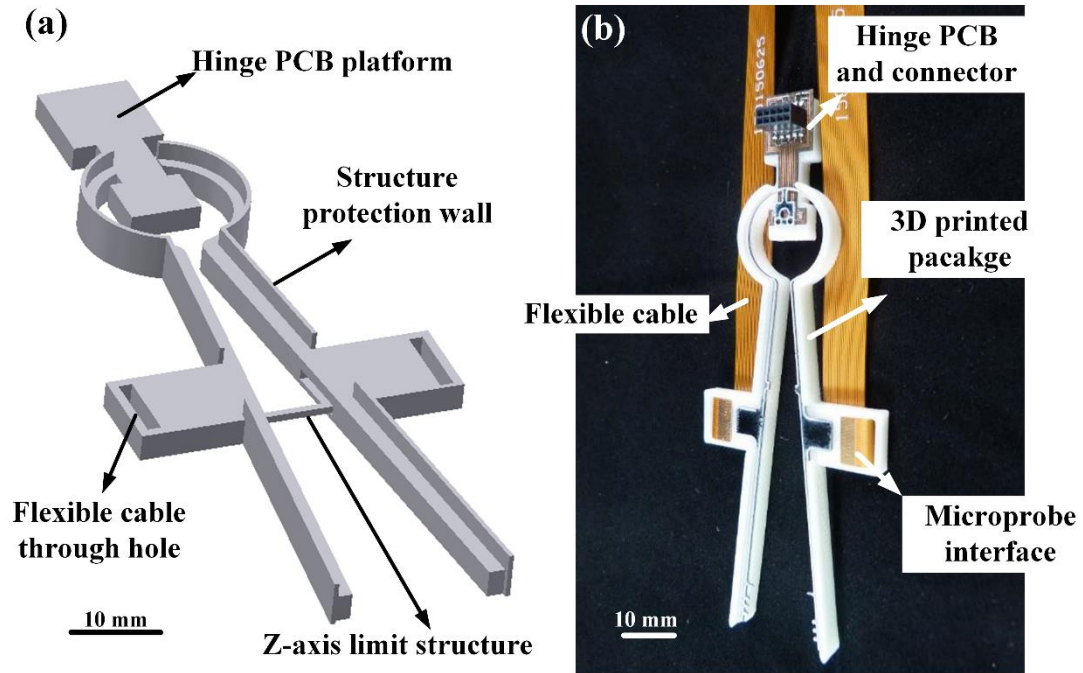
Figure 4.6: (a) 3D printed package for the tweezer device. An extended platform on the top of the tweezer is used for holding hinge PCB. Two through holes at the arm location is used for installing flexible cables. A z-axis limit structure between two legs is designed to increase the out-of-plane rigidity. (b) Picture of assembled silicon tweezer with two flexible cable interfacing microprobes and one hinge PCB for interfacing the displacement sensor on the hinge structure.
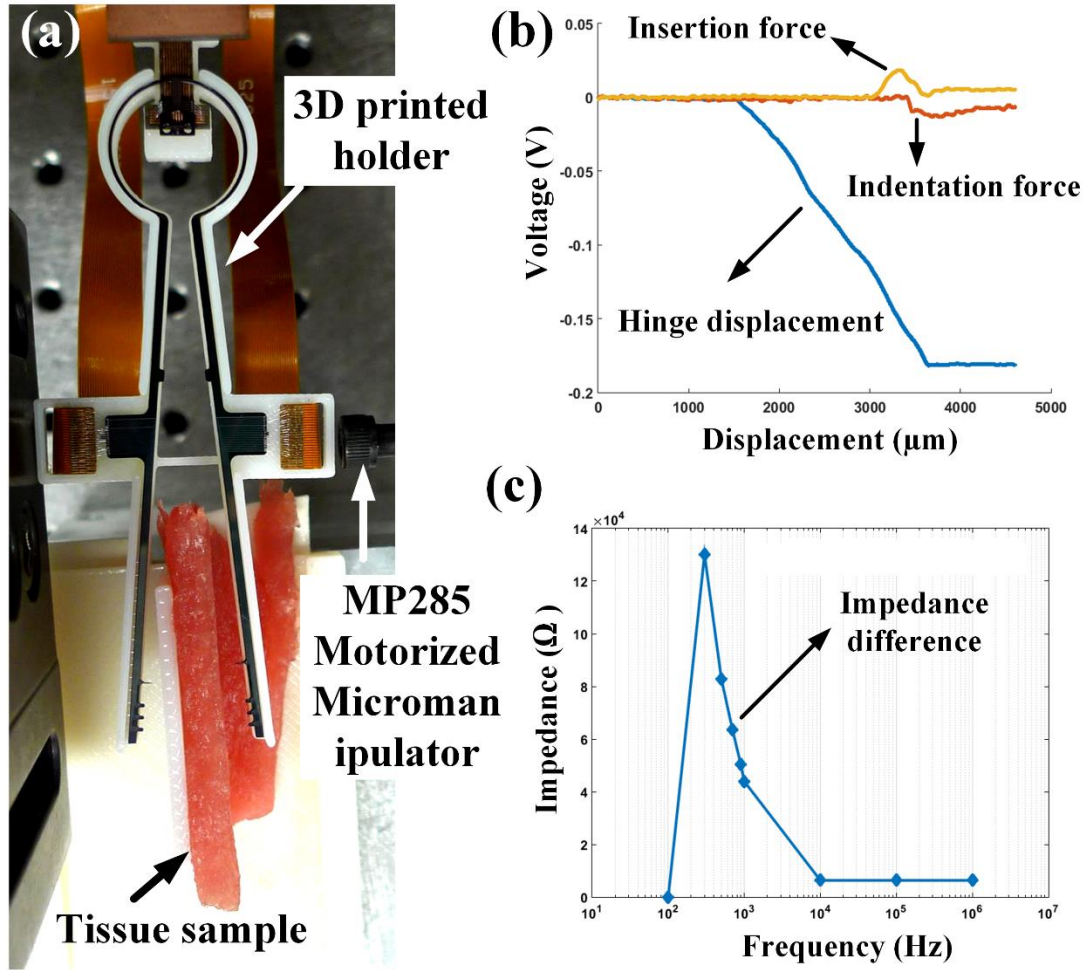
Figure 4.7: (a) Picture of the experimental setup. Tissue sample is held between two legs of the tweezer. One side of the tweezer is fixed while the other side of the tweezer is tweezed by a motorized micromanipulator. (b) Example data set for the insertion force, indentation force, and displacement sensor. The insertion force signal raise prior then the indentation force is due to the length of the insertion probe is longer than the indentation probe. (c) Example data set for tissue electrical impedance measurement with frequency range from 100 Hz to 1 MHz.

force and hinge displacement is shown in (Figure 4.7(b)) The insertion signal raise prior then the indentation force is due to the length of the insertion probe is longer than the indentation probe. The electrical impedance difference between tissue and air is shown in (Figure 4.7(c)).

4.3.1 Bioimpedance measurement results

Tissue electrical impedance is a function of its structure, and it can be used to differentiate normal and cancerous tissues in a variety of organs, including breast, cervix, skin, bladder and prostate [98]. Biological tissue structure exhibit two electrically conducting compartments, the extra- and intracellular spaces separated by insulating membranes. The conduction of electric current through such a structure is highly frequency dependent [99]. The conductivity reflects the conduction properties of the tissue. Therefore, the tissue impedance spectrum in the frequency ranges up to about 1MHz reflects the properties of the structures. This frequency-dependent relationship between impedance (Z), conductivity (σ) and relative permittivity (ε_r) is given by the expression [100]

$$Z = Z' + j\omega Z'' = 1/(\sigma + j\omega\varepsilon_0\varepsilon_r) \qquad (4.7)$$

where Z is the total impedance, Z' and Z'' are the real and imaginary components of Z respectively, ω is the radial frequency, and ε_0 is the permittivity of free space. The total impedance for two different fish tissue sample are measured under seven frequency, range from 100 Hz to 1 MHz (Figure 4.8). At low frequencies of applied electric field, the membrane is highly resistant and, a low electric current will travel in the extracellular fluid surrounding the cells, hence the impedance is very high. As the frequency increases, this impedance decreases as the resistance drops due to its predominate capacitive behavior. At very high frequency, since $Z''=X_c=1/2\pi fC$ and Z'

is very small, the membrane impedance approaches zero and the membranes appear as a short circuit; the electric filed lines pass more uniformly through the tissue structure as the impedance decreases towards its minimum value [101], [102]. An equivalent circuit model is used to model the behavior (Figure 4.9), where C_a is the capacitor modeling the intracellular bilayer membranes, R_a is the modeling of the electrolyte between membrane structures and R_p represents the resistance of the dc-path across the extracellular environment. Tuna has 22.8 % higher total impedance than salmon while fresh at 1 kHz. After three days, the impedance for both tuna and salmon decreased. The decrease in impedance is due to the increase spoilage caused by micro-organisms or enzymes, the concentration of dissolved ionic metabolic products would increase, resulting in an increase in conductivity, or a decrease in system impedance. The similar results had been shown in the different studies [103]–[105].

4.3.2 Tissue Young's modulus results

To measure the elastic properties of the tissue, applied force and indentation deformation are required to be measured simultaneously. In this design, the force can be measured by the integrated strain gauge in the round shape probe, and the distance of deformation can be measured through strain gauge integrated on the hinge. The hinge displacement sensor was characterized under a motorized micromanipulator with 20 nm resolution. Figure 4.10 shows the output voltage signal from strain gauge versus displacement in both compressing (blue line) and relaxing (red line) direction. Linear curve fitting (green line) is performed for the displacement function. The results indicate that there is no hysteresis between the direction of motion, and the sensitivity of the hinge displacement sensor is 101.2 µV/µm with a noise equivalent displacement of 41.8 fm. The force can be measured by the integrated strain gauge from the round shape
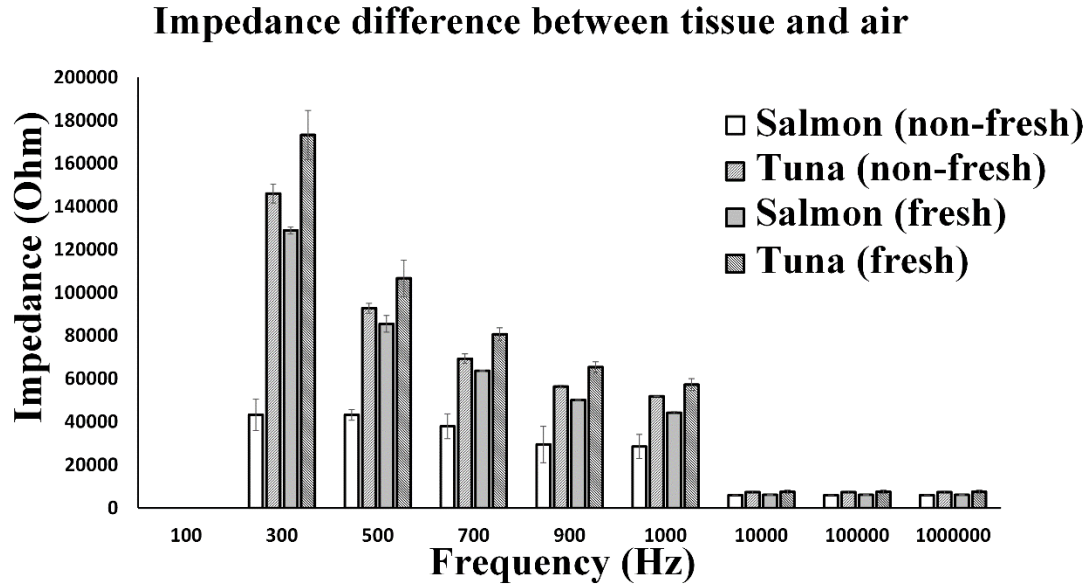
Figure 4.8: Tissue impedance measurement with two different tissue sample under different freshness.
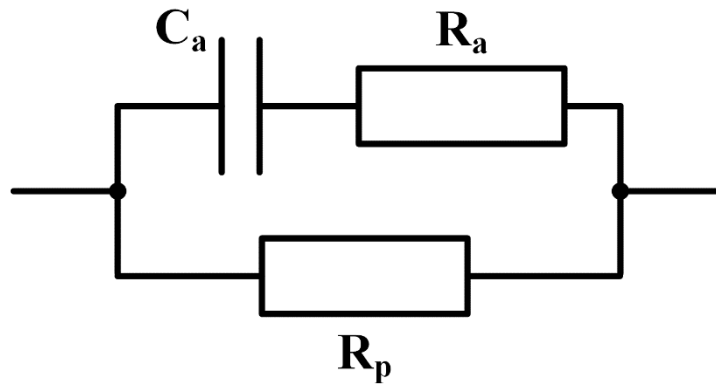
Figure 4.9: Equivalent circuit model for biological tissue impedance. C_a is the capacitor modeling the intracellular bilayer membranes, R_a is the modeling of the electrolyte between membrane structures and R_p represents the resistance of the dc path across the extracellular environment.
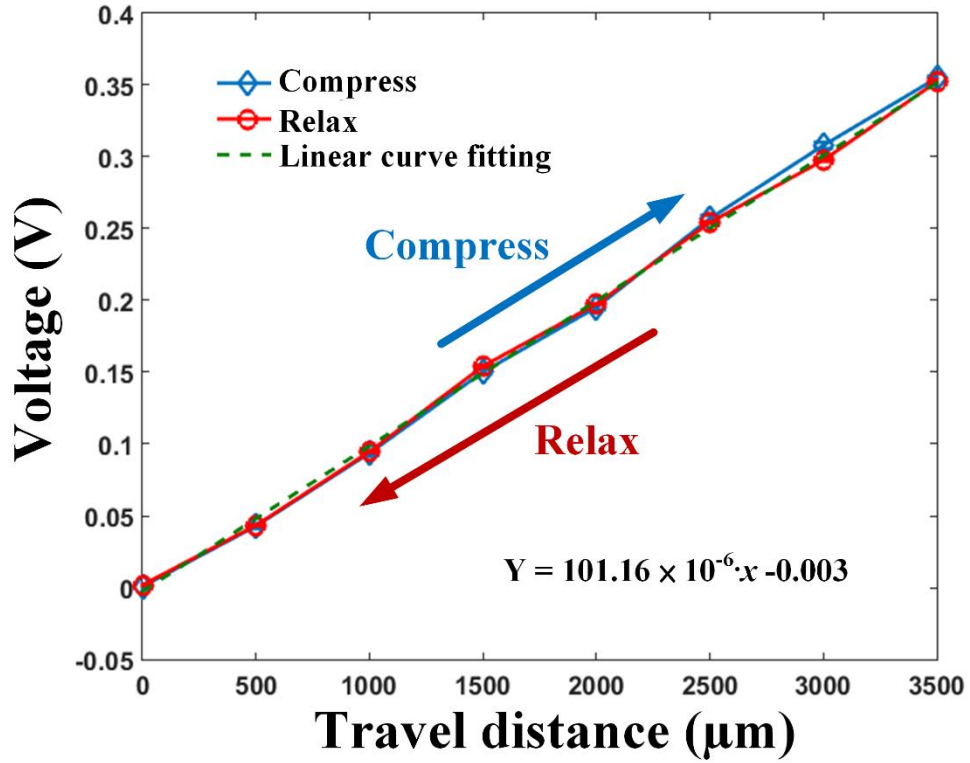
Figure 4.10: Hinge displacement sensor output of different direction of motion, compress (blue line) and relax (red line) versus the travel distance from the motorized micromanipulator. From the linear curve fitting (green dot line), we obtain a sensitivity of 101.2 µV/µm from the hinge displacement sensor.

probe. The round shape microprobe will indent tissue longitudinally during tweezing motion. The force can be expressed as [87]

$$F = \frac{4}{3}\frac{E_{tissue}}{1-v^2}\delta^{\frac{3}{2}}R^{\frac{1}{2}} \tag{4.8}$$

where E_{tissue} is the tissue Young's modulus, δ is the displacement, v is the Poisson's ratio (0.5 [106]), and R is the radius of the sphere indenter (250 μm). The tissue Young's modulus can further be expressed as

$$E_{tissue} = \frac{2 \cdot V_{out}}{V_{bridge} \cdot GF} \cdot A \cdot E_{sillicon} \cdot \frac{3}{4}(1 - v^2)\delta^{-\frac{3}{2}}R^{-\frac{1}{2}} \tag{4.9}$$

where V_{out} is the voltage output from the Wheatstone bridge, V_{bridge} is the voltage across the bridge (3V), GF is gauge factor of the polysilicon piezoresistor (10), A is the contact area of the probe to tissue (2×10^{-9} m^2), , and $E_{silicon}$ is the silicon Young's modulus (169 GPa). Two different fish tissue with different freshness sample is tested, and the Young's modulus is shown in (Figure 4.11). The tuna has 26.6 % higher Young's modulus than salmon while fresh. When freshness goes down, the tissue Young's modulus decreases by 56.85 % and 46.61 % for salmon and tuna, respectively. The decrease in the Young's modulus is due to the spoilage.

4.3.3 Tissue insertion force results

The insertion force is measured by the sharp probe with polysilicon resistors in half bridge configuration. Since the sharp probe geometry is as same as the ultrasonic neural probe, for the half bridge configuration the piezoresistor force sensitivity is half of sensitivity described in Chapter 2.3, 70 V/N. The insertion force for the two different fish tissue and freshness sample is shown in Figure 4.12. The insertion force for fresh tuna is 38.47 % higher than fresh salmon. Interestingly, the insertion force increases by 29.13 % for the non-fresh tuna, but stay approximately the same for non-fresh salmon.

4.4 *Conclusion and future directions*

Given all these measurement results, we can see tuna had higher Young's modulus, insertion force, and electrical impedance than salmon. Interestingly, these parameters can also identify tissue freshness; the fresh tissue tends to have lower Young's modulus, but higher insertion force, and impedance. A three-dimensional cluster plot for four
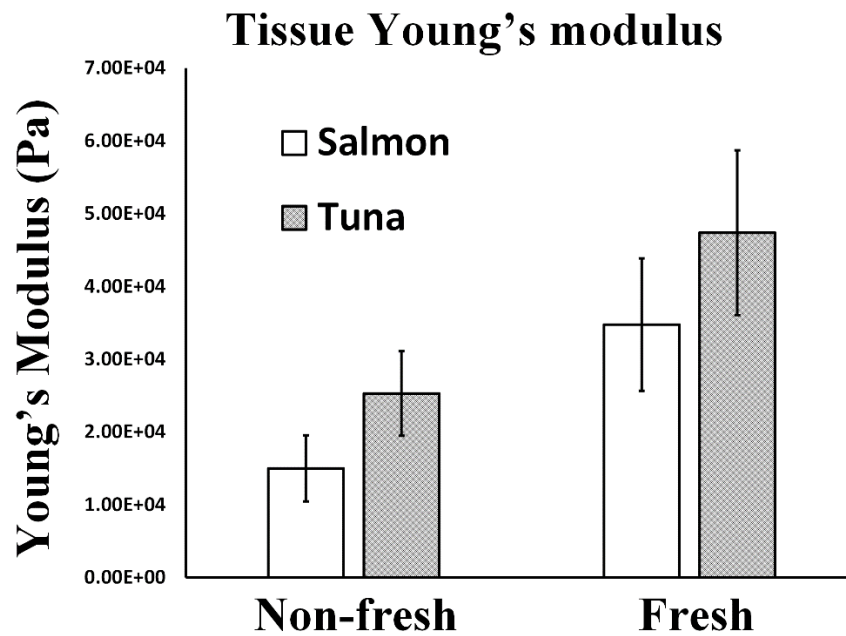
Figure 4.11: Young's modulus measurement of two different tissue sample with two different freshness
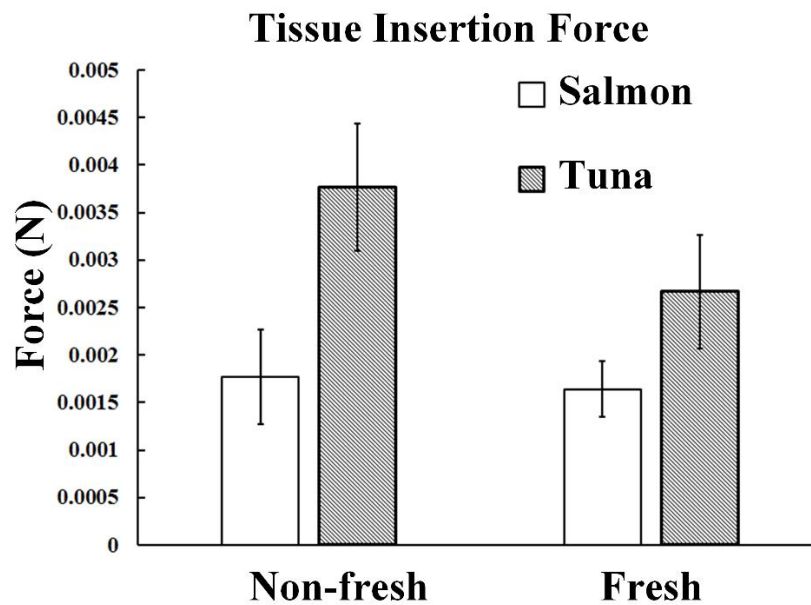
Figure 4.12: Insertion force measurement of two different tissue sample with two different freshness.
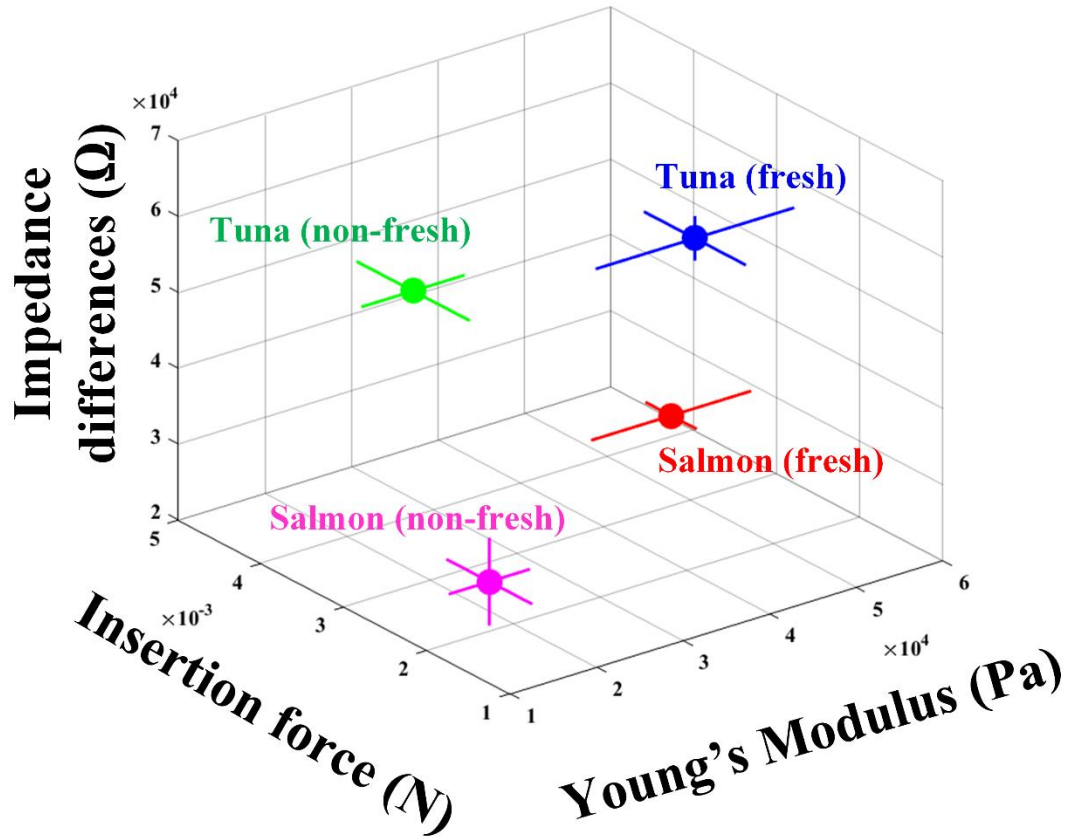
Figure 4.13: 3D cluster plot for multimodal tissue properties for two different tissue sample with two different freshness.

different tissue samples is shown in Figure 4.13, demonstrating tissue type and age determination.

In this chapter, we present a silicon tweezer that can be used for measuring multiple tissue property, and for the first time using polysilicon strain gauges for displacement measurement. The silicon tweezer structure can perform tweezing motion without silicon fracture, and the displacement can be monitored by the displacement sensor integrated on the hinge. We also report for the first time, simultaneous measurement of tissue Young's modulus, insertion force, and electrical impedance, to distinguish

different tissue type and changes in tissue types after aging. Two different types of microprobes with different penetration force versus distance are designed to measure indentation and insertion. Two platinum electrodes are integrated on insertion probes for electrical impedance measurement. This device can potentially provide more information for surgeons during the surgery operation.

In the future, more various tissue samples, especially cancerous versus benign tissue, should be investigated. For the multimodal tissue characterization tweezer platform, an algorithm can be developed based on the measurement for narrowing down the patient-specific criteria to further provide more accurate assay results. A miniaturized recording and wireless transmitting system can be developed toward a more probable device during the surgery operation.

CHAPTER 5

ULTRASONIC VISCOMETER WITH INTEGRATED DEPTH MEASUREMENT

5.1 *Introduction*

Measurement of fluid viscosity has played a significant role in both industrial and medical applications to monitor state of industrial fluids such as intermediate chemical products of food and chemical industries, and biological fluids such as blood. Miniaturized liquid sensors are critical devices for quality control and condition monitoring when sample sizes are small, or when sensing need to be done in the field. Conventional laboratory equipment to measure viscosity, for example, capillary tubes, rotating and falling ball or needle viscometers, can measure viscosity at a specified constant shear rate. However, these devices often cannot be used in applications constrained by cost, space, and portability requirements. Moreover, measurements from existing devices often involve manual labor and require large sample volume. In the case of viscosity and density sensing, microacoustic wave sensors, such as piezoelectric crystals and electroceramics have been used extensively for the measurement of fluid viscosity. The physical properties of the fluid can be extracted from the shift in the resonant frequency, the quality factor and the vibration amplitude of a resonator. Quartz thickness shear mode (TSM) resonators [107], [108] and surface acoustic wave (SAW) devices [109] have proved particularly useful alternatives to the traditional viscometers [110]. However, these devices measure viscosity at comparatively high frequencies at small vibration amplitudes. The high frequency of operation limits these devices to the measurement of thin liquid layers, owing to the low shear viscous depth and smaller bulk absorption depth. The depth of penetration can be express as

$$\delta = \sqrt{\frac{2\mu}{\omega\rho}} \qquad\qquad (5.1)$$

where μ is the viscosity, ω is the angular oscillation frequency and ρ is the fluid density. The penetration of depth of water in 1 MHz is only 0.4 μm. These parameters are often not accurately comparable to the macroscopic parameters probed by conventional viscometers operating at 1-100 Hz in liquid. For example for liquids such as emulsions, it had also been shown that microacoustic device may not be sufficient to detect rheological effect that are present only on the macroscopic scale [111].

Micromachined vibrating structures, such as miniaturized cantilever-based devices [112] offer an alternative for non-Newtonian and complex liquids with a lower resonance frequency and higher vibration amplitudes. Microcantilevers commonly used in atomic force microscopy [113] have been successfully used as liquid viscometers. They allow for simultaneous measurement of viscosity and mass density of the liquid, require sample volumes of less than one nanoliter [114]. However, the optical readout is needed to measure vibration amplitude of the cantilever beam. Strong deterioration of the quality factor while immersed in the liquid due to high-dissipative effects limited the measurement range to low viscous fluids. In other works, micromachined cantilevers and double clamped beams driving by Lorentz force [115], or by the piezoelectric effect [116] have been utilized as liquid property sensors, and the feasibility of these sensors has been demonstrated for viscosities in the range up to several Pa·s. Optical techniques derived from the damping of an immersed vibrating structures, such as micropipette and optical fiber, have also been used for fluid viscosity measurement [117].

Another challenge in viscosity measurement with a probe is the precise immersion depth control, which directly controls the change in the variable being measured. The

Table 5.1: Summary of depth of penetration (δ) of different viscous liquid sample under different operation frequency

Sample	δ @ 100kHz	δ @ 300kHz	δ @ 450kHz
Honey	33.5 μm	19.33 μm	15.8 μm
AK350 silicon oil	26.7 μm	15.4 μm	12.6 μm
AK150 silicon oil	14.6 μm	8.45 μm	6.90 μm
Ethylene Glycols	5.34 μm	3.08 μm	2.52 μm
Milk	2.15 μm	1.24 μm	1.01 μm
Blood	2.12 μm	1.23 μm	1.00 μm
Water	1.26 μm	0.72 μm	0.59 μm

depth control limits the measurement accuracy as cumbersome optical systems are needed to measure the depth of insertion. For handheld portable viscosity measurements, such as those for biomedical sample testing, one needs to be able to measure the viscosity where the complete insertion of the probe may not be possible, due to the need to measure quickly or the need to measure in volumes in which the depth is varying. This is case when one needs to measure viscosity of a liquid in a droplet with unknown or variable volume. Here we demonstrate a viscometer that can measure fluid viscosity by monitoring the fluid damping effect on immersed vibrating silicon microprobes integrated with polysilicon strain gauge while keeping track of the depth of insertion. Silicon ultrasonic horn actuators have been reported previously for exciting flexural vibration mode in microprobes integrated at the tip of the horn and used as a viscometer [28], [118].

In this chapter, a similar ultrasonic microprobe was fabricated with piezoresistive strain gauges integrated on the microprobe to measure its vibration amplitude. The

116

silicon cantilever beam is actuated at its λ/2 longitudinal resonance, 95 kHz. From Equation (5.1), the shear viscous depth of penetration of the device operating at couple hundred of kHz with different viscous liquid is summarized in Table 5.1. The damping in the vibration of the microprobe is quantified by the strain gauge when immersed in viscous reference standard solutions with different viscosities. Device design, fabrication, and characterization

5.1.1 Structure design

The ultrasonic viscometer is comprised of 1) a silicon beam structure, 2) polysilicon piezoresistors and 3) pores array along the silicon beam structure (Figure 5.1(a)-(c)).

Silicon beam: The beam ($2.5 \times 50 \times 0.5$ mm^3) is designed to drive at its half-wavelength resonance frequency by PZT. This mode excited by the actuator are a combination of surface motion generating the shear strain in liquid and an out-of-plane motion drive bulk mode into the liquid. From finite element simulation (Figure 5.2), a half-wavelength longitudinal resonance frequency of 94.8 kHz is expected, which is close to the impedance analyzer (HP4194A) measurement on the fabricated device (95.2 kHz).

Polysilicon piezoresistors: To monitor the vibration amplitude damping of the device while immersing into viscous liquids. Four sets of polysilicon piezoresistor strain gauges are integrated for the vibration amplitude sensing. In each set strain gauge, two polysilicon resistors (passive) are positioned perpendicular to the longitudinal mode direction that sense less strain at the longitudinal mode while the other two piezoresistors (active) are positioned in parallel to maximize the strain (Figure 5.3(a)). The output voltage of the strain gauge, V_{out} can be written as a function of the stain.

117
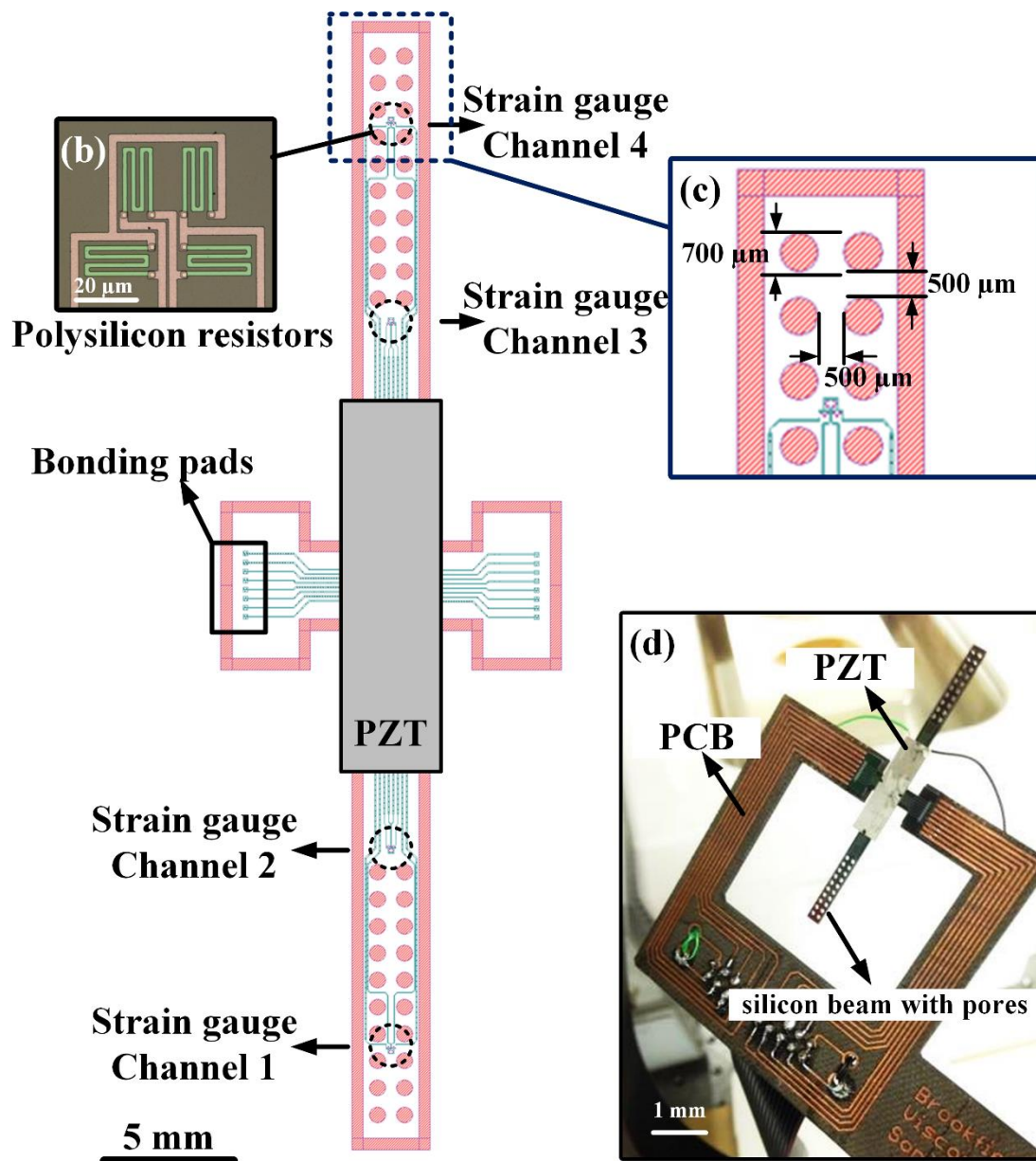
Figure 5.1: Ultrasonic viscometer with integrated depth sensors. (a) Layout view of the viscometer, (b) integrated polysilicon piezoresistor strain gauge in Wheatstone bridge configuration, (c) pores structure on the cantilever beam, and (d) optical photos of assembled device.

(a)

Longitudinal mode @ 94.78 kHz
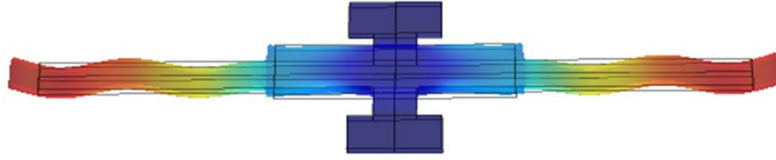
(b)

Impedance
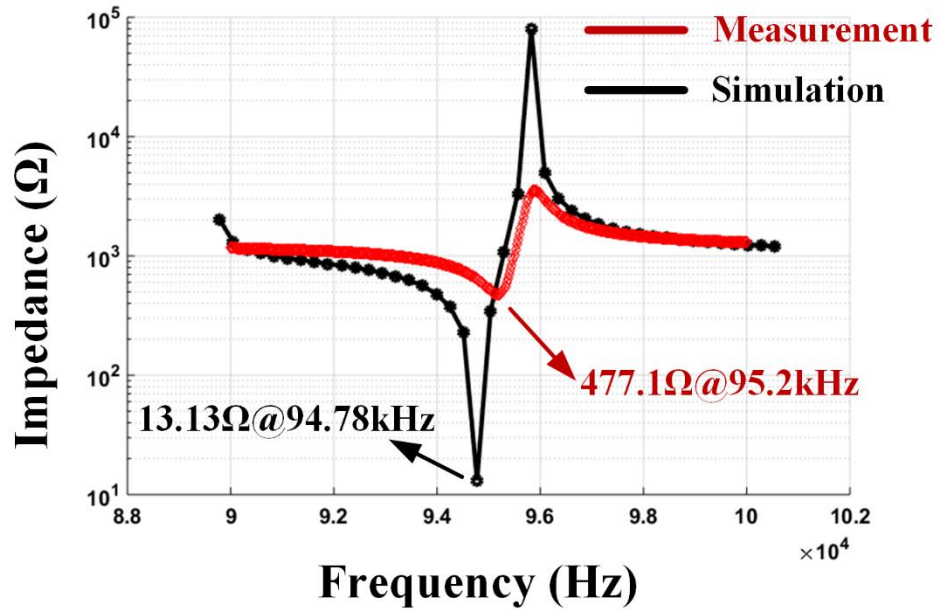
Figure 5.2: (a) COMSOL simulation on longitudinal mode at 94.78 kHz. (b) Motion impedance simulation versus measurement results.

$$V_{out} = V_{bridge} \cdot \frac{\Delta R}{2R} = V_{bridge} \cdot \frac{GF \cdot \varepsilon}{2} \qquad (5.2)$$

where V_{bridge} is the bridge exciting voltage, GF is the gauge factor of the piezoresistor, and ε is the strain. In order to maximize the sensitivity, strain gauges are placed across the beam in the maximum strain of the silicon at longitudinal mode (Figure 5.3(b)). Four
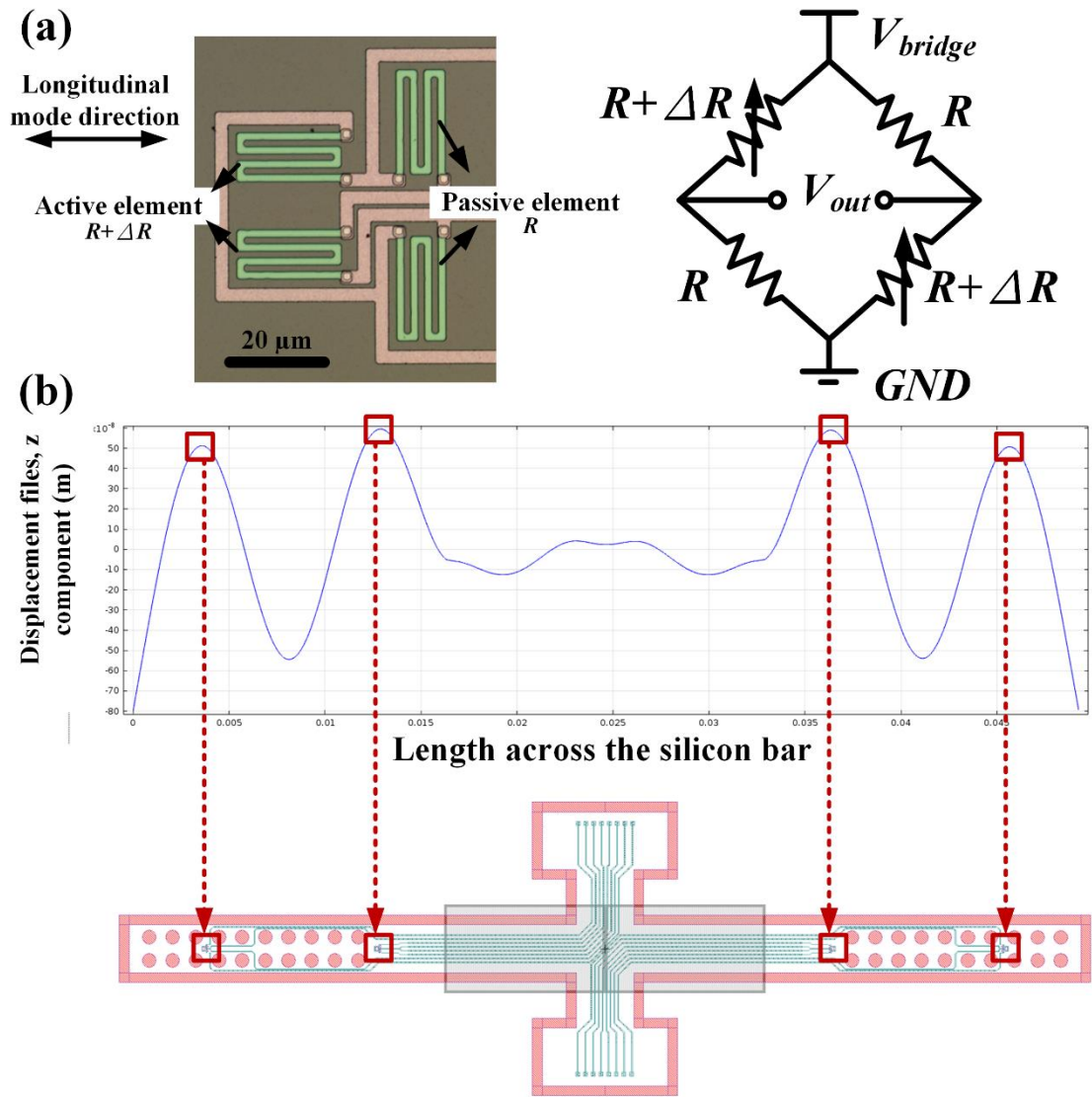
Figure 5.3: (a) Polysilicon piezoresistor in Wheatstone bridge configuration. (b) Strain gauges are placed on the maximum strain along with the silicon beam structure.

sets of strain gauges are used to differentially measure strain to subtract common mode shift in strain due to temperature and electromagnetic noises.

Pores array: Two rows of 700 μm pores are used as immersion depth indicator by manipulating the contact area while moving into the liquid. The total contact area (Figure 5.4) can be expressed as $A(z) = A_0 + (A_n + A'(z)), n = 1,2,3\,...,$ where z is the direction along the cantilever beam, A_0 is the initial area, $A'(z)$ is the area with pores and n is the number of segment. Area with pores can be express as

$$A'(z) = wz + zh - 2h\left[\frac{r^2}{2}\left(\frac{2\cos^{-1}\left(r - \frac{z}{r}\right)\pi}{180^o}\right) - \sin(2\cos^{-1}\left(r - \frac{z}{r}\right))\right] \qquad (5.3)$$

where w is the width of the cantilever beam, h is the thickness of the cantilever beam and r is the radius of the pore. Figure 5.4 shows the total contact area versus immersion depth between pores design (red line) and non-pores design (blue line). Reduced contact area will cause reduced damping of the silicon structure and create discrete jumps in the transducer amplitude upon immersion in liquid. These discrete jumps cause steps in the transducer amplitude, due to increasing the sensor-liquid contact area in stepwise fashion, which can provide the immersion depth and liquid viscosity information simultaneously. The profile of transducer amplitude can also be used to estimate the speed of insertion into the liquid.

5.1.2 Fabrication process flows and device assembly

A silicon beam ($2.5 \times 50 \times 0.5$ mm^3) is fabricated from a 500 μm thick silicon wafer using through wafer DRIE dry-etching with standard Bosch process. Two rows of 700 μm diameter pores are co-fabricated at the same time. Four polysilicon resistors arranged in single balanced Wheatstone bridge configuration are integrated on the

Area versus immersion depth
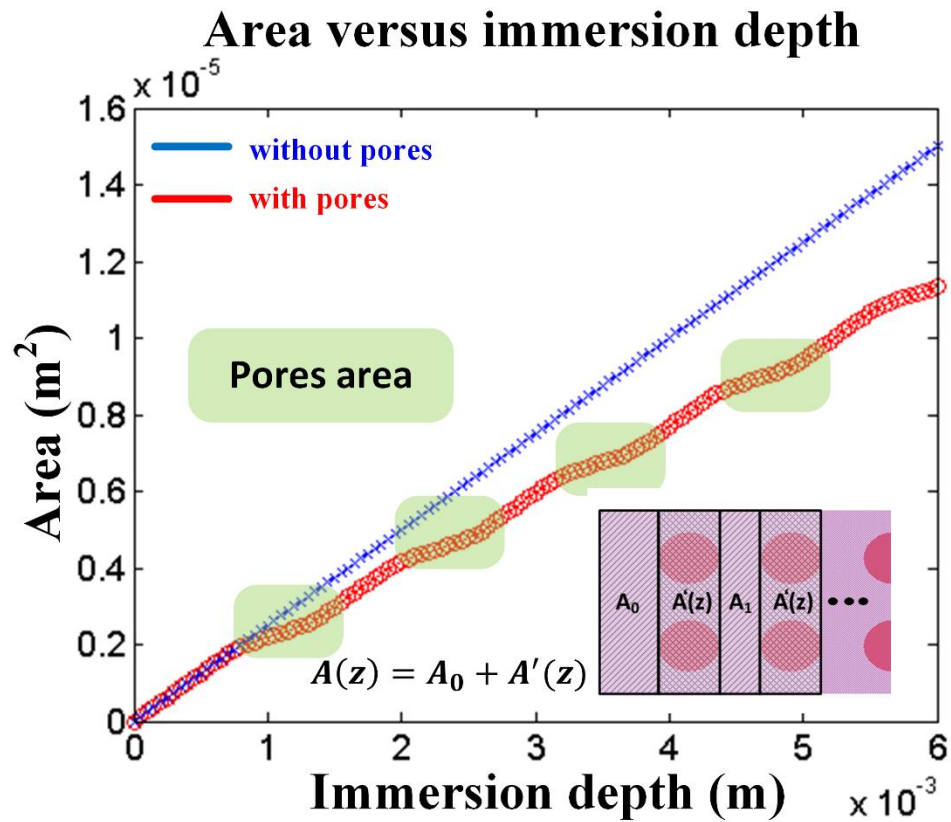
Figure 5.4: Contact area versus immersion depth between pores and non-pores design.

The chart shows:
- **without pores** (blue)
- **with pores** (red)
- Pores area
- $A(z) = A_0 + A'(z)$
- Axes: Area (m^2) ($\times 10^{-5}$) versus Immersion depth (m) ($\times 10^{-3}$)
- Inset labels: A_0, $A'(z)$, A_1, $A'(z)$ $\cdots$

Legend:
- Silicon
- LPCVD Nitride
- Polysilicon
- Oxide
- Aluminum+1%Si
- PECVD Nitride

Bonding pad   Strain gauges   Pores structure
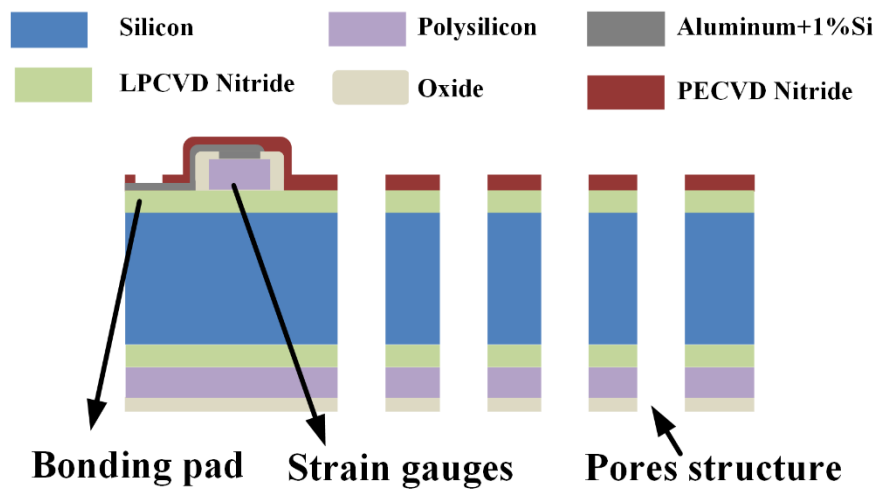
Figure 5.5: Fabrication process flows (Process cross section)

surface of the beam. The fabrication of the ultrasonic viscometer is similar to the ultrasonic neural probe and silicon tweezer described in the previous chapters. Briefly, polysilicon strain gauge resistors are realized by LPCVD polysilicon implanted with boron at a dose of 2×10^{15} ions/cm^2 at 100 keV. The resistors are electrically contacted with aluminum alloy (Al + 1% silicon) metal lines. PECVD nitride is deposited as an insulation layer. During the through wafer etching, a polymer coating Protek SR-25 is spun to protect the front side features. The fabrication process cross section is shown in (Figure 5.5). One Lead Zirconate Titanate Oxide (PZT-4H) piezoelectric plate (17.48 × 3.2×0.5 mm^3) is affixed to the zero-displacement nodes of the longitudinal mode shape. The PZT/silicon actuator is then adhesively bonded to a PCB, and the contact metal pads on the actuator are wire-bonded to the PCB (Figure 5.1(d)).

5.2 *Experimental results*

The ultrasonic viscometer is affixed on a precision motorized micromanipulator (MP285, Sutter Instrument) with 0.2 μm resolution for motion control. To drive the device at correct longitudinal resonance frequency, PZT motional current is monitored periodically with an impedance analyzer (HP4194A) to track the frequency variation throughout each experiment. A function generator with a piezo amplifier, gain of 20, are used to drive the ultrasonic viscometer at the frequency measured by the impedance analyzer. Switching control system is implemented and controlled by a microcontroller (LPC1768) between the driving and sensing the PZT of the ultrasonic viscometer. The device is positioned above viscosities reference standards around 1000 μm and moving toward the viscosities reference standards at 200 μm step with velocity of 1000 μm/s per step. The total traveling distance is 5000 µm, and the final immersion depth is around 4000 μm. During each step, four ultrasonic induced strain signal are amplified through four channel instrumental amplifier (EX-400, Dagan) with gain of 500. A data
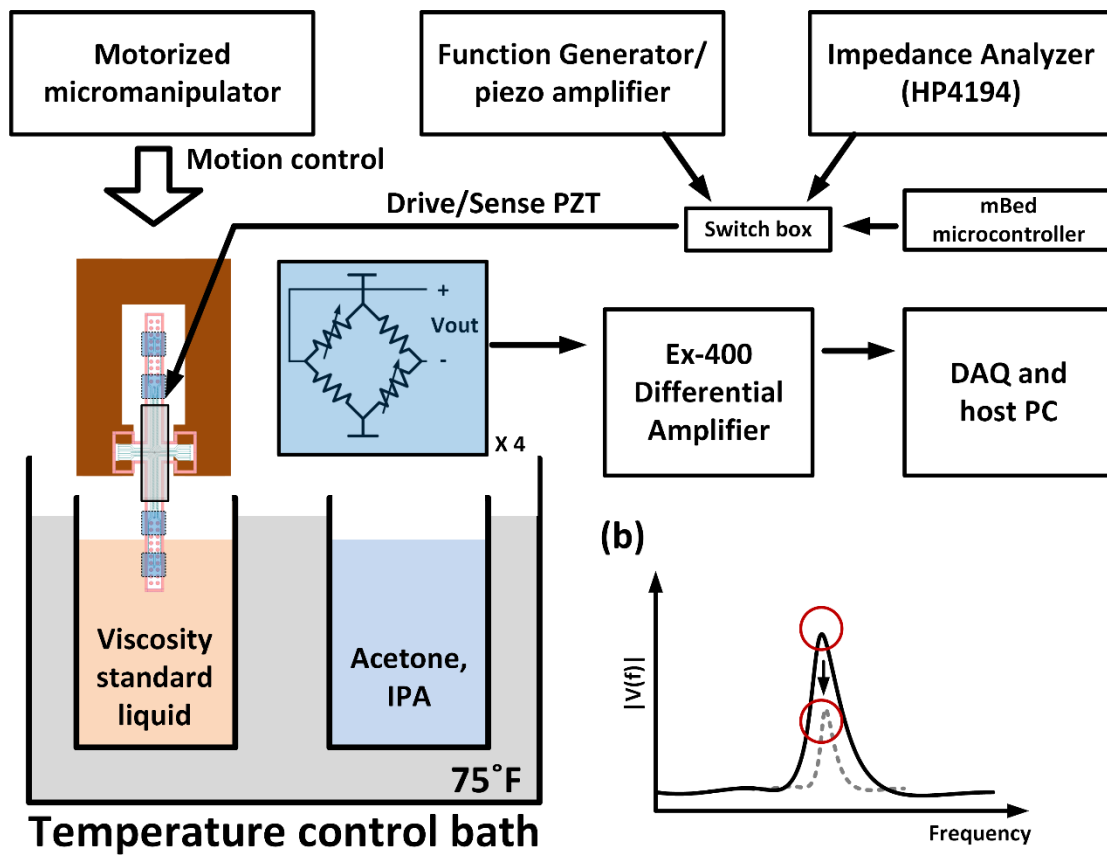
Figure 5.6: Block diagram of experimental setup (a) Motorized micromanipulator is used to control the motion of the viscometer. Function generator and piezo amplifier are used to drive PZT while impedance analyzer is used to sense the motion current of PZT to monitor the resonance frequency. Four set of strain signals is amplified by a differential amplifier and acquired by a data acquisition system and send to host PC. (b) Fast Fourier transform is performed on host PC, and the voltage variation is monitored at each immersion depth.
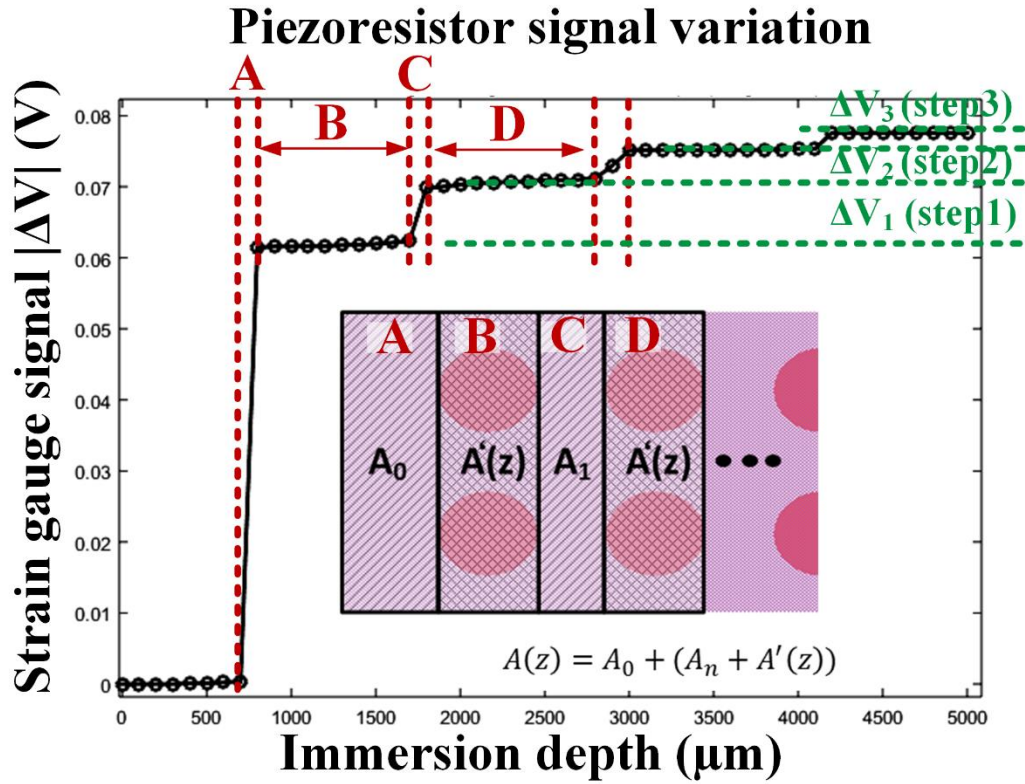
Figure 5.7: Example data set of strain signal under different immersion depth.

acquisition system (USB-6259, National Instrument) is used to record the data to a host computer. Software demodulation is performed on the host PC using MATLAB with known driving frequency to extract the voltage. The experiment setup is shown in (Figure 5.6).

Three different viscosity reference standard are tested: N2, N10 and S20 (Cannon Instrument), with dynamic viscosity of 2.0, 16, and 29 mPa·s, respectively, at 25℃. A temperature control bath is used to maintain temperature during the experiment. However, the absorption loss from the viscous loss can still cause an increase in liquid temperature due to the relative motion from the microprobe surface and viscosity reference standard. The increased temperature can be estimated from Navier-Stokes equation

$$\rho \left(\frac{\partial u}{\partial t} + u \cdot \nabla u \right) = -\nabla p + \eta \cdot \nabla^2 u + f \tag{5.4}$$

where ρ is density of medium, u is the velocity of ultrasonic vibration, p is the pressure, η is the viscosity coefficient, and f is the external force. Assuming external force and pressure gradient are not presented, and the medium is incompressible. Equation (5.4) can be simplified as

$$\rho \frac{\partial u}{\partial t} = \eta \frac{\partial^2 u}{\partial z^2} \tag{5.5}$$

The velocity of ultrasonic vibration can be written as

$$u = u_0 e^{\frac{z}{\delta}} e^{j\omega t} \tag{5.6}$$

where u_0 is the amplitude of the vibration. Substituting Equation (5.6) into Equation (5.5), we can get the following expression

$$\rho j\omega = \frac{\eta}{\delta^2} \tag{5.7}$$

Rearranging (5.7), δ can be expressed as

$$\delta = \frac{\sqrt{2}}{1+j} \sqrt{\frac{\eta}{j\omega}} \tag{5.8}$$

From Equation (5.8), Equation (5.6) can be rewritten as

$$u = u_0 e^{-\frac{z(1+j)}{\sqrt{\frac{2\eta}{\rho\omega}}}} e^{j\omega t} = u_0 e^{-\frac{z}{\delta_0}} e^{j\left(\omega t - \frac{z}{\delta_0}\right)}$$

(5.9)

$$\delta_0 = \sqrt{\frac{2\eta}{\rho\omega}}$$

where δ_0 is the viscous penetration depth, the acoustic boundary layer thickness. The mechanical power loss into medium can express as force, F, times, velocity, u. The force can be written as

$$F = W \cdot L \cdot \int \eta \frac{\partial^2 u}{\partial z^2} dz = W \cdot L \cdot \eta \cdot \frac{\partial u}{\partial z}$$

(5.10)

where W and L are the dimensions of the microprobe, and the integral of the shear stress is from the surface ($z = 0$) to infinity. From Equation (5.10), the total mechanical power loss (force times velocity) into medium can be estimated as

$$P = F \cdot u = W \cdot L \cdot \eta \cdot \frac{\partial u}{\partial z} \cdot u \cong W \cdot L \cdot \frac{\eta}{\delta_0} \cdot u^2$$

(5.11)

The one-dimension thermal diffusion equation for constant κ, ρ, and c_p (thermal conductivity, density and specific heat) can be expressed as

$$\frac{\partial T}{\partial t} = \alpha \frac{\partial^2 T}{\partial x^2}$$

(5.12)

where α is the thermal diffusivity $\alpha = \kappa / (\rho \cdot c_p)$. Since the thermal conductivity of silicon microprobe, $130 \, W/(m \cdot K)$ is three order of magnitude higher than the silicon

oil viscous standard, between 0.1 to 0.15 $W/(m \cdot K)$. Most of the heat will conduct to the silicon microprobe. The steady state temperature variation, ΔT, of silicon microprobe can be estimated as

$$\Delta T = \frac{P'}{M \cdot c_p} \tag{5.13}$$

where P' is the total energy loss of the probe, M is the mass of immersed silicon probe and c_p is the specific heat capacity of silicon, $710 \ J/(kg \cdot K)$. The steady state temperature of three different viscous standards, N2, N10, and S20, are 0.06℃, 0.17℃, and 0.22℃, respectively. Solving Equation (5.12) with constant surface temperature boundary condition, T(0,t) = T$_s$, we can obtain the temporal temperature profile in a semi-infinite domain as [119]

$$T(x,t) = T_\infty + (T_\infty - T_s) \operatorname{erf}\left(\frac{x}{2\sqrt{\alpha t}}\right) \tag{5.14}$$

Figure 5.8 shows the temperature profiles for the three different viscous standard (2, 16, and 29 mPa·s) after thirty seconds of operation time period. The maximum temperature increase is in the range of 0.06 ℃ to 0.22 ℃.

Total fifteen experiments are performed, each reference standard is repeated five times using the same device. Between each experiment, the probe went through a cleaning procedure (10 mins of Acetone sonication bath follow by two 10 mins of isopropyl alcohol (IPA) sonication bath) to ensure there is no residue on the probe. An example data set (voltage difference between air and viscous fluid) of the measurement is shown in (Figure 5.7). When the device is in the air, the voltage difference is constant. Once the microprobe contacts the viscous standard reference, a dramatic change is
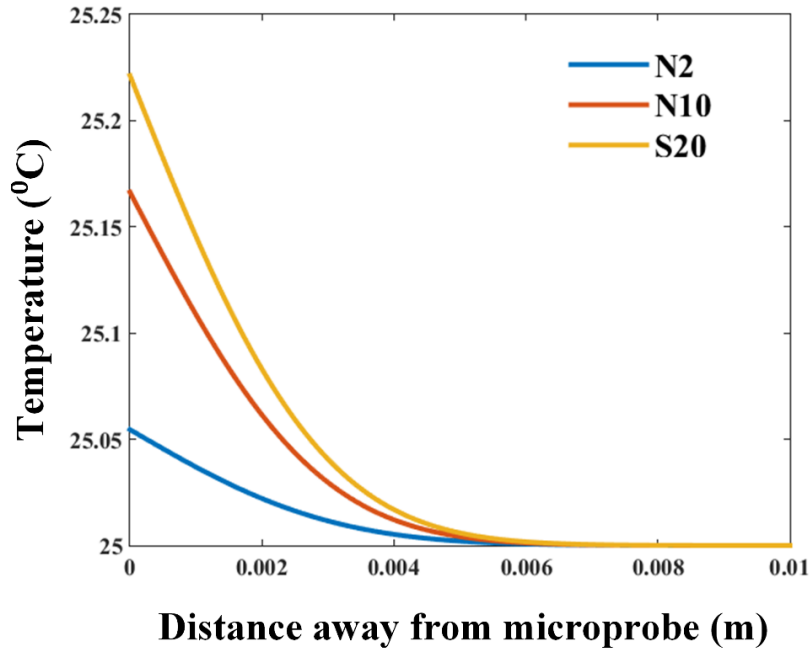
Figure 5.8: The temperature profile of three different viscous standard under 30 seconds of operation time period.

observed (point A). This is because vibration amplitude is reduced from fluid damping. While immersing through the pore structure, the signal difference increased very slightly (point B and D) due to reduced contact area. A small jump of the voltage difference is observed when the liquid experience increased contact area (point C). These voltage steps from the strain gauge signal can be used as an immersion depth indicator.

A lumped spring-mass-damper model of the viscometer leads to the motion of the device as

$$u = \frac{\frac{f}{k}}{\left(1 - \left(\frac{\omega}{\omega_0}\right)^2\right) + \frac{j\omega\eta}{k}} \tag{5.15}$$

where u is the displacement of the device, f is the force, k is the spring constant, ω_0 is the resonance frequency, ω is the operation frequency, and η is the damping terms. The damping includes damping from viscous liquid, air and adhesive between PZT and silicon structure. The damping can be expressed and simplified as

$$\eta = \eta_{viscous\ liquid} + \eta_{air} + \eta_{adhesive} + \cdots = \eta(z) + \eta' \tag{5.16}$$

where $\eta(z)$ is the damping from the viscous liquid, a function of the immersion depth and η' is damping from all other sources which is not a function of immersion depth. The quality factor of the resonator is $Q = m\omega_0/\eta$, and from Equation (5.16), Equation (5.15) can be rewritten as

$$u = \frac{\frac{f}{k}}{\left(1 - \left(\frac{\omega}{\omega_0}\right)^2\right) + \frac{j\omega}{Q(z)\omega_0} + \frac{j\omega}{Q'}} \tag{5.17}$$

While operating at resonance frequency, Equation (5.17) can be expressed as a function of quality factor: $u = \mathcal{B}(Q(z) + Q')$, where $Q(z)$ is inversely proportional to the contact area, $A(z)$ and the fluid viscosity, μ, ($Q(z) \propto 1/(A(z)\mu)$). The output voltage, V_{out}, from the strain gauges at different immersion depths, z_1 and z_2, can be expressed as

$$V_{out}|_{z_1} = \frac{\Gamma}{\mu}\frac{1}{A(z_1)} + \frac{\Gamma}{\mu}Q' = \frac{\Gamma}{\mu}\frac{1}{A(z_1)} + V_0$$

$$\tag{5.18}$$

$$V_{out}|_{z_2} = \frac{\Gamma}{\mu}\frac{1}{A(z_2)} + \frac{\Gamma}{\mu}Q' = \frac{\Gamma}{\mu}\frac{1}{A(z_2)} + V_0$$

where Γ is a constant. By subtracting two output voltage, ΔV, the fluid viscosity can be expressed as a function of the ΔV.

$$\Delta V = V_{out}|_{z_1} - V_{out}|_{z_2} = \frac{\Gamma}{\mu}\left(\frac{1}{A(z_1)} - \frac{1}{A(z_2)}\right) \tag{5.19}$$

From equation (5.19), voltage difference (ΔV_1, ΔV_2, and ΔV_3 in Figure 5.7) between each step are used to determine the fluid viscosity. Figure 5.9 shows the voltage at different step with different viscous reference standard. While increasing immersion depth, the vibration voltage decreased. The decreased voltage is proportional to the viscosity. Figure 5.10 shows the voltage differences between step2 and step1 versus different viscosity. From the vibration amplitude measured by the strain gauges, we were able to quantify the damping in the fluid that is proportional to the viscosity and immersion depth information can be extracted simultaneously.

5.3 *Conclusion and future directions*

In this chapter, we demonstrate an ultrasonically actuated silicon viscometer with integrated immersion depth sensor and strain gauges. We presented a microfabricated silicon ultrasonic sensor with integrated holes and four sets of piezoresistive strain gauge for viscosity measurement. The silicon beam is actuated at its $\lambda/2$ longitudinal resonance frequency, 95 kHz, by a PZT plate bonded at its longitudinal mode node. The modes excited by the actuator are a combination of surface motion generating the shear strain in liquids and an out-plane motion drive bulk mode into the liquid. Two rows of 700 μ m pores are used to create a depth dependent varying liquid sampling volume. The viscosity is measured by changes in the transducer strain signals upon immersion in liquid. Steps in the strain signal are obtained by increasing the sensor-liquid contact area in a non-continuous steps, which can provide the immersion depth and liquid

131
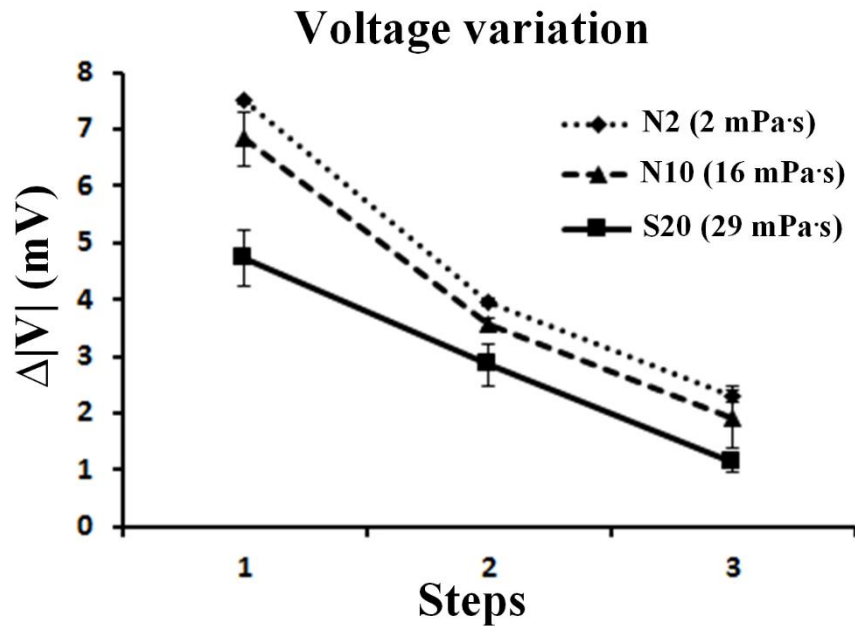
Figure 5.9: Strain gauge signal difference with various viscous reference standard at various steps
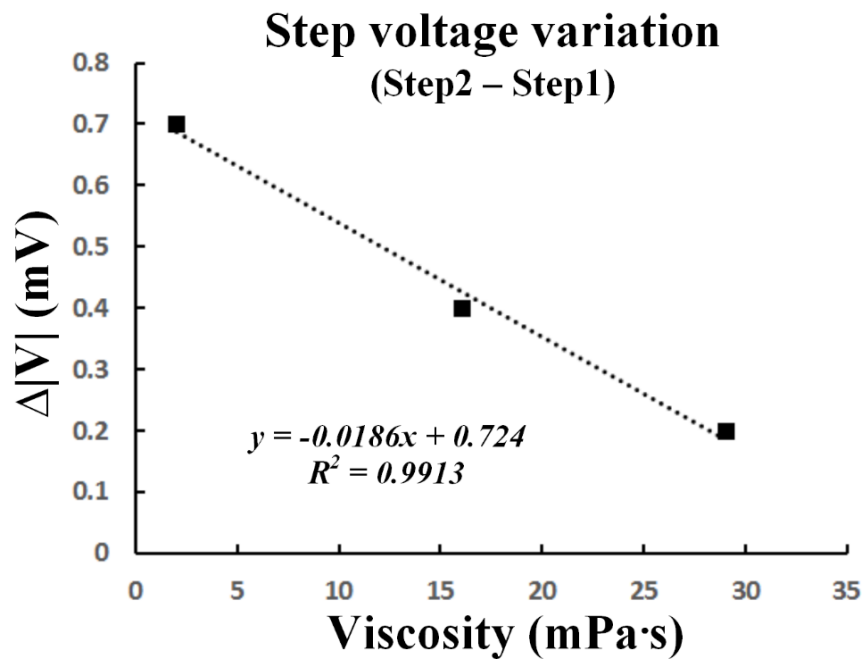
Figure 5.10: Strain gauge signal difference of steps at different viscosity sample.

viscosity information simultaneously. The pure transverse mode with resonance frequency of 8.7 kHz is also tested, however, pores structure non-continuous step response did not observed. The microprobe was characterized in various bulk viscosities reference standards. From the vibration amplitude measured by the strain gauges, we were able to quantify the damping in the fluid that is proportional to the viscosity. The immersion depth and viscosity information from the liquid can be measured simultaneously. This can potentially solve a major problem of depth calibration in the portable application of ultrasonic viscometers.

The viscous reference standard used in this work is a Newtonian fluid that is independent of the shear rate. In the future, the capability of measuring non-Newtonian fluid such as blood need to investigate by changing PZT actuation voltage to change amplitude and velocity of longitudinal (shear) vibration in the fluid.

CHAPTER 6 APPENDIX

6.1 *Ultrasonic horn layout generator GUI*

Matlab GUI code for generating different catenoidal horn dimensions in CIF (Caltech Intermediate Form) format. The GUI is shown in Figure 6.1.
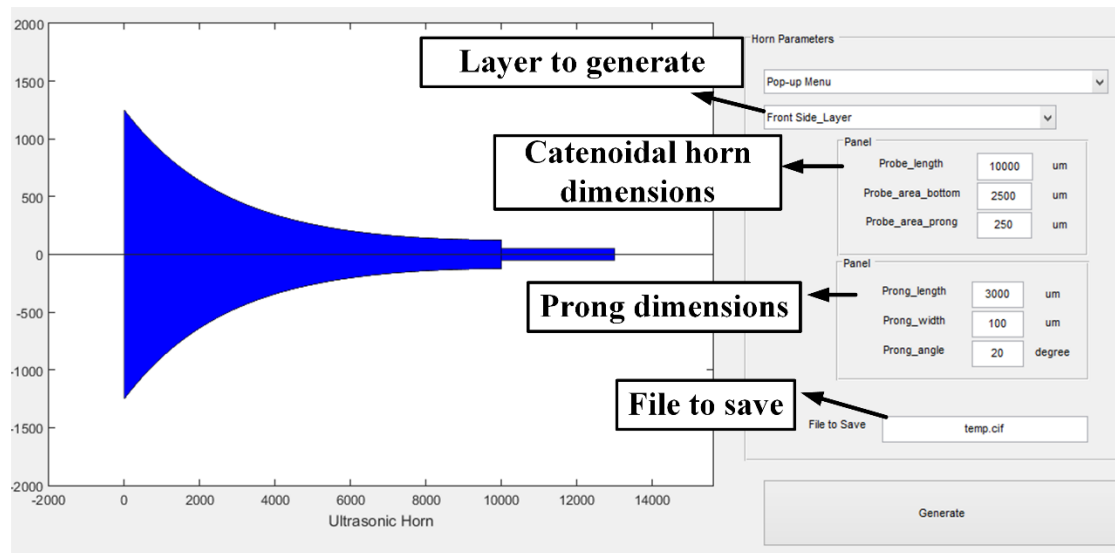
Figure 6.1: GUI for the catenoidal horn generator.

```matlab
function varargout = UltrasonicHornGenerator_GUI_v2(varargin)
% ULTRASONICHORNGENERATOR_GUI_V2 MATLAB code for
UltrasonicHornGenerator_GUI_v2.fig
%      ULTRASONICHORNGENERATOR_GUI_V2, by itself, creates a new
ULTRASONICHORNGENERATOR_GUI_V2 or raises the existing
%      singleton*.
%
%      H = ULTRASONICHORNGENERATOR_GUI_V2 returns the handle to a new
ULTRASONICHORNGENERATOR_GUI_V2 or the handle to
%      the existing singleton*.
%
%
ULTRASONICHORNGENERATOR_GUI_V2('CALLBACK',hObject,eventData,handles,.
..) calls the local
%      function named CALLBACK in ULTRASONICHORNGENERATOR_GUI_V2.M
with the given input arguments.
%
%      ULTRASONICHORNGENERATOR_GUI_V2('Property','Value',...) creates
a new ULTRASONICHORNGENERATOR_GUI_V2 or raises the
%      existing singleton*.  Starting from the left, property value
pairs are
%      applied to the GUI before
UltrasonicHornGenerator_GUI_v2_OpeningFcn gets called.  An
%      unrecognized property name or invalid value makes property
application
%      stop.  All inputs are passed to
UltrasonicHornGenerator_GUI_v2_OpeningFcn via varargin.
%
%      *See GUI Options on GUIDE's Tools menu.  Choose "GUI allows
only one
%      instance to run (singleton)".
%
% See also: GUIDE, GUIDATA, GUIHANDLES

% Edit the above text to modify the response to help
UltrasonicHornGenerator_GUI_v2

% Last Modified by GUIDE v2.5 01-May-2013 12:14:19

% Begin initialization code - DO NOT EDIT
gui_Singleton = 1;
gui_State = struct('gui_Name',       mfilename, ...
                   'gui_Singleton',  gui_Singleton, ...
                   'gui_OpeningFcn',
@UltrasonicHornGenerator_GUI_v2_OpeningFcn, ...
                   'gui_OutputFcn',
@UltrasonicHornGenerator_GUI_v2_OutputFcn, ...
                   'gui_LayoutFcn',  [] , ...
                   'gui_Callback',   []);
if nargin && ischar(varargin{1})
    gui_State.gui_Callback = str2func(varargin{1});
```

```matlab
end

if nargout
    [varargout{1:nargout}] = gui_mainfcn(gui_State, varargin{:});
else
    gui_mainfcn(gui_State, varargin{:});
end
% End initialization code - DO NOT EDIT


% --- Executes just before UltrasonicHornGenerator_GUI_v2 is made
visible.
function UltrasonicHornGenerator_GUI_v2_OpeningFcn(hObject,
eventdata, handles, varargin)
% This function has no output args, see OutputFcn.
% hObject     handle to figure
% eventdata   reserved - to be defined in a future version of MATLAB
% handles     structure with handles and user data (see GUIDATA)
% varargin    command line arguments to UltrasonicHornGenerator_GUI_v2
(see VARARGIN)

% Choose default command line output for
UltrasonicHornGenerator_GUI_v2
handles.output = hObject;

% Update handles structure
guidata(hObject, handles);

% UIWAIT makes UltrasonicHornGenerator_GUI_v2 wait for user response
(see UIRESUME)
% uiwait(handles.figure1);

plot_update(hObject, eventdata, handles)


% --- Outputs from this function are returned to the command line.
function varargout =
UltrasonicHornGenerator_GUI_v2_OutputFcn(hObject, eventdata, handles)
% varargout   cell array for returning output args (see VARARGOUT);
% hObject     handle to figure
% eventdata   reserved - to be defined in a future version of MATLAB
% handles     structure with handles and user data (see GUIDATA)

% Get default command line output from handles structure
varargout{1} = handles.output;


function edit_probe_len_Callback(hObject, eventdata, handles)
% hObject     handle to edit_probe_len (see GCBO)
% eventdata   reserved - to be defined in a future version of MATLAB
```

```matlab
% handles    structure with handles and user data (see GUIDATA)

% Hints: get(hObject,'String') returns contents of edit_probe_len as
text
%        str2double(get(hObject,'String')) returns contents of
edit_probe_len as a double
plot_update(hObject, eventdata, handles)


% --- Executes during object creation, after setting all properties.
function edit_probe_len_CreateFcn(hObject, eventdata, handles)
% hObject    handle to edit_probe_len (see GCBO)
% eventdata  reserved - to be defined in a future version of MATLAB
% handles    empty - handles not created until after all CreateFcns
called

% Hint: edit controls usually have a white background on Windows.
%        See ISPC and COMPUTER.
if ispc && isequal(get(hObject,'BackgroundColor'),
get(0,'defaultUicontrolBackgroundColor'))
    set(hObject,'BackgroundColor','white');
end




function edit_probe_AO_Callback(hObject, eventdata, handles)
% hObject    handle to edit_probe_AO (see GCBO)
% eventdata  reserved - to be defined in a future version of MATLAB
% handles    structure with handles and user data (see GUIDATA)

% Hints: get(hObject,'String') returns contents of edit_probe_AO as
text
%        str2double(get(hObject,'String')) returns contents of
edit_probe_AO as a double
plot_update(hObject, eventdata, handles)

% --- Executes during object creation, after setting all properties.
function edit_probe_AO_CreateFcn(hObject, eventdata, handles)
% hObject    handle to edit_probe_AO (see GCBO)
% eventdata  reserved - to be defined in a future version of MATLAB
% handles    empty - handles not created until after all CreateFcns
called

% Hint: edit controls usually have a white background on Windows.
%        See ISPC and COMPUTER.
if ispc && isequal(get(hObject,'BackgroundColor'),
get(0,'defaultUicontrolBackgroundColor'))
    set(hObject,'BackgroundColor','white');
end
```

```matlab
function edit_probe_A1_Callback(hObject, eventdata, handles)
% hObject    handle to edit_probe_A1 (see GCBO)
% eventdata  reserved - to be defined in a future version of MATLAB
% handles    structure with handles and user data (see GUIDATA)

% Hints: get(hObject,'String') returns contents of edit_probe_A1 as
text
%        str2double(get(hObject,'String')) returns contents of
edit_probe_A1 as a double
plot_update(hObject, eventdata, handles)


% --- Executes during object creation, after setting all properties.
function edit_probe_A1_CreateFcn(hObject, eventdata, handles)
% hObject    handle to edit_probe_A1 (see GCBO)
% eventdata  reserved - to be defined in a future version of MATLAB
% handles    empty - handles not created until after all CreateFcns
called

% Hint: edit controls usually have a white background on Windows.
%       See ISPC and COMPUTER.
if ispc && isequal(get(hObject,'BackgroundColor'),
get(0,'defaultUicontrolBackgroundColor'))
    set(hObject,'BackgroundColor','white');
end


% --- Executes on selection change in pop_layer.
function pop_layer_Callback(hObject, eventdata, handles)
% hObject    handle to pop_layer (see GCBO)
% eventdata  reserved - to be defined in a future version of MATLAB
% handles    structure with handles and user data (see GUIDATA)

% Hints: contents = cellstr(get(hObject,'String')) returns pop_layer
contents as cell array
%        contents{get(hObject,'Value')} returns selected item from
pop_layer


% --- Executes during object creation, after setting all properties.
function pop_layer_CreateFcn(hObject, eventdata, handles)
% hObject    handle to pop_layer (see GCBO)
% eventdata  reserved - to be defined in a future version of MATLAB
% handles    empty - handles not created until after all CreateFcns
called

% Hint: popupmenu controls usually have a white background on
Windows.
```

```matlab
%       See ISPC and COMPUTER.
if ispc && isequal(get(hObject,'BackgroundColor'),
get(O,'defaultUicontrolBackgroundColor'))
    set(hObject,'BackgroundColor','white');
end


function edit_fileName_Callback(hObject, eventdata, handles)
% hObject    handle to edit_fileName (see GCBO)
% eventdata  reserved - to be defined in a future version of MATLAB
% handles    structure with handles and user data (see GUIDATA)

% Hints: get(hObject,'String') returns contents of edit_fileName as
text
%        str2double(get(hObject,'String')) returns contents of
edit_fileName as a double


% --- Executes during object creation, after setting all properties.
function edit_fileName_CreateFcn(hObject, eventdata, handles)
% hObject    handle to edit_fileName (see GCBO)
% eventdata  reserved - to be defined in a future version of MATLAB
% handles    empty - handles not created until after all CreateFcns
called

% Hint: edit controls usually have a white background on Windows.
%       See ISPC and COMPUTER.
if ispc && isequal(get(hObject,'BackgroundColor'),
get(O,'defaultUicontrolBackgroundColor'))
    set(hObject,'BackgroundColor','white');
end


function edit_prong_len_Callback(hObject, eventdata, handles)
% hObject    handle to edit_prong_len (see GCBO)
% eventdata  reserved - to be defined in a future version of MATLAB
% handles    structure with handles and user data (see GUIDATA)

% Hints: get(hObject,'String') returns contents of edit_prong_len as
text
%        str2double(get(hObject,'String')) returns contents of
edit_prong_len as a double
plot_update(hObject, eventdata, handles)


% --- Executes during object creation, after setting all properties.
function edit_prong_len_CreateFcn(hObject, eventdata, handles)
% hObject    handle to edit_prong_len (see GCBO)
% eventdata  reserved - to be defined in a future version of MATLAB
```

```matlab
% handles    empty - handles not created until after all CreateFcns
called

% Hint: edit controls usually have a white background on Windows.
%       See ISPC and COMPUTER.
if ispc && isequal(get(hObject,'BackgroundColor'),
get(0,'defaultUicontrolBackgroundColor'))
    set(hObject,'BackgroundColor','white');
end


function edit_prong_width_Callback(hObject, eventdata, handles)
% hObject    handle to edit_prong_width (see GCBO)
% eventdata  reserved - to be defined in a future version of MATLAB
% handles    structure with handles and user data (see GUIDATA)

% Hints: get(hObject,'String') returns contents of edit_prong_width
as text
%        str2double(get(hObject,'String')) returns contents of
edit_prong_width as a double
plot_update(hObject, eventdata, handles)


% --- Executes during object creation, after setting all properties.
function edit_prong_width_CreateFcn(hObject, eventdata, handles)
% hObject    handle to edit_prong_width (see GCBO)
% eventdata  reserved - to be defined in a future version of MATLAB
% handles    empty - handles not created until after all CreateFcns
called

% Hint: edit controls usually have a white background on Windows.
%       See ISPC and COMPUTER.
if ispc && isequal(get(hObject,'BackgroundColor'),
get(0,'defaultUicontrolBackgroundColor'))
    set(hObject,'BackgroundColor','white');
end

function edit_prong_angle_Callback(hObject, eventdata, handles)
% hObject    handle to edit_prong_angle (see GCBO)
% eventdata  reserved - to be defined in a future version of MATLAB
% handles    structure with handles and user data (see GUIDATA)

% Hints: get(hObject,'String') returns contents of edit_prong_angle
as text
%        str2double(get(hObject,'String')) returns contents of
edit_prong_angle as a double
plot_update(hObject, eventdata, handles)


% --- Executes during object creation, after setting all properties.
```

```matlab
function edit_prong_angle_CreateFcn(hObject, eventdata, handles)
% hObject    handle to edit_prong_angle (see GCBO)
% eventdata  reserved - to be defined in a future version of MATLAB
% handles    empty - handles not created until after all CreateFcns
called

% Hint: edit controls usually have a white background on Windows.
%        See ISPC and COMPUTER.
if ispc && isequal(get(hObject,'BackgroundColor'),
get(0,'defaultUicontrolBackgroundColor'))
    set(hObject,'BackgroundColor','white');
end

% --- Executes on button press in pushbutton1.
function pushbutton1_Callback(hObject, eventdata, handles)
% hObject    handle to pushbutton1 (see GCBO)
% eventdata  reserved - to be defined in a future version of MATLAB
% handles    structure with handles and user data (see GUIDATA)
% update(hObject, eventdata, handles)


% get parameters from GUI
% Probe_LEN = str2num(get(handles.edit_probe_len, 'string'));
Probe_LEN = str2double(get(handles.edit_probe_len,'String'));
Probe_A0 = str2double(get(handles.edit_probe_A0, 'string'));
Probe_A1 = str2double(get(handles.edit_probe_A1, 'string'));
fileName = get(handles.edit_fileName, 'string');
% Obtain values from the popmemu
% pop_list = get(handles.pop_layer, 'string');
% pop_val = get(handles.pop_layer, 'value');
% layer_name = pop_list{pop_val};
layer_val = get(handles.pop_layer, 'value');
switch layer_val
    case 1
        layer_name = 'CMF';
    case 2
        layer_name = 'CMS';
end
% contents = cellstr(get(hObject,'String'))

print_layer_name = ['L ' layer_name '; \n'];

s=2000; %%(SCALING: 1 CIF Unit = 1/2000 Microns);

%% File start statement
%%%%%%%%%%%%%%%%%%%%%%%%%%%%%%%%%%%%%%%%
%Writing to file and displaying graphs
%%%%%%%%%%%%%%%%%%%%%%%%%%%%%%%%%%%%%%%%%
% file = fopen('tttt.cif','w');
file = fopen(fileName,'w');
fprintf(file,'DS 1 2 40; \n');
```

```matlab
fprintf(file,'UltrasonicHorn; \n'); % Input lines in CIF file
%%%%%%%%%%%%%%%%%%%%%%%%%%%%%%%%%%%%

%Define printing layers
% fprintf(file, 'L ', layer_name, '; \n');
fprintf(file, print_layer_name);

%% Horn Body drawing
%%%%%%%%%%%%%%%%%%%%%%%%%%%%%%%%%%%%%%
%Define catenonid horn shape
%%%%%%%%%%%%%%%%%%%%%%%%%%%%%%%%%%%%%%
%boxwidth: small horn (25) big horn (100)
%boxheight: samll horn (250) big horn (1000)
%%%%%%%%%%%%%%%%%%%%%%%%%%%%%%%%%%%%%%
% Probe_box_width=25;   %box width
% Probe_box_height=250; %box height

Probe_box_width=Probe_A1/10;   %box width
Probe_box_height=Probe_A0/10; %box height

%Note: for the back side, make the box hight slightly larger!!

% default value
% % % Probe_LEN=10000;  %Length of the probe
% % % Probe_A0=2500;    %End width of the probe
% % % Probe_A1=250;     %Tip width of the probe
Probe_offset=Probe_A1;
alpha=acosh(sqrt(Probe_A0/Probe_A1))/Probe_LEN;     %design parameter
for probe


%%%%%%%%%%%%%%%%%%%%%%%%%%%%%%%%%%%%%%%%
%Define catenonid horn equation
%%%%%%%%%%%%%%%%%%%%%%%%%%%%%%%%%%%%%%%%
x=0:Probe_box_width:Probe_LEN;
A=Probe_A1*cosh(alpha*(Probe_LEN-x)).^2+Probe_offset;
catenoid=A/2;

for qq=1:length(catenoid)
    %Drawing upper curve
    fprintf(file,
'B %10.0f %10.0f  %10.0f , %10.0f ;\n',Probe_box_width*s,
Probe_box_height*s, x(qq)*s, catenoid(qq)*s);
    %Drawing lower curve
    fprintf(file,
'B %10.0f %10.0f  %10.0f , %10.0f ;\n',Probe_box_width*s,
Probe_box_height*s, x(qq)*s, -catenoid(qq)*s);
end

%Drawing the bottom
```

```matlab
fprintf(file, 'B %10.0f %10.0f  %10.0f , %10.0f ;\n',
Probe_box_height*s, (Probe_A0+Probe_box_height*2)*s, -
(Probe_box_height/2)*s, 0);

%% Prong drawing
%%%%%%%%%%%%%%%%%%%%%%%%%%%%%%%%%%%%%
%Define prong
%%%%%%%%%%%%%%%%%%%%%%%%%%%%%%%%%%%%%
Prong_width=str2double(get(handles.edit_prong_width, 'string'));
Prong_length=str2double(get(handles.edit_prong_len, 'string'));
% Default values
% Prong_width=200;
% Prong_length=3000;
Prong_x=0;
Prong_y=0;
Prong_box=Probe_A1;
Prong_rad=Probe_offset-(Prong_width/2+Prong_box/2);
Prong_offsetX=Probe_LEN+Prong_rad;
Prong_offsetY=Probe_A1;

% fprintf(file, 'R %10.0f  %10.0f , %10.0f ;\n',Prong_rad*2*s,
Prong_offsetX*s, Prong_offsetY*s);
% prong length
% fprintf(file,
'B %10.0f %10.0f  %10.0f , %10.0f ;\n',Prong_length*s, Prong_box*s,
(((Prong_length)/2-Prong_rad)+Prong_offsetX)*s,(Probe_A1/2)*s);
% plot the prong length
fprintf(file, 'B %10.0f %10.0f  %10.0f , %10.0f ;\n',Prong_length*s,
Prong_box*s, (Probe_LEN+Prong_length/2)*s,
(Prong_width/2+Prong_box/2)*s);
fprintf(file, 'B %10.0f %10.0f  %10.0f , %10.0f ;\n',Prong_length*s,
Prong_box*s, (Probe_LEN+Prong_length/2)*s, -
(Prong_width/2+Prong_box/2)*s);
% fill the prong with the body box
fprintf(file, 'B %10.0f %10.0f  %10.0f , %10.0f ;\n',Prong_length*s,
Prong_box*s, (Probe_LEN+Prong_length/2)*s, Probe_offset*s);
fprintf(file, 'B %10.0f %10.0f  %10.0f , %10.0f ;\n',Prong_length*s,
Prong_box*s, (Probe_LEN+Prong_length/2)*s, -Probe_offset*s);
% fill the round with the body box
fprintf(file, 'R %10.0f  %10.0f , %10.0f ;\n',Prong_rad*2*s,
Probe_LEN*s, (Prong_rad+Prong_width/2)*s);
fprintf(file, 'R %10.0f  %10.0f , %10.0f ;\n',Prong_rad*2*s,
Probe_LEN*s, -(Prong_rad+Prong_width/2)*s);

%%%%%%%%%%%%%%%%%%%%%%%%%%%%%%%%%%%%%
%Tip blade definition
%Factors Influencing the Biocompatibility of Insertable
%Silicon Microshafts in Cerebral Cortex, 1992
%the tip angle should less than 20 degree
%%%%%%%%%%%%%%%%%%%%%%%%%%%%%%%%%%%%%
degree=20;  %unit in degree
```

```matlab
prong_trilength=Prong_width/2/sind(degree);
yextend=sind(20)*prong_trilength;
xextend=cosd(20)*prong_trilength;
% etchBond=250;


%%%%%%%%%%%%%%%%%%%%%%%%%%%%%%%%%%%%%%%%%%%%%%%%%%%%%%%%%%%%%%%%%%%%%%%%%%%
%%%%%%%%%%%%%%%%%%%%%%%%%%%%%%%%%%%%%%%%%%%%%%%%%%%%%%%%%%%%%%%%%%%%%%%%%%%
%%%%%%%%%%%%%%%%%%%%%%%
% need more work!!!! now only work for 20 degree sharpe tip
%define the tip slop
fprintf(file,'P');
fprintf(file,'%10.0f , %10.0f \n', (Probe_LEN+Prong_length)*s,
(Prong_width/2)*s);
fprintf(file,'%10.0f , %10.0f \n',
((Probe_LEN+Prong_length)+xextend)*s, (Prong_width/2)*s);
fprintf(file,'%10.0f , %10.0f \n',
((Probe_LEN+Prong_length)+xextend)*s, (Prong_width/2-yextend)*s);
fprintf(file,'; \n');

fprintf(file,'P');
fprintf(file,'%10.0f , %10.0f \n', (Probe_LEN+Prong_length)*s, -
(Prong_width/2)*s);
fprintf(file,'%10.0f , %10.0f \n',
((Probe_LEN+Prong_length)+xextend)*s, -(Prong_width/2)*s);
fprintf(file,'%10.0f , %10.0f \n',
((Probe_LEN+Prong_length)+xextend)*s, -(Prong_width/2-yextend)*s);
fprintf(file,'; \n');

%fill the tip with surroundings
fprintf(file, 'B %10.0f %10.0f  %10.0f , %10.0f ;\n',xextend*s,
Prong_box*s,(Probe_LEN+Prong_length+xextend/2)*s,
(Prong_width/2+Prong_box/2)*s);
fprintf(file, 'B %10.0f %10.0f  %10.0f , %10.0f ;\n',xextend*s,
Prong_box*s,(Probe_LEN+Prong_length+xextend/2)*s, Probe_offset*s);
fprintf(file, 'B %10.0f %10.0f  %10.0f , %10.0f ;\n',xextend*s,
Prong_box*s,(Probe_LEN+Prong_length+xextend/2)*s, -
(Prong_width/2+Prong_box/2)*s);
fprintf(file, 'B %10.0f %10.0f  %10.0f , %10.0f ;\n',xextend*s,
Prong_box*s,(Probe_LEN+Prong_length+xextend/2)*s, -Probe_offset*s);

%define the box in front of tip
fprintf(file,
'B %10.0f %10.0f  %10.0f , %10.0f ;\n',Probe_box_height*s,(Probe_offs
et/2+Probe_box_height)*s,(Probe_LEN+Prong_length+xextend+Probe_box_he
ight/2)*s, (Probe_offset/2+Probe_box_height)/2*s);
fprintf(file,
'B %10.0f %10.0f  %10.0f , %10.0f ;\n',Probe_box_height*s,(Probe_offs
et/2+Probe_box_height)*s,(Probe_LEN+Prong_length+xextend+Probe_box_he
ight/2)*s, -(Probe_offset/2+Probe_box_height)/2*s);
```

```matlab
%% File Clsing statements
fprintf(file,'DF; \n');
fprintf(file,'C 1;\n');
fprintf(file,'E \n');
fclose(file);


function plot_update(hObject, eventdata, handles)
% obtain the updated value from the edit box
Probe_LEN = str2double(get(handles.edit_probe_len,'String'));
Probe_A0 = str2double(get(handles.edit_probe_A0, 'string'));
Probe_A1 = str2double(get(handles.edit_probe_A1, 'string'));
Prong_width=str2double(get(handles.edit_prong_width, 'string'));
Prong_length=str2double(get(handles.edit_prong_len, 'string'));

% setupt the design values
Probe_box_width=25;    %box width
Probe_box_height=250; %box height
Probe_offset=Probe_A1/2-Probe_box_height/2;
alpha=acosh(sqrt(Probe_A0/Probe_A1))/Probe_LEN;       %design parameter
for probe
% Probe_box_width=25;    %box width
% Probe_box_height=250; %box height

%% Ploting the horn
plot_x=0:Probe_LEN;
plot_xaxes_min=-Probe_LEN*0.2;
plot_xaxes_max=(Probe_LEN+Prong_length)*1.2;
plot_yaxes_min=-Probe_A0*0.8;
plot_yaxes_max=Probe_A0*0.8;
% plot_A=Probe_A1*cosh(alpha*(Probe_LEN-plot_x)).^2+Probe_offset;
plot_A=(Probe_A1*cosh(alpha*(Probe_LEN-plot_x)).^2)/2;
plot_catenoid=plot_A;

% plot_botton_line=-Probe_A0/2-
Probe_box_height/2:Probe_A0/2+Probe_box_height/2;
plot_botton_line=-Probe_A0/2:Probe_A0/2;

%plotting function for visulization
axes(handles.axes1);
area(plot_x, plot_catenoid,'FaceColor', 'b'); hold on; %Upper side
area(plot_x, -plot_catenoid, 'FaceColor', 'b'); %Lower side
plot(0, plot_botton_line, 'b'); hold off;
xlabel('Ultrasonic Horn')
%define the max and min axis value for axes1
rectangle('Position',[(Probe_LEN),-
Prong_width/2,Prong_length,Prong_width], 'FaceColor', 'b')

axis([plot_xaxes_min plot_xaxes_max plot_yaxes_min
plot_yaxes_max]); %define the max and min axis value for axes1
% rectangle('Position',[x,y,w,h])
```

```matlab
% --- Executes on selection change in popupmenu2.
function popupmenu2_Callback(hObject, eventdata, handles)
% hObject    handle to popupmenu2 (see GCBO)
% eventdata  reserved - to be defined in a future version of MATLAB
% handles    structure with handles and user data (see GUIDATA)

% Hints: contents = cellstr(get(hObject,'String')) returns popupmenu2
contents as cell array
%        contents{get(hObject,'Value')} returns selected item from
popupmenu2


% --- Executes during object creation, after setting all properties.
function popupmenu2_CreateFcn(hObject, eventdata, handles)
% hObject    handle to popupmenu2 (see GCBO)
% eventdata  reserved - to be defined in a future version of MATLAB
% handles    empty - handles not created until after all CreateFcns
called

% Hint: popupmenu controls usually have a white background on
Windows.
%        See ISPC and COMPUTER.
if ispc && isequal(get(hObject,'BackgroundColor'),
get(0,'defaultUicontrolBackgroundColor'))
    set(hObject,'BackgroundColor','white');
end
```

6.2 *Process flow*

Detailed process flow description, equipment and parameters is shown in Table 6.1.

Table 6.1: Detailed process flow description

Step	Process description	Equipment	Parameters
1	Start		p or n type, 4 inch 500 micron thick Si wafers
2	Make the mask	DWL 2000 Hamatech	Developed the mask with the MIF 726 Chrome etch Hot strip bath 10 mins for both baths
3	MOS clean	MOS clean hood	Base Bath(10min), Acid Bath(10min), final resistivity of bath = 16Mohm-cm
4	Deposit LPCVD LS Silicon Nitride	E4, B4 furnace	Low stress recipe, 800C, 18A/min, single spaced loading, ~0.6 micron
5	Deposit LPCVD polysilicon	E3 furnace	furnace ~0.6 um thick
6	Ion Implant polysilicon	Innovion	boron 2e15/cm^2 at 100keV, 7 degree tilt
7	MOS clean	MOS clean hood	Base Bath(10min), Acid Bath(10min), final resistivity of bath = 16Mohm-cm
8	Anneal 950 C, 1 hour in N2 ambient	A1 furnace	General anneal furnace, measure sheet resistance ~ 180-190
9	Pattern PR	P-20 SPR220-3 MA6	P-20 (primer), 3000/1000/30 SPR220-3, 3000/1000/30, pre-bake 115C 90s MA6 expo: 5.5 sec, PEB 115C 90 sec MIF726 develop for 90 sec Hard bake in 90C oven for 30 mins (optional)
10	Etch polysilicon	Oxford 80 #1 or #2	1.Oxygen clean chamber 10 mins 2.CF4 seasoning for 10 mins 3.Oxygen clean (descum) for 1.5mins 4.CF4 for 12-13 mins 5.Rotate the wafer 6.CF4 for another 12-13 mins 7.Oxgen clean the chmaber for 5 mins
11	Remove PR	1165	put in 1165 (at least 1 hr) over night and sonication or Aura1000, 03F recipe
12	MOS clean	MOS clean hood	Base Bath(10min), Acid Bath(10min), final resistivity of bath = 16Mohm-cm
13	Grow thermal oxide	E2 furnace	300 nm in oxide furnace (recipe #8, T = 1000 P), set wet HCL oxide 50 min, cycle 5->1000 P) Measured ~340nm
14	Pattern PR	P-20 SPR220-3 MA6	P-20 (primer), 3000/1000/30 SPR220-3, 3000/1000/30, pre-bake 115C 90s MA6 expo: 5.5 sec, PEB 115C 90 sec MIF726 develop for 90 sec

			Hard bake in 90C oven for 30 mins (optional)
15	Etch Oxide	Oxford 80 #1 or #2	Oxygen clean for 1.5 minutes CHF3/O2 for 15min
17	Verify the oxide etching		probe station for measuring the poly resistors could also verified with the optical thickness measurmenet
18	Strip PR and Cleaning wafer surface	1165	over night + Sonication Spray Acetone and IPA and spin rinse the wafer Spinner and wash the wafer Put in 90C oven to dehydrate for at least 10 mins
19	Sputter Al	CVC Sputter Al+1% Si	Al + 1% silicon, Sputter time 30.5 mins ~600 nm
20	Pattern PR	P-20 SPR220-3 MA6	P-20 (primer), 3000/1000/30 SPR220-3, 3000/1000/30, pre-bake 115C 90s MA6 expo: 5.5 sec, PEB 115C 90 sec MIF726 develop for 90 sec Hard bake in 90C oven for 30 mins (optional)
21	Etch aluminum	PT740	1.5min break through and 25 mins etch
22	Strip PR and Cleaning wafer surface	1165	over night + Sonication Spray Acetone and IPA and spin rinse the wafer Spinner and wash the wafer Put in 90C oven to dehydrate for at least 10 mins
23	Anneal aluminum	C1, C2 furnace	5% H2/N2 Anneal 250C, Ramp for 30, Anneal for 60 mins Note: it will take very long time to cool down ~0.86C/min, Generally proecss will take around 4~5 hours
24	Measure aluminum sheet resistance w/ probe station	CDE resistance map	90~100 mOhm/square
25	Passivation nitride deposition	GSI	1. Auto clean/Etch for 10-20 mins 2. LS Nitride pre-deposition for 3 mins 3. Desposite the device for 5-6 mins (~600nm) LS Nitride - 600nm @ 250C ; the deposition time should be equal to clean time
26	Cleaning wafer surface	Spinner	Spray Acetone and IPA and spin rinse the wafer Spinner and wash the wafer

			Put in 90C oven to dehydrate for at least 10 mins
27	Pattern PR	LOR-3a SPR220-3 MA6	LOR-3a, 2500/500/60, back 180C 5 mins SPR220-3, 3000/1000/30, pre-bake 115C 3 mins MA6 expo: 5.5 sec, wait for 10 mins to rehydration PEB 115C 3 mins MIF726 develop for 90-120 sec (manually) Hard bake in 90C oven for 30 mins (optional)
28	Descum	Oxford 80 #1 or #2	2 minutes, Oxygen Clean
29	Measure resist thickness	P10	Thickness ~ 2.6 um
30	Metal Evaporation	CHA 50 (NBTC)	Cr - 250A; Pt - 2300A 1.5A/s 1A/s
31	Lift-off	Photolith bench	Leave wafers face down in 1165 solutions overnight or at least 6 hours Sonicate the wafer in 1165 individually before clean the wafer to make sure the lift-off is good
32	Cleaning wafer surface	Spinner	Spray Acetone and IPA and spin rinse the wafer Spinner and wash the wafer Put in 90C oven to dehydrate for at least 10 mins
33	Passivation nitride deposition	GSI	1. Auto clean/Etch for 10-20 mins 2. LS Nitride pre-deposition for 3 mins 3. Desposite the device for 6 mins (~600nm) LS Nitride - 600nm @ 250C ; the deposition time should be equal to clean time
34	Cleaning wafer surface	Spinner	Spray Acetone and IPA and spin rinse the wafer Spinner and wash the wafer Put in 90C oven to dehydrate for at least 10 mins
35	Pattern PR	P-20 SPR220-3 MA6	P-20 (primer), 3000/1000/30 SPR220-3, 3000/1000/30, pre-bake 115C 90s MA6 expo: 5.5 sec, PEB 115C 90 sec MIF726 develop for 90 sec Hard bake in 90C oven for 30 mins (optional)
36	PECVD Nitride etch	Oxford 80 #1 or #2	CHF3/O2 Nitride etch recipe; thickness to be etched ~1800 nm 10 mins oxygen clean

			10 mins seasoning (use monitor wafer to test) 2 mins descum 30 min CHF3/O2 5 mins oxygen clean
37	Strip PR and Cleaning wafer surface	1165	over night + Sonication Spray Acetone and IPA and spin rinse the wafer Spinner and wash the wafer Put in 90C oven to dehydrate for at least 10 mins
38	Pattern PR	HDMS oven SPR220-7 MA6	HDMS oven, take about 30 mins SPR220-7, 2000/1000/45 proxy-bake 115C 60 sec; pre-bake 115C 120s MA6 expo: 22 sec, wait for at least 45 mins to rehydration PEB 115C 90 sec MIF726 develop for 2.5 mins (manually) Hard bake in 90C oven for at least 6 hours
39	Manual Edgebead removal	Spinner hood	Use cotton swabs drenched in acetone to manually remove 5mm ring of PR on the circumference of the wafer
40	Frontside Etch - PECVD and LPCVD Nitride etch	Oxford 80 #1 or #2	CHF3/O2 Nitride etch recipe; thickness to be etched - 600nm LS-LPCVD Nitride + 2000nm LS-PECVD Nitride (35 mins)
41	Frontside Etch - DRIE Silicon etch	Unaxis UN770	0TRENCH recipe; thickness to be etched - 200 microns or 1THRUJPC recipe -run 150 loops (thickness around 135~140 um)
42	Strip PR and Cleaning wafer surface	1165	over night + Sonication Spray Acetone and IPA and spin rinse the wafer Spinner and wash the wafer Put in 90C oven to dehydrate for at least 10 mins
43	Frontside - Spin SR25 (proTek)	Spinner	2000 rpm, 1000 rpm/sec, 60 sec
44	Soft bake/solvent removal	Hot Plate	4 minutes, 115~130C (at least) 4 minutes, 160~180C (at least) 4 minutes, 205C (at least)
45	Exposure	HDMS oven SPR220-7 MA6	HDMS oven, take about 30 mins SPR220-7, 2000/1000/45 proxy-bake 115C 60 sec; pre-bake 115C 120s MA6 expo: 9s, 3 cycle, 10s wait time, (PEB

			115C 90 sec) Rehydration for at least 1 hour MIF726 develop for 2.5 - 3 mins Hard bake in 90C oven for at least 6 hours
46	Manual Edgebead removal	Spinner hood	Use cotton swabs drenched in acetone to manually remove 5mm ring of PR on the circumference of the wafer
47	Backside Etch - LPCVD Nitride etch	Oxford 80 #1 or #2	CHF3/O2 Nitride etch recipe; thickness to be etched - 600nm ~10 mins oxygen clean ~2 mins descum ~10 mins CHF3/O2 Oxide etch ~11 mins SF6/O2 Si etching ~5 mins Oxygen clean
48	Backside Etch - DRIE Silicon etch	Unaxis UN770	0TRENCH recipe; thickness to be etched - 360 microns or 1THRUJPC recipe (~580 loops total)
49	Strip ProTek SR-25 and Cleaning wafer suface	1165	overnight + sonication Spray Acetone and IPA and spin rinse the wafer, Spinner and wash the wafer Put in 90C oven to dehydrate for at least 10 mins
50	Cleaning device	Oxford 80 #1 or #2	Oxgen clean for 5 mins (optional)

6.3 *Wheatstone bridge calculator*

Matlab GUI code for calculating each piezoresistor values from six measurements. The GUI is shown in Figure 6.2.
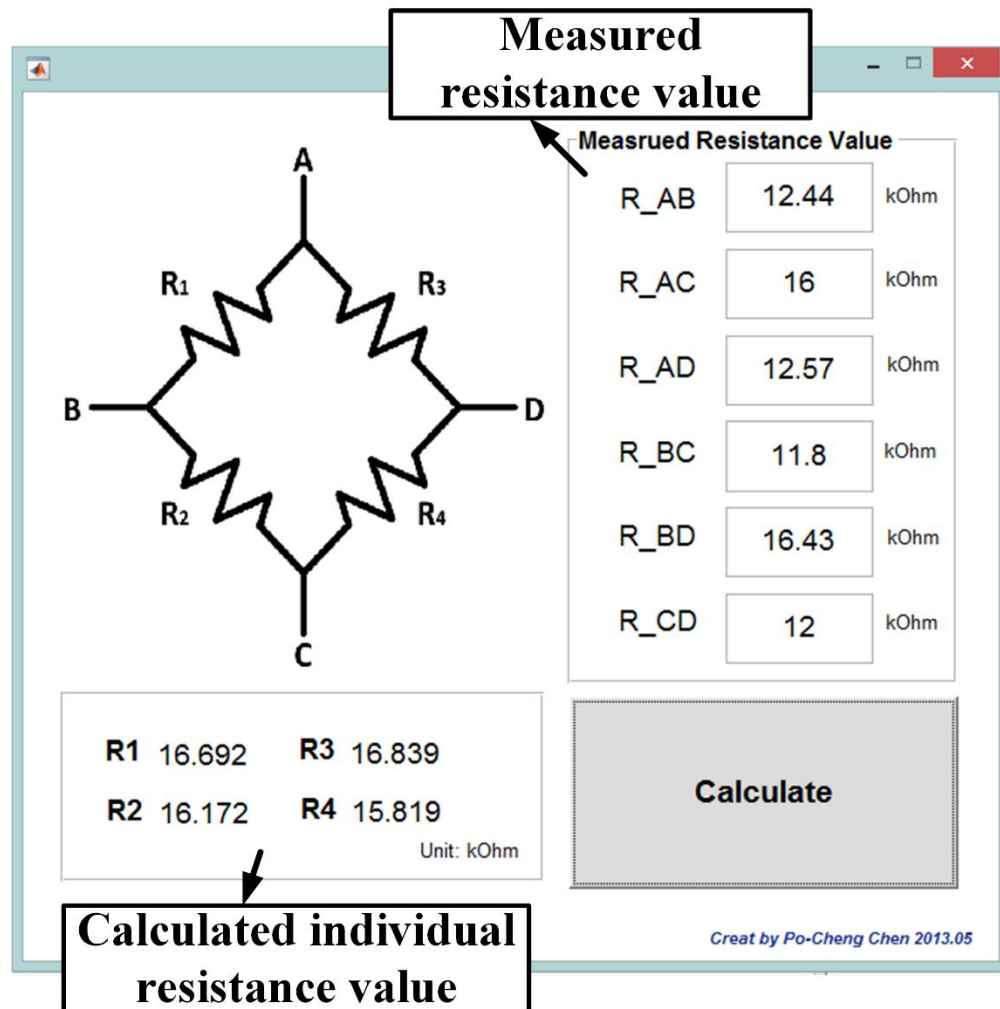
Figure 6.2: GUI for the Wheatstone bridge calculator.

```matlab
function varargout = wheatStoneBridge_cal(varargin)
% WHEATSTONEBRIDGE_CAL MATLAB code for wheatStoneBridge_cal.fig
%      WHEATSTONEBRIDGE_CAL, by itself, creates a new
WHEATSTONEBRIDGE_CAL or raises the existing
%      singleton*.
%
%      H = WHEATSTONEBRIDGE_CAL returns the handle to a new
WHEATSTONEBRIDGE_CAL or the handle to
%      the existing singleton*.
%
%      WHEATSTONEBRIDGE_CAL('CALLBACK',hObject,eventData,handles,...)
calls the local
%      function named CALLBACK in WHEATSTONEBRIDGE_CAL.M with the
given input arguments.
%
%      WHEATSTONEBRIDGE_CAL('Property','Value',...) creates a new
WHEATSTONEBRIDGE_CAL or raises the
%      existing singleton*.  Starting from the left, property value
pairs are
%      applied to the GUI before wheatStoneBridge_cal_OpeningFcn gets
called.  An
%      unrecognized property name or invalid value makes property
application
%      stop.  All inputs are passed to
wheatStoneBridge_cal_OpeningFcn via varargin.
%
%      *See GUI Options on GUIDE's Tools menu.  Choose "GUI allows
only one
%      instance to run (singleton)".
%
% See also: GUIDE, GUIDATA, GUIHANDLES

% Edit the above text to modify the response to help
wheatStoneBridge_cal

% Last Modified by GUIDE v2.5 02-May-2013 17:40:23

% Begin initialization code - DO NOT EDIT
gui_Singleton = 1;
gui_State = struct('gui_Name',       mfilename, ...
                   'gui_Singleton',  gui_Singleton, ...
                   'gui_OpeningFcn',
@wheatStoneBridge_cal_OpeningFcn, ...
                   'gui_OutputFcn',
@wheatStoneBridge_cal_OutputFcn, ...
                   'gui_LayoutFcn',  [] , ...
                   'gui_Callback',   []);
if nargin && ischar(varargin{1})
    gui_State.gui_Callback = str2func(varargin{1});
end
```

```matlab
if nargout
    [varargout{1:nargout}] = gui_mainfcn(gui_State, varargin{:});
else
    gui_mainfcn(gui_State, varargin{:});
end
% End initialization code - DO NOT EDIT


% --- Executes just before wheatStoneBridge_cal is made visible.
function wheatStoneBridge_cal_OpeningFcn(hObject, eventdata, handles, varargin)
% This function has no output args, see OutputFcn.
% hObject    handle to figure
% eventdata  reserved - to be defined in a future version of MATLAB
% handles    structure with handles and user data (see GUIDATA)
% varargin   command line arguments to wheatStoneBridge_cal (see VARARGIN)

% Choose default command line output for wheatStoneBridge_cal
handles.output = hObject;

% Update handles structure
guidata(hObject, handles);

% load the picture
axes(handles.axes1)
image(imread('wheatStoneBridge.png'));
axis off




% UIWAIT makes wheatStoneBridge_cal wait for user response (see UIRESUME)
% uiwait(handles.figure1);


% --- Outputs from this function are returned to the command line.
function varargout = wheatStoneBridge_cal_OutputFcn(hObject, eventdata, handles)
% varargout  cell array for returning output args (see VARARGOUT);
% hObject    handle to figure
% eventdata  reserved - to be defined in a future version of MATLAB
% handles    structure with handles and user data (see GUIDATA)

% Get default command line output from handles structure
varargout{1} = handles.output;
```

```matlab
function edit_RAB_Callback(hObject, eventdata, handles)
% hObject    handle to edit_RAB (see GCBO)
% eventdata  reserved - to be defined in a future version of MATLAB
% handles    structure with handles and user data (see GUIDATA)

% Hints: get(hObject,'String') returns contents of edit_RAB as text
%        str2double(get(hObject,'String')) returns contents of
edit_RAB as a double


% --- Executes during object creation, after setting all properties.
function edit_RAB_CreateFcn(hObject, eventdata, handles)
% hObject    handle to edit_RAB (see GCBO)
% eventdata  reserved - to be defined in a future version of MATLAB
% handles    empty - handles not created until after all CreateFcns
called

% Hint: edit controls usually have a white background on Windows.
%       See ISPC and COMPUTER.
if ispc && isequal(get(hObject,'BackgroundColor'),
get(O,'defaultUicontrolBackgroundColor'))
    set(hObject,'BackgroundColor','white');
end




function edit_RAC_Callback(hObject, eventdata, handles)
% hObject    handle to edit_RAC (see GCBO)
% eventdata  reserved - to be defined in a future version of MATLAB
% handles    structure with handles and user data (see GUIDATA)

% Hints: get(hObject,'String') returns contents of edit_RAC as text
%        str2double(get(hObject,'String')) returns contents of
edit_RAC as a double


% --- Executes during object creation, after setting all properties.
function edit_RAC_CreateFcn(hObject, eventdata, handles)
% hObject    handle to edit_RAC (see GCBO)
% eventdata  reserved - to be defined in a future version of MATLAB
% handles    empty - handles not created until after all CreateFcns
called

% Hint: edit controls usually have a white background on Windows.
%       See ISPC and COMPUTER.
if ispc && isequal(get(hObject,'BackgroundColor'),
get(O,'defaultUicontrolBackgroundColor'))
    set(hObject,'BackgroundColor','white');
end
```

```matlab
function edit_RAD_Callback(hObject, eventdata, handles)
% hObject    handle to edit_RAD (see GCBO)
% eventdata  reserved - to be defined in a future version of MATLAB
% handles    structure with handles and user data (see GUIDATA)

% Hints: get(hObject,'String') returns contents of edit_RAD as text
%        str2double(get(hObject,'String')) returns contents of
edit_RAD as a double


% --- Executes during object creation, after setting all properties.
function edit_RAD_CreateFcn(hObject, eventdata, handles)
% hObject    handle to edit_RAD (see GCBO)
% eventdata  reserved - to be defined in a future version of MATLAB
% handles    empty - handles not created until after all CreateFcns
called

% Hint: edit controls usually have a white background on Windows.
%       See ISPC and COMPUTER.
if ispc && isequal(get(hObject,'BackgroundColor'),
get(O,'defaultUicontrolBackgroundColor'))
    set(hObject,'BackgroundColor','white');
end




function edit_RBC_Callback(hObject, eventdata, handles)
% hObject    handle to edit_RBC (see GCBO)
% eventdata  reserved - to be defined in a future version of MATLAB
% handles    structure with handles and user data (see GUIDATA)

% Hints: get(hObject,'String') returns contents of edit_RBC as text
%        str2double(get(hObject,'String')) returns contents of
edit_RBC as a double


% --- Executes during object creation, after setting all properties.
function edit_RBC_CreateFcn(hObject, eventdata, handles)
% hObject    handle to edit_RBC (see GCBO)
% eventdata  reserved - to be defined in a future version of MATLAB
% handles    empty - handles not created until after all CreateFcns
called

% Hint: edit controls usually have a white background on Windows.
%       See ISPC and COMPUTER.
```

```matlab
if ispc && isequal(get(hObject,'BackgroundColor'),
get(0,'defaultUicontrolBackgroundColor'))
    set(hObject,'BackgroundColor','white');
end




function edit_RBD_Callback(hObject, eventdata, handles)
% hObject    handle to edit_RBD (see GCBO)
% eventdata  reserved - to be defined in a future version of MATLAB
% handles    structure with handles and user data (see GUIDATA)

% Hints: get(hObject,'String') returns contents of edit_RBD as text
%        str2double(get(hObject,'String')) returns contents of
edit_RBD as a double



% --- Executes during object creation, after setting all properties.
function edit_RBD_CreateFcn(hObject, eventdata, handles)
% hObject    handle to edit_RBD (see GCBO)
% eventdata  reserved - to be defined in a future version of MATLAB
% handles    empty - handles not created until after all CreateFcns
called

% Hint: edit controls usually have a white background on Windows.
%       See ISPC and COMPUTER.
if ispc && isequal(get(hObject,'BackgroundColor'),
get(0,'defaultUicontrolBackgroundColor'))
    set(hObject,'BackgroundColor','white');
end




function edit_RCD_Callback(hObject, eventdata, handles)
% hObject    handle to edit_RCD (see GCBO)
% eventdata  reserved - to be defined in a future version of MATLAB
% handles    structure with handles and user data (see GUIDATA)

% Hints: get(hObject,'String') returns contents of edit_RCD as text
%        str2double(get(hObject,'String')) returns contents of
edit_RCD as a double



% --- Executes during object creation, after setting all properties.
function edit_RCD_CreateFcn(hObject, eventdata, handles)
% hObject    handle to edit_RCD (see GCBO)
% eventdata  reserved - to be defined in a future version of MATLAB
% handles    empty - handles not created until after all CreateFcns
called
```

```matlab
% Hint: edit controls usually have a white background on Windows.
%       See ISPC and COMPUTER.
if ispc && isequal(get(hObject,'BackgroundColor'),
get(0,'defaultUicontrolBackgroundColor'))
    set(hObject,'BackgroundColor','white');
end


% --- Executes on button press in pushbutton_calculate.
function pushbutton_calculate_Callback(hObject, eventdata, handles)
% hObject    handle to pushbutton_calculate (see GCBO)
% eventdata  reserved - to be defined in a future version of MATLAB
% handles    structure with handles and user data (see GUIDATA)

% Obtain value from the edit box
R_AB = str2double(get(handles.edit_RAB,'String'));
R_AC = str2double(get(handles.edit_RAC,'String'));
R_AD = str2double(get(handles.edit_RAD,'String'));
R_BC = str2double(get(handles.edit_RBC,'String'));
R_BD = str2double(get(handles.edit_RBD,'String'));
R_CD = str2double(get(handles.edit_RCD,'String'));

% equation for each indivudual resistor values
C2=(R_AB+R_BC-R_AC)/2;
C3=(R_AB+R_AD-R_BD)/2;
C4=(R_AC-R_BC+R_BD-R_AD)/2;

R1=(C4*C4-(R_CD*R_AB))/(C4-R_CD);
R2=(R1*C2)/(R1-R_AB);
R3=(R1*C3)/(R1-R_AB);
R4=(R1*C4)/(R1-R_AB);
% display the calcuated results
set(handles.text_R1, 'String', num2str(R1));
set(handles.text_R2, 'String', num2str(R2));
set(handles.text_R3, 'String', num2str(R3));
set(handles.text_R4, 'String', num2str(R4));
```

6.4 *Wireless neural amplifier circuit dimensions*

The block diagram of the wireless neural amplifier is shown in Figure 6.3. The neural amplifier acquires the biopotential signal from neuron cells and transmit the recorded data with a radio frequency (RF) data transmitter wirelessly. The architecture of neural amplifier is shown in Figure 6.4, the transconductance (Gm) stage is shown in Figure 6.5. A Colpitts oscillator (Figure 6.6) is used for transmitting data modulated in analog frequency modulation scheme. The dimensions of each elements are listed in Table 6.2.
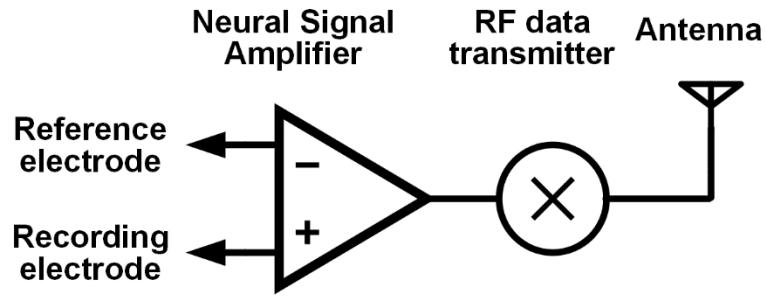
Figure 6.3: Block diagram of wireless neural amplifier.
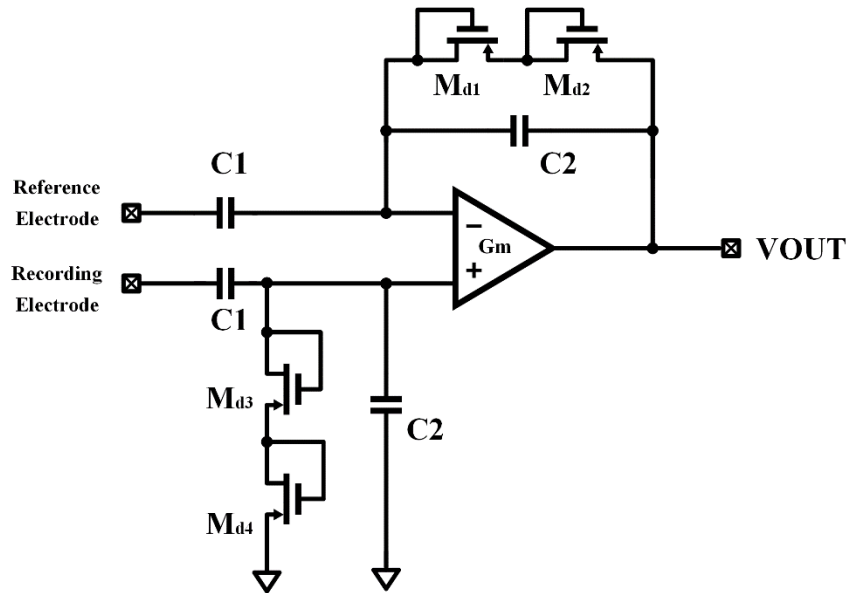
Figure 6.4: Neural amplifier circuit structure.
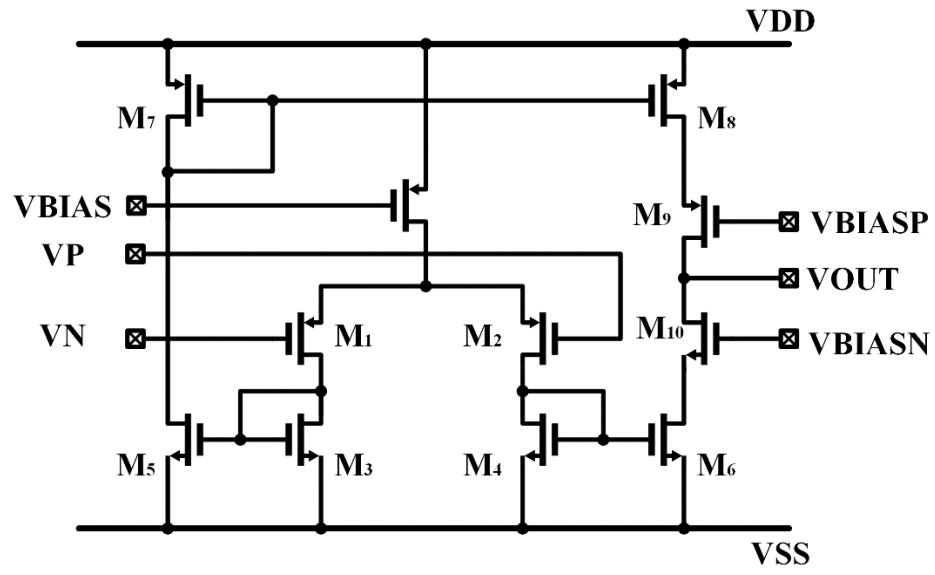
Figure 6.5: Transconductnace (Gm) stage circuit.
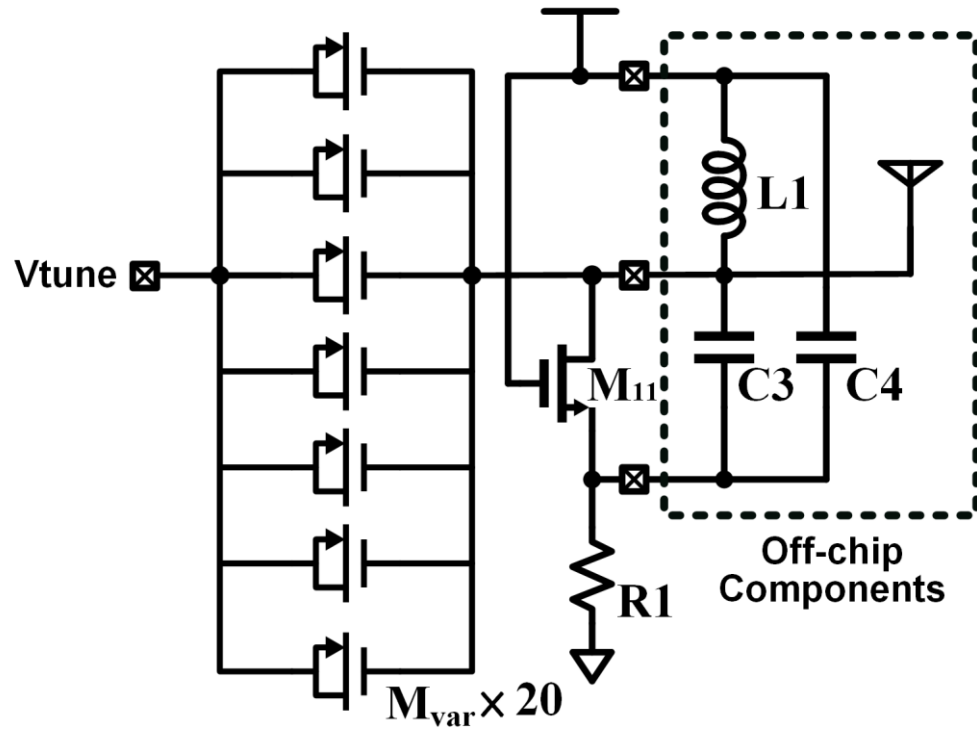
Figure 6.6: Colpitts oscillator circuit is used as data transmitter. The data is transmitted with analog frequency modulation.

Table 6.2: Dimension of elements in the neural amplifier

Device	W/L
M_1, M_2	800/1
M_3, M_4, M_5, M_6	60/50
M_7, M_8	10/30
M_9	12/3
M_{10}	6/3
M_{11}	40/3
M_{d1}, M_{d2}, M_{d3}, M_{d4}	2/2
M_{var}	8/0.35
C1	20 pF
C2	200 fF
C3	22 pF
C4	13 pF
L1	150 nH
R1	10 kΩ

BIBLIOGRAPHY

[1] E. M. Maynard, C. T. Nordhausen, and R. A. Normann, "The Utah Intracortical Electrode Array: A recording structure for potential brain-computer interfaces," *Electroencephalogr. Clin. Neurophysiol.*, vol. 102, no. 3, pp. 228–239, Mar. 1997.

[2] K. D. Wise, J. B. Angell, and A. Starr, "An Integrated-Circuit Approach to Extracellular Microelectrodes," *IEEE Trans. Biomed. Eng.*, vol. BME-17, no. 3, pp. 238–247, Jul. 1970.

[3] M. A. L. Nicolelis, "Brain–machine interfaces to restore motor function and probe neural circuits," *Nat. Rev. Neurosci.*, vol. 4, no. 5, pp. 417–422, May 2003.

[4] D. A. Borton, M. Yin, J. Aceros, and A. Nurmikko, "An implantable wireless neural interface for recording cortical circuit dynamics in moving primates," *J. Neural Eng.*, vol. 10, no. 2, p. 026010, 2013.

[5] L. R. Hochberg, M. D. Serruya, G. M. Friehs, J. A. Mukand, M. Saleh, A. H. Caplan, A. Branner, D. Chen, R. D. Penn, and J. P. Donoghue, "Neuronal ensemble control of prosthetic devices by a human with tetraplegia," *Nature*, vol. 442, no. 7099, pp. 164–171, Jul. 2006.

[6] S.-P. Kim, J. D. Simeral, L. R. Hochberg, J. P. Donoghue, and M. J. Black, "Neural control of computer cursor velocity by decoding motor cortical spiking activity in humans with tetraplegia," *J. Neural Eng.*, vol. 5, no. 4, p. 455, 2008.

[7] M. F. Bear, B. W. Connors, and M. A. Paradiso, *Neuroscience*. Lippincott Williams & Wilkins, 2007.

[8] P. J. Rousche, D. S. Pellinen, J. Pivin D. P., J. C. Williams, R. J. Vetter, and D. R. Kipke, "Flexible polyimide-based intracortical electrode arrays with bioactive capability," *IEEE Trans. Biomed. Eng.*, vol. 48, no. 3, pp. 361–371, Mar. 2001.

[9] D.-H. Kim, J. Viventi, J. J. Amsden, J. Xiao, L. Vigeland, Y.-S. Kim, J. A. Blanco, B. Panilaitis, E. S. Frechette, D. Contreras, D. L. Kaplan, F. G. Omenetto, Y. Huang, K.-C. Hwang, M. R. Zakin, B. Litt, and J. A. Rogers, "Dissolvable films of silk fibroin for ultrathin conformal bio-integrated electronics," *Nat. Mater.*, vol. 9, no. 6, pp. 511–517, Jun. 2010.

[10] Q. Bai and K. D. Wise, "Single-unit neural recording with active microelectrode arrays," *IEEE Trans. Biomed. Eng.*, vol. 48, no. 8, pp. 911–920, Aug. 2001.

[11] P.-C. Chen, C. G. Clark, C. Schaffer, R. F. Gilmour, and A. Lal, "Ultrasonically enabled neural probes with co-located electrical and mechanical transduction," in *Ultrasonics Symposium (IUS), 2012 IEEE International*, 2012, pp. 350–353.

[12] H. J. Lee, Y. Son, J. Kim, C. J. Lee, E.-S. Yoon, and I.-J. Cho, "A multichannel neural probe with embedded microfluidic channels for simultaneous in vivo neural recording and drug delivery," *Lab. Chip*, vol. 15, no. 6, pp. 1590–1597, Mar. 2015.

[13]   D. B. Jaroch, M. P. Ward, E. Y. Chow, J. L. Rickus, and P. P. Irazoqui, "Magnetic insertion system for flexible electrode implantation," *J. Neurosci. Methods*, vol. 183, no. 2, pp. 213–222, Oct. 2009.

[14]   L. A. Geddes, "Historical evolution of circuit models for the electrode-electrolyte interface," *Ann. Biomed. Eng.*, vol. 25, no. 1, pp. 1–14, Feb. 1997.

[15]   E. T. McAdams and J. Jossinet, "Physical interpretation of Schwan's limit voltage of linearity," *Med. Biol. Eng. Comput.*, vol. 32, no. 2, pp. 126–130, Mar. 1994.

[16]   D. C. Grahame, "Theory of the Faradaic Admittance. II. Analysis of the Current-Interrupter Method," *J. Phys. Chem.*, vol. 57, no. 3, pp. 257–261, Mar. 1953.

[17]   G. Kovacs, "Introduction to the theory, design and modeling of thin-film microelectrodes for neural interfaces," in *Enabling Technologies for Cultured Neural Networks*, D. Stenger and T. McKenna, Eds. London: Academic Press, 1994, pp. 121–165.

[18]   A. J. Bard and L. R. Faulkner, *Electrochemical Methods: Fundamentals and Applications, 2nd Edition*. Wiley Global Education, 2000.

[19]   E. T. McAdams, A. Lackermeier, J. A. McLaughlin, D. Macken, and J. Jossinet, "The linear and non-linear electrical properties of the electrode-electrolyte interface," *Biosens. Bioelectron.*, vol. 10, no. 1–2, pp. 67–74, 1995.

[20]   K. F. Graff, *Wave Motion in Elastic Solids*. Dover Publications, 1975.

[21]   X. Chen, *Micromachined ultrasonic actuators for biomedical applications: surgical tools, cardiac microprobes, and microfluidic actuation*. Cornell University, May, 2006.

[22]   E. Eisner, "Design of Sonic Amplitude Transformers for High Magnification," *J. Acoust. Soc. Am.*, vol. 35, no. 9, pp. 1367–1377, Sep. 1963.

[23]   E. Eisner, "Complete Solutions of the 'Webster' Horn Equation," *J. Acoust. Soc. Am.*, vol. 41, no. 4B, pp. 1126–1146, Apr. 1967.

[24]   A. Lal, *Micromachined Silicon Ultrasonic Longitudinal Mode Actuators: Theory and Applications to Surgery, Pumping and Atomization*. University of California, Berkeley, 1996.

[25]   G. Amza and D. Drimer, "The design and construction of solid concentrators for ultrasonic energy," *Ultrasonics*, vol. 14, no. 5, pp. 223–226, Sep. 1976.

[26]   F. V. Hunt, "Stress and Strain Limits on the Attainable Velocity in Mechanical Vibration," *J. Acoust. Soc. Am.*, vol. 32, no. 9, pp. 1123–1128, Sep. 1960.

[27]   A. Ramkumar, A. Lal, D. . Paduch, and P. N. Schlegel, "An Ultrasonically Actuated Silicon-Microprobe-Based Testicular Tubule Assay," *IEEE Trans. Biomed. Eng.*, vol. 56, no. 11, pp. 2666–2674, Nov. 2009.

[28]   A. Ramkumar and A. Lal, "Silicon ultrasonic horn actuated microprobes based self-calibrating viscosity sensor," in *2010 IEEE 23rd International Conference on Micro Electro Mechanical Systems (MEMS)*, 2010, pp. 991–994.

[29]   C. J. Shen, A. Ramkumar, A. Lal, and R. F. G. Jr, "Wireless cardiac action potential transmission with ultrasonically inserted silicon microprobes," *J. Micromechanics Microengineering*, vol. 21, no. 5, p. 054011, 2011.

[30]   M. A. Lebedev, J. M. Carmena, J. E. O'Doherty, M. Zacksenhouse, C. S. Henriquez, J. C. Principe, and M. A. L. Nicolelis, "Cortical Ensemble Adaptation to Represent Velocity of an Artificial Actuator Controlled by a Brain-Machine Interface," *J. Neurosci.*, vol. 25, no. 19, pp. 4681–4693, May 2005.

[31]   V. S. Polikov, P. A. Tresco, and W. M. Reichert, "Response of brain tissue to chronically implanted neural electrodes," *J. Neurosci. Methods*, vol. 148, no. 1, pp. 1–18, Oct. 2005.

[32]   K. Bazaka and M. V. Jacob, "Implantable Devices: Issues and Challenges," *Electronics*, vol. 2, no. 1, pp. 1–34, Dec. 2012.

[33]   A. Prasad, Q.-S. Xue, V. Sankar, T. Nishida, G. Shaw, W. J. Streit, and J. C. Sanchez, "Comprehensive characterization and failure modes of tungsten microwire arrays in chronic neural implants," *J. Neural Eng.*, vol. 9, no. 5, p. 056015, Oct. 2012.

[34]   D. H. Szarowski, M. D. Andersen, S. Retterer, A. J. Spence, M. Isaacson, H. G. Craighead, J. N. Turner, and W. Shain, "Brain responses to micro-machined silicon devices," *Brain Res.*, vol. 983, no. 1–2, pp. 23–35, Sep. 2003.

[35]   A. Prasad, V. Sankar, A. T. Dyer, E. Knott, Q.-S. Xue, T. Nishida, J. R. Reynolds, G. Shaw, W. Streit, and J. C. Sanchez, "Coupling biotic and abiotic metrics to create a testbed for predicting neural electrode performance," in *2011 Annual International Conference of the IEEE Engineering in Medicine and Biology Society, EMBC*, 2011, pp. 3020–3023.

[36]   sociallymindful, "Recording the brain is not reading the mind," *Socially Mindful*, 29-Oct-2013. .

[37]   "Reading the Surface of the Brain," *MIT Technology Review*. [Online]. Available: https://www.technologyreview.com/s/413686/reading-the-surface-of-the-brain/. [Accessed: 01-Apr-2016].

[38]   K. Najafi and J. F. Hetke, "Strength characterization of silicon microprobes in neurophysiological tissues," *IEEE Trans. Biomed. Eng.*, vol. 37, no. 5, pp. 474–481, May 1990.

[39]   W. Jensen, K. Yoshida, and U. G. Hofmann, "In-vivo implant mechanics of flexible, silicon-based ACREO microelectrode arrays in rat cerebral cortex," *IEEE Trans. Biomed. Eng.*, vol. 53, no. 5, pp. 934–940, May 2006.

[40]   C. S. Bjornsson, S. J. Oh, Y. A. Al-Kofahi, Y. J. Lim, K. L. Smith, J. N. Turner, S. De, B. Roysam, W. Shain, and S. J. Kim, "Effects of insertion conditions on

tissue strain and vascular damage during neuroprosthetic device insertion," *J. Neural Eng.*, vol. 3, no. 3, p. 196, Sep. 2006.

[41]   D. J. Edell, V. V. Toi, V. M. McNeil, and L. D. Clark, "Factors influencing the biocompatibility of insertable silicon microshafts in cerebral cortex," *IEEE Trans. Biomed. Eng.*, vol. 39, no. 6, pp. 635–643, Jun. 1992.

[42]   A. A. Sharp, A. M. Ortega, D. Restrepo, D. Curran-Everett, and K. Gall, "In Vivo Penetration Mechanics and Mechanical Properties of Mouse Brain Tissue at Micrometer Scales," *IEEE Trans. Biomed. Eng.*, vol. 56, no. 1, pp. 45–53, Jan. 2009.

[43]   P. J. Gilgunn, R. Khilwani, T. D. Y. Kozai, D. J. Weber, X. T. Cui, G. Erdos, O. B. Ozdoganlar, and G. K. Fedder, "An ultra-compliant, scalable neural probe with molded biodissolvable delivery vehicle," in *2012 IEEE 25th International Conference on Micro Electro Mechanical Systems (MEMS)*, 2012, pp. 56–59.

[44]   K. A. Ludwig, N. B. Langhals, M. D. Joseph, S. M. Richardson-Burns, J. L. Hendricks, and D. R. Kipke, "Poly(3,4-ethylenedioxythiophene) (PEDOT) polymer coatings facilitate smaller neural recording electrodes," *J. Neural Eng.*, vol. 8, no. 1, p. 014001, 2011.

[45]   X. T. Cui and D. D. Zhou, "Poly (3,4-Ethylenedioxythiophene) for Chronic Neural Stimulation," *IEEE Trans. Neural Syst. Rehabil. Eng.*, vol. 15, no. 4, pp. 502–508, Dec. 2007.

[46]   K. A. Ludwig, J. D. Uram, J. Yang, D. C. Martin, and D. R. Kipke, "Chronic neural recordings using silicon microelectrode arrays electrochemically deposited with a poly(3,4-ethylenedioxythiophene) (PEDOT) film," *J. Neural Eng.*, vol. 3, no. 1, p. 59, 2006.

[47]   M. A. L. Nicolelis, D. Dimitrov, J. M. Carmena, R. Crist, G. Lehew, J. D. Kralik, and S. P. Wise, "Chronic, multisite, multielectrode recordings in macaque monkeys," *Proc. Natl. Acad. Sci.*, vol. 100, no. 19, pp. 11041–11046, Sep. 2003.

[48]   E. M. Maynard, E. Fernandez, and R. A. Normann, "A technique to prevent dural adhesions to chronically implanted microelectrode arrays," *J. Neurosci. Methods*, vol. 97, no. 2, pp. 93–101, Apr. 2000.

[49]   S. Schmidt, K. Horch, and R. Normann, "Biocompatibility of silicon-based electrode arrays implanted in feline cortical tissue," *J. Biomed. Mater. Res.*, vol. 27, no. 11, pp. 1393–1399, Nov. 1993.

[50]   P. K. Campbell, K. E. Jones, R. J. Huber, K. W. Horch, and R. A. Normann, "A silicon-based, three-dimensional neural interface: manufacturing processes for an intracortical electrode array," *IEEE Trans. Biomed. Eng.*, vol. 38, no. 8, pp. 758–768, Aug. 1991.

[51]   J. N. Turner, W. Shain, D. H. Szarowski, M. Andersen, S. Martins, M. Isaacson, and H. Craighead, "Cerebral Astrocyte Response to Micromachined Silicon Implants," *Exp. Neurol.*, vol. 156, no. 1, pp. 33–49, Mar. 1999.

[52]   "dDrive Single Use Microdrive - NeuroNexus." [Online]. Available: http://neuronexus.com/products/microdrives/ddrive. [Accessed: 12-Apr-2016].

[53]   M. HajjHassan, V. Chodavarapu, and S. Musallam, "NeuroMEMS: Neural Probe Microtechnologies," *Sensors*, vol. 8, no. 10, pp. 6704–6726, Oct. 2008.

[54]   R. A. Normann, E. M. Maynard, P. J. Rousche, and D. J. Warren, "A neural interface for a cortical vision prosthesis," *Vision Res.*, vol. 39, no. 15, pp. 2577–2587, Jul. 1999.

[55]   Y. Schneider, S. Zahn, and H. Rohm, "Ultrasonic Cutting of Foods," in *Ultrasound Technologies for Food and Bioprocessing*, H. Feng, G. Barbosa-Canovas, and J. Weiss, Eds. Springer New York, 2011, pp. 211–237.

[56]   W. Littmann, H. Storck, and J. Wallaschek, "Sliding friction in the presence of ultrasonic oscillations: superposition of longitudinal oscillations," *Arch. Appl. Mech.*, vol. 71, no. 8, pp. 549–554, Aug. 2001.

[57]   M. K. Nabibekov, B. D. Plyushchenkov, and I. Y. Sarkisov, "Study of ultrasonic cutting of soft biotissues," *Mech. Compos. Mater.*, vol. 16, no. 3, pp. 377–382, May 1980.

[58]   C.-P. Shen, "Silicon Based Co-Integrated Bioelectrical And Biomechanical Interfaces: Applications To Insect Olfactory Neural Interfaces, Miniature Neural Interfaces, And Cardiac Excitation Characterization," Jan. 2012.

[59]   C. Koch, H. Nürnberger, and H. P. Reimann, "Measurement of temperature elevation in tissue for the optimum and safe use of scalpel-type ultrasonic surgery devices," *J. Phys. Conf. Ser.*, vol. 1, no. 1, p. 122, 2004.

[60]   T. Kinoshita, E. Kanehira, K. Omura, K. Kawakami, and Y. Watanabe, "Experimental study on heat production by a 23.5-kHz ultrasonically activated device for endoscopic surgery," *Surg. Endosc.*, vol. 13, no. 6, pp. 621–625, May 2014.

[61]   C. Koch, T. Friedrich, F. Metternich, A. Tannapfel, H.-P. Reimann, and U. Eichfeld, "Determination of temperature elevation in tissue during the application of the harmonic scalpel," *Ultrasound Med. Biol.*, vol. 29, no. 2, pp. 301–309, Feb. 2003.

[62]   M. M. Elwassif, Q. Kong, M. Vazquez, and M. Bikson, "Bio-Heat Transfer Model of Deep Brain Stimulation Induced Temperature changes," in *28th Annual International Conference of the IEEE Engineering in Medicine and Biology Society, 2006. EMBS '06*, 2006, pp. 3580–3583.

[63]   W. M. M. P. E. M. I. of Technology and W. R. M. P. E. U. of Toledo, *The Bonded Electrical Resistance Strain Gage : An Introduction: An Introduction*. Oxford University Press, USA, 1992.

[64]   R. L. Hannah and S. E. Reed, *Strain Gage Users' Handbook*. Springer Science & Business Media, 1992.

[65]   G. T. A. Kovacs, *Micromachined Transducers Sourcebook*. WCB/McGraw-Hill, 1998.

[66]   S. D. Senturia, *Microsystem Design*. Springer US, 2005.

[67]   H. Schäfer, V. Graeger, and R. Kobs, "Temperature-independent pressure sensors using polycrystalline silicon strain gauges," *Sens. Actuators*, vol. 17, no. 3–4, pp. 521–527, May 1989.

[68]   Y. Kim and S. Kwon, "Resistivity dependence of gauge factor of polysilicon strain gauge," *IET Micro Nano Lett.*, vol. 5, no. 3, pp. 189–192, Jun. 2010.

[69]   C. Yeh and K. Najafi, "A low-voltage tunneling-based silicon microaccelerometer," *IEEE Trans. Electron Devices*, vol. 44, no. 11, pp. 1875–1882, Nov. 1997.

[70]   S. Bhardwaj, "S/N Optimization and Noise Considerations for Piezoresistive Microphones," 2001. .

[71]   P. M. Klinge, M. A. Vafa, T. Brinker, A. Brandis, G. F. Walter, T. Stieglitz, M. Samii, and K. Wewetzer, "Immunohistochemical characterization of axonal sprouting and reactive tissue changes after long-term implantation of a polyimide sieve electrode to the transected adult rat sciatic nerve," *Biomaterials*, vol. 22, no. 17, pp. 2333–2343, Sep. 2001.

[72]   R. Abhishek, "Micromachined Ultrasonic Silicon Horn Actuators For Biomedical Applications: Surgical Tools, Cardiac Electrophysiological Recordings, Testicular Tubule-Size Detection And Fluid Viscosity Measurement," Aug. 2010.

[73]   C. J. Shen, A. Ramkumar, A. Lal, and R. F. Gilmour, "Wireless transmission of cardiac action potentials with ultrasonically guided insertion of silicon probes," 2010, pp. 5022–5025.

[74]   S. J. Eliades and X. Wang, "Chronic multi-electrode neural recording in free-roaming monkeys," *J. Neurosci. Methods*, vol. 172, no. 2, pp. 201–214, Jul. 2008.

[75]   D. Lewitus, K. L. Smith, W. Shain, and J. Kohn, "Ultrafast resorbing polymers for use as carriers for cortical neural probes," *Acta Biomater.*, vol. 7, no. 6, pp. 2483–2491, Jun. 2011.

[76]   J. T. W. Kuo, B. J. Kim, S. A. Hara, C. D. Lee, C. A. Gutierrez, T. Q. Hoang, and E. Meng, "Novel flexible Parylene neural probe with 3D sheath structure for enhancing tissue integration," *Lab. Chip*, vol. 13, no. 4, pp. 554–561, Jan. 2013.

[77]   S. Takeuchi, Y. Yoshida, D. Ziegler, K. Mabuchi, and T. Suzuki, "Parylene flexible neural probe with micro fluidic channel," in *Micro Electro Mechanical Systems, 2004. 17th IEEE International Conference on. (MEMS)*, 2004, pp. 208–211.

[78]   T. D. Y. Kozai and D. R. Kipke, "Insertion shuttle with carboxyl terminated self-assembled monolayer coatings for implanting flexible polymer neural probes in the brain," *J. Neurosci. Methods*, vol. 184, no. 2, pp. 199–205, Nov. 2009.

[79]   S. H. Felix, K. G. Shah, V. M. Tolosa, H. J. Sheth, A. C. Tooker, T. L. Delima, S. P. Jadhav, L. M. Frank, and S. S. Pannu, "Insertion of flexible neural probes using rigid stiffeners attached with biodissolvable adhesive," *J. Vis. Exp. JoVE*, no. 79, p. e50609, 2013.

[80]   D. R. Kipke, D. S. Pellinen, and R. J. Vetter, "Advanced neural implants using thin-film polymers," in *IEEE International Symposium on Circuits and Systems, 2002. ISCAS 2002*, 2002, vol. 4, pp. IV–173–IV–176 vol.4.

[81]   R. B. Greenwald, Y. H. Choe, J. McGuire, and C. D. Conover, "Effective drug delivery by PEGylated drug conjugates," *Adv. Drug Deliv. Rev.*, vol. 55, no. 2, pp. 217–250, Feb. 2003.

[82]   R. J. Halter, A. Schned, J. Heaney, A. Hartov, and K. D. Paulsen, "Electrical Properties of Prostatic Tissues: I. Single Frequency Admittivity Properties," *J. Urol.*, vol. 182, no. 4, pp. 1600–1607, Oct. 2009.

[83]   R. J. Halter, A. Schned, J. Heaney, A. Hartov, and K. D. Paulsen, "Electrical Properties of Prostatic Tissues: II. Spectral Admittivity Properties," *J. Urol.*, vol. 182, no. 4, pp. 1608–1613, Oct. 2009.

[84]   S. Laufer, A. Ivorra, V. E. Reuter, B. Rubinsky, and S. B. Solomon, "Electrical impedance characterization of normal and cancerous human hepatic tissue," *Physiol. Meas.*, vol. 31, no. 7, pp. 995–1009, Jul. 2010.

[85]   B. R. Lee, W. W. Roberts, D. G. Smith, H. W. Ko, J. I. Epstein, K. Lecksell, A. W. Partin, and P. C. Walsh, "Bioimpedance: Novel Use of a Minimally Invasive Technique for Cancer Localization in the Intact Prostate," *J. Urol.*, vol. 162, no. 4, pp. 1546–1547, Oct. 1999.

[86]   R. E. Shadwick, "Elastic energy storage in tendons: mechanical differences related to function and age," *J. Appl. Physiol.*, vol. 68, no. 3, pp. 1033–1040, Mar. 1990.

[87]   C. T. McKee, J. A. Last, P. Russell, and C. J. Murphy, "Indentation Versus Tensile Measurements of Young's Modulus for Soft Biological Tissues," *Tissue Eng. Part B Rev.*, vol. 17, no. 3, pp. 155–164, Jun. 2011.

[88]   K. Hoyt, B. Castaneda, M. Zhang, P. Nigwekar, P. A. di Sant'Agnese, J. V. Joseph, J. Strang, D. J. Rubens, and K. J. Parker, "Tissue elasticity properties as biomarkers for prostate cancer," *Cancer Biomark. Sect. Dis. Markers*, vol. 4, no. 4–5, pp. 213–225, 2008.

[89]   M. Zhang, P. Nigwekar, B. Castaneda, K. Hoyt, J. V. Joseph, A. di Sant'Agnese, E. M. Messing, J. G. Strang, D. J. Rubens, and K. J. Parker, "Quantitative Characterization of Viscoelastic Properties of Human Prostate Correlated with Histology," *Ultrasound Med. Biol.*, vol. 34, no. 7, pp. 1033–1042, Jul. 2008.

[90]   V. Jalkanen, "Hand-held resonance sensor for tissue stiffness measurements—a theoretical and experimental analysis," *Meas. Sci. Technol.*, vol. 21, no. 5, p. 055801, 2010.

[91]   K. Yan, L. Li, J. Joseph, D. R. Rubens, E. M. Messing, L. Liao, and Y. Yu, "A real-time prostate cancer detection technique using needle insertion force and patient-specific criteria during percutaneous intervention," *Med. Phys.*, vol. 36, no. 7, pp. 3356–3362, Jul. 2009.

[92]   A. Vignali, V. W. Fazio, I. C. Lavery, J. W. Milsom, J. M. Church, T. L. Hull, S. A. Strong, and J. R. Oakley, "Factors associated with the occurrence of leaks in stapled rectal anastomoses: a review of 1,014 patients," *J. Am. Coll. Surg.*, vol. 185, no. 2, pp. 105–113, Aug. 1997.

[93]   Telem DA, Chin EH, Nguyen SQ, and Divino CM, "Risk factors for anastomotic leak following colorectal surgery: A case-control study," *Arch. Surg.*, vol. 145, no. 4, pp. 371–376, Apr. 2010.

[94]   F. L. Hammond, M. J. Smith, and R. J. Wood, "Printing Strain Gauges on Surgical Instruments for Force Measurement," *J. Med. Devices*, vol. 8, no. 3, pp. 030935–030935, Jul. 2014.

[95]   S. M. Hu, "Critical stress in silicon brittle fracture, and effect of ion implantation and other surface treatments," *J. Appl. Phys.*, vol. 53, no. 5, pp. 3576–3580, May 1982.

[96]   W. D. Sylwestrowicz and M. S. E. Koonce, "Fracture mechanism of single crystals of silicon," *Philos. Mag.*, vol. 8, no. 92, pp. 1427–1428, Aug. 1963.

[97]   H. Liebowitz, *Fracture of Nonmetals and Composites*. Elsevier, 2013.

[98]   R. J. Halter, A. Hartov, J. A. Heaney, K. D. Paulsen, and A. R. Schned, "Electrical Impedance Spectroscopy of the Human Prostate," *IEEE Trans. Biomed. Eng.*, vol. 54, no. 7, pp. 1321–1327, Jul. 2007.

[99]   E. Gersing, "Impedance spectroscopy on living tissue for determination of the state of organs," *Bioelectrochem. Bioenerg.*, vol. 45, no. 2, pp. 145–149, May 1998.

[100] K. S. Osterman, P. J. Hoopes, C. DeLorenzo, D. J. Gladstone, and K. D. Paulsen, "Non-invasive assessment of radiation injury with electrical impedance spectroscopy," *Phys. Med. Biol.*, vol. 49, no. 5, p. 665, 2004.

[101] A. Soley, M. Lecina, X. Gámez, J. J. Cairó, P. Riu, X. Rosell, R. Bragós, and F. Gòdia, "On-line monitoring of yeast cell growth by impedance spectroscopy," *J. Biotechnol.*, vol. 118, no. 4, pp. 398–405, Sep. 2005.

[102] J. Glahder, B. Norrild, M. B. Persson, and B. R. R. Persson, "Transfection of HeLa-cells with pEGFP plasmid by impedance power-assisted electroporation," *Biotechnol. Bioeng.*, vol. 92, no. 3, pp. 267–276, Nov. 2005.

[103] J. Niu and J. y. Lee, "A New Approach for the Determination of Fish Freshness by Electrochemical Impedance Spectroscopy," *J. Food Sci.*, vol. 65, no. 5, pp. 780–785, Aug. 2000.

[104] L. N. Cotton and D. L. Marshall, "Rapid Impediometric Method to Determine Crustacean Food Freshness," in *New Techniques in the Analysis of Foods*, M. H. Tunick, S. A. Palumbo, and P. M. Fratamico, Eds. Springer US, 1998, pp. 147–160.

[105] D. L. M. PhD and P. L. W.-L. PhD, "Comparison of Impedance, Microbial, Sensory, and pH Methods to Determine Shrimp Quality," *J. Aquat. Food Prod. Technol.*, vol. 6, no. 2, pp. 17–31, Mar. 1997.

[106] T. Glozman and H. Azhari, "A Method for Characterization of Tissue Elastic Properties Combining Ultrasonic Computed Tomography With Elastography," *J. Ultrasound Med.*, vol. 29, no. 3, pp. 387–398, Mar. 2010.

[107] H. Helle, H. Välimäki, and J. Lekkala, "Comparing a 10 MHz thickness–shear mode quartz resonator with a commercial process viscometer in monitoring resol manufacture process," *Sens. Actuators B Chem.*, vol. 81, no. 2–3, pp. 133–140, Jan. 2002.

[108] A. Saluja and D. S. Kalonia, "Measurement of fluid viscosity at microliter volumes using quartz impedance analysis," *AAPS PharmSciTech*, vol. 5, no. 3, pp. 68–81, Sep. 2004.

[109] B. A. Martin, S. W. Wenzel, and R. M. White, "Viscosity and density sensing with ultrasonic plate waves," *Sens. Actuators Phys.*, vol. 22, no. 1–3, pp. 704–708, Jun. 1990.

[110] B. Jakoby, M. Scherer, M. Buskies, and H. Eisenschmid, "An automotive engine oil viscosity sensor," *IEEE Sens. J.*, vol. 3, no. 5, pp. 562–568, Oct. 2003.

[111] B. Jakoby and M. J. Vellekoop, "Physical sensors for water-in-oil emulsions," *Sens. Actuators Phys.*, vol. 110, no. 1–3, pp. 28–32, Feb. 2004.

[112] A. Agoston, F. Keplinger, and B. Jakoby, "Evaluation of a vibrating micromachined cantilever sensor for measuring the viscosity of complex organic liquids," *Sens. Actuators Phys.*, vol. 123–124, pp. 82–86, Sep. 2005.

[113] W. Li, D. Rodger, P. Menon, and Y.-C. Tai, "Corrosion Behavior of Parylene-Metal-Parylene Thin Films in Saline," *ECS Trans.*, vol. 11, no. 18, pp. 1–6, Oct. 2008.

[114] S. Boskovic, J. W. M. Chon, P. Mulvaney, and J. E. Sader, "Rheological measurements using microcantilevers," *J. Rheol.*, vol. 46, no. 4, p. 891, 2002.

[115] I. Etchart, H. Chen, P. Dryden, J. Jundt, C. Harrison, K. Hsu, F. Marty, and B. Mercier, "MEMS sensors for density–viscosity sensing in a low-flow microfluidic environment," *Sens. Actuators Phys.*, vol. 141, no. 2, pp. 266–275, Feb. 2008.

[116] N. Thanh-Vinh, K. Matsumoto, and I. Shimoyama, "A viscometer based on vibration of droplets on a piezoresistive cantilever array," 2015, pp. 176–179.

[117] Wei-Chih Wang, M. Afromowitz, and B. Hannaford, "Technique for mechanical measurements using optical scattering from a micropipette [cells application]," *IEEE Trans. Biomed. Eng.*, vol. 41, no. 3, pp. 298–304, Mar. 1994.

[118] A. Ramkumar, X. Chen, and A. Lal, "P1I-7 Silicon Ultrasonic Horn Driven Microprobe Viscometer," in *IEEE Ultrasonics Symposium, 2006*, 2006, pp. 1449–1452.

[119] F. P. Incropera, *Fundamentals of heat and mass transfer*. John Wiley, 2007.